Estimation of Standard Model backgrounds to the search for electroweak production of Supersymmetry in events with at least two tau leptons in the final state

Dissertation der Fakultät für Physik

der

Ludwig-Maximilians-Universität München

vorgelegt von

Sebastian Becker

geboren in Mainz

München, den 20.09.2013

Erstgutachterin: Prof. Dr. Dorothee Schaile

Zweitgutachter: Prof. Dr. Wolfgang Dünnweber

Datum der mündlichen Prüfung: 04.11.2013

Abstract

This thesis presents a search for Supersymmetry in events with at least two hadronically decaying tau leptons and missing transverse energy. The analysis is focused on the electro-weak production of gaugino pairs. Electroweak production processes for SUSY particles are promising candidates for the discovery of Supersymmetry with R-parity conservation at hadron-hadron colliders. For the analysis a sample of proton-proton collisions at a center of mass energy of $\sqrt{s} = 8\,\text{TeV}$ with an integrated luminosity of $\int \mathcal{L}\ \text{dt} = 20.3\,\text{fb}^{-1}$ is used. The collisions have been recorded with the ATLAS detector at the LHC in the year 2012. In two different selections the Standard Model predictions are compared with the observations. The observation of 6 events in the first selection and 14 in the second does not deviate significantly from the Standard Model with an expectation of 11 events in the first selection and 17 in the second. These results are interpreted in a phenomenological Minimal Supersymmetric Standard Model and in simplified models. For a simplified model with a chargino-neutralino pair production scenario the parameter space for masses of the lightest neutralino up to 100 GeV and up to 350 GeV for the lightest chargino mass can be excluded. For a simplified model with chargino pair production processes the parameter space for the lightest neutralino mass up to $30-50\,\text{GeV}$ in a range for the lightest chargino mass of $170-330\,\text{GeV}$ can be excluded. This thesis is focused on the estimation techniques of Standard Model background processes. Different methods for the estimation of the background originating from Z-boson and top-quark decays are investigated.

Zusammenfassung

In dieser Arbeit wird eine Suche nach Supersymmetrie für Ereignisse mit zwei hadronisch zerfallenden Tau Leptonen und fehlender Transversalenergie im Endzustand präsentiert. Die Analyse konzentriert sich dabei auf die elektroschwache Produktion von Gaugino Paaren. Elektroschwache Produktionsprozesse sind vielversprechende Kandidaten für die Entdeckung der Supersymmetrie mit R-Paritätserhaltung an Hadron-Hadron Teilchenbeschleunigern. Für die Analyse wurde ein Datensatz von Proton-Proton Kollisionen bei einer Schwerpunktenergie von $\sqrt{s} = 8\,\text{TeV}$ mit einer integrierten Luminosität von $\int \mathcal{L}\ \text{dt} = 20.3\,\text{fb}^{-1}$ verwendet. Die Daten wurden mit dem ATLAS Detektor am LHC im Jahr 2012 aufgezeichnet. Die beobachteten Datenereignisse wurden mit den Vorhersagen des Standardmodells für zwei unterschiedliche Sätze von Signalauswahlkriterien verglichen. Die Beobachtung von 6 Ereignissen in der ersten Signalregion und 14 Ereignissen in der zweiten weicht nicht signifikant von den Vorhersagen des Standardmodells mit 11 Ereignissen in der ersten Signalregion und 17 in der zweiten ab. Diese Ergebnisse wurden mit Hinblick auf ein phänomenologisches minimal supersymmetrisches Standardmodell und auf vereinfachte supersymmetrische Modelle interpretiert. Für ein vereinfachtes Modell mit Chargino-Neutralino Paarproduktion kann der Parameterraum für Massen des leichtesten Neutralinos bis zu 100 GeV und bis zu 350 GeV für die Masse des leichtesten Charginos ausgeschlossen werden. Für ein vereinfachtes Modell mit Chargino Paarproduktion kann der Parameterraum für die leichteste Neutralinomasse bis zu $30 - 50\,\text{GeV}$ in einem Bereich der leichtesten Chargino Masse von $170 - 330\,\text{GeV}$ ausgeschlossen werden. Das Hauptaugenmerk dieser Arbeit liegt jedoch auf den Verfahren, die zur Bestimmung des Standardmodell-Untergrundes benutzt werden. Unterschiedliche Methoden zur Bestimmung des Untergrunds aus Z-Boson und Top-Quark Zerfallsprozessen wurden untersucht.

Contents

1 Introduction

Particle physics is dedicated to the investigation of the behavior of the smallest constituents of matter, the elementary particles. The goal is the description of the observations of particles and their interactions with a physical model. With the technological improvement of experiments and the scientific progress in the understanding of the theory, various models to describe the observations have been developed over the time. However, with every progress in the precision of measurements new undescribed phenomena were seen and thus new questions arose. The Standard Model is the theory that is used at the present time to describe elementary particle physics.
With the Large Hadron Collider (LHC) investigations of collisions at high energy scales are possible. With experiments like the multi-purpose detector ATLAS physicists are investigating the Higgs-Boson, which is the last Standard Model particle, that had been undetected in the pre-LHC era. Also models for physics beyond the Standard Model are tested.
The Standard Model is not able to describe all particles and all their interactions together. The description of gravity is not included in the Standard Model. Another important discovery in the observation of galaxy rotations and the expansion of the universe is that only 5% of the universe consists of visible matter. The conclusion is that dark matter, which is not described by the Standard Model, has to exist. The dark matter particles interact with other particles via the gravitational force and the weak interaction but do not interact electromagnetically or via the strong interaction. One promising model that could explain dark matter is Supersymmetry. With a supersymmetric expansion of the Standard Model additional particles are predicted, however not yet observed. The lightest supersymmetric particle might be a candidate for dark matter. Also other open questions of the Standard Model could be solved with Supersymmetry such as the hierarchy problem or the unification of the running coupling constants at high energies.
In this thesis a search for Supersymmetry in events with at least two hadronically decaying tau leptons and missing transverse energy is presented. The selection criteria described in this thesis are focused on the detection of events in which a pair of SUSY particles was electroweakly produced. With the selection used most of the Standard Model processes with a similar event topology, which represent the background to this analysis, can be rejected. The analysis is very sensitive to the discovery of electroweak SUSY production. To perform a precise measurement the Standard Model background needs to be predicted with high accuracy. This thesis presents investigations of the methods to predict the irreducible background to the selection originating from Z-boson or top-quark decays.
This thesis is divided into eight chapters. A brief overview of the theoretical background

is given in chapter 2. The Standard Model is described and its limitations discussed. The theory of Supersymmetry is introduced as a possible solution for some of the problems of the Standard Model. It is also described how new supersymmetric particles could be produced from Standard Model particles and how such supersymmetric particles would decay afterwards. In chapter 3 the experimental setup of the LHC accelerator and the ATLAS detector is described. Chapter 4 contains a summary of all important ingredients for the analysis, such as the datasets, the description of the kinematic variables, or the definition of particle reconstruction methods. The exact selection criteria for the analysis are also presented in this chapter. In chapter 5 the background estimation methods are introduced and the expected event yields of the various processes are given. In chapter 6 improvements for the estimation of the Z + jets and top background are discussed. In chapter 7 a validation of the background estimation described in the previous chapter is presented. In chapter 8 the final results of the analysis are presented and the results are interpreted with respect to several different supersymmetric models.

2 Theory

2.1 The Standard Model

The goal of elementary particle physics is to describe the constituents and interactions of matter within a quantum field theory. The Standard Model is a self-consistent and renormalizable gauge theory, which comprises all known particles and elementary interactions except for gravity [1, 2, 3, 4, 5].
Particles are influenced by four fundamental interactions: Gravity couples to the mass of particles, the electromagnetic force couples to the electric charge of particles, the strong interaction couples to the so called "color charge", and the weak interaction couples to the so called "weak charge". Besides the mass of a particle and charges relevant to the corresponding interaction the spin is an important quantity of particles. All particles obey the spin-statistics-theorem (Pauli 1940) and can be divided into two groups. The first group are the fermions with half-integer spin. The symmetry of their wave function is described by the Fermi-Dirac statistics. One consequence is the Pauli principle, which prohibits two identical fermions being in the same quantum state. Fermions are the fundamental constituents of all matter. Particles with integer spin are called bosons, because they are following the Bose-Einstein statistics. Unlike fermions bosons can exist with the exact same quantum state at the same place and time. The fundamental interactions are mediated by vector bosons.

	1st gen.		2nd gen.		3rd gen.		
	Flavor	Mass [MeV]	Flavor	Mass [MeV]	Flavor	Mass [GeV]	El. charge
Leptons	e	0.511	μ	105.7	tau	1.776	-1
	ν_e	$< 2 \cdot 10^{-6}$	ν_μ	< 0.19	ν_τ	$< 18.2 \cdot 10^{-3}$	0
Quarks	u	$2.3^{+0.7}_{-0.5}$	c	1275 ± 25	t	$173.5 \pm 0.6 \pm 0.8$	$+\frac{2}{3}$
	d	$4.8^{+0.7}_{-0.3}$	s	95 ± 5	b	4.18 ± 0.03	$-\frac{1}{3}$

Table 2.1: Properties of the fundamental fermions of the Standard Model. Values are taken from [6].

The fundamental fermions are divided into leptons and quarks. The leptons do not carry a color charge and are therefore only subject to weak, electromagnetic, and gravitational interactions. Only the quarks carry a color charge, which is needed to be influenced by the strong force. There exist 6 different leptons and quarks, and each quark can exist in three different color states. They are subdivided into three families or generations of isospin doublets, where the corresponding particles of each generation have the same

charge but increasing mass over the generations. The charged leptons are the electron (e), muon (μ), and tau (τ) with a corresponding neutral neutrino (ν) for each. The positively charged quarks are the up (u), charm (c), and top (t) quark, and the negatively charged quarks are called down (d), strange (s), and bottom (b) (see table 2.1). Although the neutrino mass has not been measured yet and only upper limits can be given it cannot be neglected. Missing energy in the distribution of the β-decay and the observation of neutrino oscillations lead to the assumption of a nonzero mass [7]. In the very basic definition of the Standard Model however the neutrino mass is assumed to be zero. But it can be easily integrated into the model.
For each fermion in the Standard Model a corresponding antiparticle exists. These are the solutions for the Dirac equation with negative energy. The antiparticles have the same spin and mass values but the opposite electric and color charge, isospin, and lepton number or baryon number. Since bosons do not obey the Pauli principle, the number of bosons with the same quantum state is not restricted. Thus the neutral particles can be their own antiparticle and for the charged W bosons the corresponding partner with inverted charge is the antiparticle. The gluons are also antiparticles among themselves depending on how the octet of color states is constructed.

Every force observable in nature can be deduced from one of four fundamental interactions: The electromagnetic, weak, strong, and gravitational force. One of the great goals of particle physics is to unify even these four forces. The electromagnetic force is described for relativistic processes in the quantum electrodynamics (QED) by Tomonaga, Feynman, and Schwinger. The field theory for the weak interaction was developed by Fermi. Glashow, Weinberg, and Salam then formulated the unification of the electromagnetic and weak interaction into the so called electroweak force. For the strong interaction the theory of quantum chromodynamics (QCD) is used. Gravity is not included in the Standard Model and there is no quantum field theory of gravitation yet, but its strength is negligible for relativistic particle processes compared to the other interactions. An overview of the fundamental interactions can be seen in table 2.2.

Interaction	Strong	Electromagnetic	Weak	Gravity
Field quantum	gluons	photon (γ)	$W^{\pm}$, Z^0	graviton
Mass [GeV]	0	0	80.385 $\pm$0.015, 91.1876 $\pm$0.0021	0
Range [m]	$\leq 10^{-15}$	∞	10^{-18}	∞
Couples to	"color charge"	electric charge	"weak charge"	mass
Coupling constant	$\alpha_S(M_Z) =$ 0.1184	$\alpha(m_e) = \frac{1}{137.04}$	$G_F(m_\mu) =$ $1.17 \cdot 10^{-5}$ GeV^{-2}	$G_N =$ $6.71 \cdot 10^{-39}$ GeV^{-2}

Table 2.2: Properties of the fundamental interactions. Values are taken from [6].

The best understood interaction is the electromagnetic force. The massless photon mediates the interaction between particles with an electric charge.

The strong interaction is mediated by eight charge- and massless gluons. They couple to the color charge of quarks or themselves. The QCD is described by a $SU(3)$ symmetry group. Hence the quantum number corresponding to the charge is divided into three color charges. The color is a conserved quantity like the electrical charge. Since a quark changes its color when it interacts with a gluon, the gluons need to carry a color and an anticolor charge. Composite particles consisting of quarks are called hadrons. A hadron that is composed of two quarks is called meson. A hadron comprised of three quarks is called baryon. Since hadrons are not found in colored versions and single quarks themselves cannot be observed at all, it is assumed that only a color neutral state can exist. This colorless or "white" state is achieved for a combination of one color and its anticolor or for all three colors combined. Hence hadrons consist either of one quark and one antiquark (mesons) or the hadrons are a three quark or antiquark state (baryons). This phenomenon is called quark confinement. It originates from the strong coupling "constant" α_S, which is strongly dependent on the squared four-momentum transfer Q^2. For very low Q^2 corresponding to very high distances the potential increases to infinity. Thus it is not possible to extract a single quark from a color neutral state, it is confined. If the potential energy rises, at a certain point the energy is high enough to produce a new quark antiquark pair. In the new state the distance and the potential are lower and the quarks can also achieve two or more new color-neutral states. This process of producing new quarks during the separation of quarks from an existing neutral state is called hadronisation. In the other extreme of small distances the coupling becomes negligible and particles no longer bound by the strong force can move freely. This behavior is called asymptotic freedom. It was first observed in deep inelastic lepton-nucleon scattering experiments, where the substructure of protons and neutrons was investigated.
The mediators of the weak interaction are massive gauge bosons. Two of these bosons have an electric charge and the third boson is neutral. They are called $W^{\pm}$ and Z^0. The field theory includes two weak coupling constants, one for the coupling of fermions to the neutral boson and one for the coupling of charged bosons. These depend on the electric charge. To unify the electromagnetic and the weak interaction the weak isospin and the weak hypercharge are introduced. This is represented by the $SU(2)_L \otimes U(1)_Y$ symmetry group, where $SU(2)_L$ corresponds to the weak isospin. The index L denotes that only left handed particles are involved. $U(1)_Y$ corresponds to the weak hypercharge, where both chiralities are included. The generators of this combined symmetry group build an isotriplet and an isosinglet of vector bosons. To represent the charged and neutral weak interaction and the electromagnetic interaction, the actual physical bosons need to be linear combinations of the triplet and singlet. The charged bosons $W^{\pm}$ correspond to the weak isospin changing state of the triplet. The neutral Z^0 boson and the photon γ are linear combinations of the singlet and the isospin neutral state of the triplet. This also leads to the relation between the electric and the weak charges with the so-called Weinberg angle θ_W.
The Standard Model is based on the gauge principle. Theories are renormalizable if they provide local gauge invariance. The Standard Model is described by the symmetry group $SU(3)_C \otimes SU(2)_L \otimes U(1)_Y$, which is a combination of the $SU(3)_C$ symmetry

group of the strong interaction and the $SU(2)_L \otimes U(1)_Y$ group for the electroweak interaction. In field theories with local gauge invariance the gauge bosons need to be massless. To provide mass for the W and Z bosons and keep the renormalizability, the concept of spontaneous symmetry breaking is introduced. In a Lagrangian describing the electroweak interactions an $SU(2)_L$ doublet of complex scalar Higgs fields called ϕ^+ and ϕ^0 is included. The potential resembles the bottom of a bottle of wine. Choosing one point as the ground state breaks the symmetry. If the fields are then developed via well chosen fluctuations around this vacuum expectation value some fields obtain a mass term in the corresponding Lagrangian and some terms with field interactions completely vanish. In this process aside of the mass terms for the electroweak gauge bosons a new massive scalar field arises in the Lagrangian. It is named Higgs boson. However, the exact mass of this additional particle is not predicted by the theory. The Higgs boson was not observed in the pre-LHC era and was the last missing particle for the Standard Model to be consistent. But the data of the first LHC run shows evidence of a new particle, which is so far in agreement with the properties of the Higgs boson [16][17].

2.2 Beyond the Standard Model

The prediction of fundamental interactions between particles provided by the Standard Model has been in very good agreement with experimental observations so far. Nevertheless the Standard Model does not describe all observed physical processes and has some inconsistencies. Thus it needs to be extended or replaced to give an even better description of elementary particle physics. In the following the most important open questions and problems are outlined:

- The basic definition of the Standard Model does not include a nonzero neutrino mass, which is strongly suggested by experimental observations. It can be rather easily included in the theory.
- The Standard Model still has a lot of free parameters that are not described by the theory and can only be determined by experimental measurements:
  - six quark masses;
  - three masses of the charged leptons;
  - one weak gauge boson mass ($W^\pm$ or Z^0);
  - one Higgs mass;
  - four weak mixing parameters (3 angles and 1 phase in the CKM-matrix);
  - three coupling "constants" of the three interactions α, α_S, and G_F;
  - one parameter for the strong CP violation.

  If the neutrino masses and oscillations are also included in the theory the number further rises by at least the three neutrino masses and four mixing parameters of the neutrino oscillation matrix.

- Although the LHC experiments show evidence for a new particle similar to the predicted Higgs boson [16][17], many of the properties like spin and parity have yet to be determined with enough significance.

- The Standard Model only unifies the electromagnetic and weak interactions. One additional step to the great goal of the complete unification is to also include the strong interaction by so called Grand Unified Theories (GUT). Possible symmetry groups for GUTs are $SU(5)$ or $SO(10)$. But this does still not include all fundamental interactions. Gravity is still missing. But it is too weak to be relevant at the energy scales of present particle physics experiments and even far beyond. Only at the Planck Scale ($\sim 10^{19}$ GeV) gravity becomes relevant. But then new problems arise with the description of a model as a field theory, because gravity is not renormalizable.

- In GUTs the coupling "constants", which are in fact energy dependent, could be combined at very high energies called the GUT scale $\sim 10^{16}$ GeV. The problem is that without extensions to the present theory the three running couplings do not have one exact intersection. Instead the functions cross each other at three different points (see figure 2.1).

- The huge gaps in mass scales are another open question in the theory. The difference between the weak mass scale $M_W \approx 10^2$ GeV and the Planck Scale ($\sim 10^{19}$ GeV) or the difference between the strengths of the weak force and gravity are called the hierarchy problem.

- From the hierarchy problem additional difficulties for renormalizability arise. Scalar particles like the Higgs boson have quadratic divergences in higher order loop corrections. Without any new physics below the Planck scale this leads to quantum corrections to the Higgs mass that are 30 orders of magnitude larger than the Higgs mass itself. To eliminate the divergences the counter-terms then need to have an unnaturally high precision of around 30 decimal digits. This is called fine-tuning problem.

- Cosmological observations of galaxy rotations and the expansion of the universe have shown that only 4.9% of the universe consist of visible baryonic matter. 68.3% are dark energy and 26.8% are dark matter, which means that 95% of the energy density of the universe are not described by the Standard Model [8].

- Another cosmological observation that cannot be explained with the Standard Model is the asymmetry of matter and antimatter in the universe. CP violation is an important ingredient, but the origin and size of this violation are not described by theory yet and need to be researched.

2.3 Supersymmetry

One of the possible extensions to the Standard Model is the theory of Supersymmetry (SUSY)[9][10][11], with important contributions by Wess and Zumino in 1973 [12][13]. In order to get closer to the great goal of unification the SUSY theory suggests an additional symmetry that transforms bosons into fermions and vice versa. This leads to an additional spectrum of particles which are the bosonic or fermionic supersymmetric partners to the Standard Model particles.
The fundamental transformation would yield particles that have the same properties except for the spin. Because of the same mass, these superpartners would have already been seen in experiments. Since no additional particles have been observed so far, Supersymmetry needs to be broken. The hierarchy problem suggests that the mass scale for SUSY particles should be slightly above the weak scale $M_W \approx 10^2$ GeV. Thus it might be possible to find evidence for particles beyond the Standard Model at the TeV scale reached at the LHC.
By the introduction of new scalar bosons one major problem of the Standard Model can be solved. These new scalar boson fields couple to the Higgs field too and lead to additional terms in the Lagrangian. The loop correction terms cancel with the fermionic loop corrections that yielded the quadratic divergences in the Standard Model. Thus the fine-tuning problem for renormalization vanishes with the introduction of Supersymmetry.
With the introduction of new particles Supersymmetry might also give an explanation for the dark matter. It is possible to construct SUSY models where certain heavy particles are stable and only interact weakly with other particles. These particles could be a candidate for dark matter.

2.3.1 Minimal Supersymmetric Standard Model

In the Minimal Supersymmetric Standard Model (MSSM) the Standard Model is extended with the least amount of additional new particles. Each fermion obtains a Spin 0 partner named after the fermion with an "S" prefix in its name. So they are called sleptons, squarks, or sfermions in general. The gauge bosons are associated with Spin $\frac{1}{2}$ fermions. They are named with the suffix "ino", the so called gauginos.
The Higgs sector needs slightly more adjustments in the MSSM. With only one Higgs field doublet a gauge anomaly would lead to inconsistencies in the field theory. The fermionic partner would lead to divergences. This can be avoided with the use of two Higgs isodoublets with hypercharge $Y = \pm 1$, respectively:

$$\begin{pmatrix} H_1^+ \\ H_1^0 \end{pmatrix}, \quad \begin{pmatrix} H_2^0 \\ H_2^- \end{pmatrix}.$$

Thus the divergent terms of the fermionic Higgs partners cancel each other. In the process of symmetry breaking of two doublet fields not just one but five massive Higgs particles remain, two charged Higgs bosons $H^\pm$, one neutral CP odd particle A, and two neutral CP even particles h, H. Via the breaking of Supersymmetry and the electroweak

symmetry the charged gauginos mix with the charged higgsinos into four eigenstates called charginos $\tilde{\chi}^{\pm}_{1,2}$. The neutral gauginos and higgsinos mix into four neutralino states $\tilde{\chi}^{0}_{1-4}$. An overview of the particles in the MSSM can be seen in table 2.3.

Particle		Spin	Sparticle		Spin
left-handed lepton	l_L	$\frac{1}{2}$	"left-handed" slepton	$\tilde{l}_L$	0
right-handed lepton	l_R	$\frac{1}{2}$	"right-handed" slepton	$\tilde{l}_R$	0
left-handed quark	q_L	$\frac{1}{2}$	"left-handed" squark	$\tilde{q}_L$	0
right-handed quark	q_R	$\frac{1}{2}$	"right-handed" squark	$\tilde{q}_R$	0
gluon	g	1	gluino	$\tilde{g}$	$\frac{1}{2}$
W boson	$W^{\pm}$	1	chargino	$\tilde{\chi}^{\pm}_{1,2}$	$\frac{1}{2}$
charged Higgs	$H^{\pm}$	0			
photon	γ	1	neutralino	$\tilde{\chi}^{0}_{1-4}$	$\frac{1}{2}$
Z boson	Z^0	1			
neutral Higgs	H, h, A	0			

Table 2.3: Standard Model particles and their corresponding SUSY sparticles in the MSSM.

The addition of all the new particles to the gauge group $SU(3)_C \otimes SU(2)_L \otimes U(1)_Y$ also changes the behavior of the running coupling constants associated to each of the subgroups. This enables the unification of the three couplings at one intersection at the GUT scale $\sim 10^{16}$ GeV, which was impossible in the Standard Model (see figure 2.1).
The supersymmetric algebra introduces a new global symmetry with generator R. However, this symmetry has to be discrete, which leads to the new quantum number R-parity, defined as

$$R_P = (-1)^{3(B-L)+2S}, \tag{2.1}$$

where B is the baryon number, L is the lepton number, and S is the spin of a particle. This leads to the fact that all Standard Model particles get an even R-parity ($R_P = 1$), while all supersymmetric particles are associated with an odd R-parity ($R_P = -1$). For the MSSM the R-parity is chosen to be conserved. This ensures the lepton and baryon number conservation and thus the longevity of the proton. It also leads to some striking features for SUSY particles. With R-parity conservation SUSY-particles are always produced in even numbers. On the other hand when a SUSY particle decays, at least one SUSY particle remains after the decay, which leads to the fact that the lightest supersymmetric particle (LSP) has to be absolutely stable. Because an electrically neutral LSP would only interact weakly with other particles, it can be a candidate for cold dark matter. Hence another gap of the Standard Model could be filled with Supersymmetry.
To preserve the cancellation of the quadratic divergences coming from the Standard Model terms and the supersymmetric terms the symmetry breaking needs to be "soft".

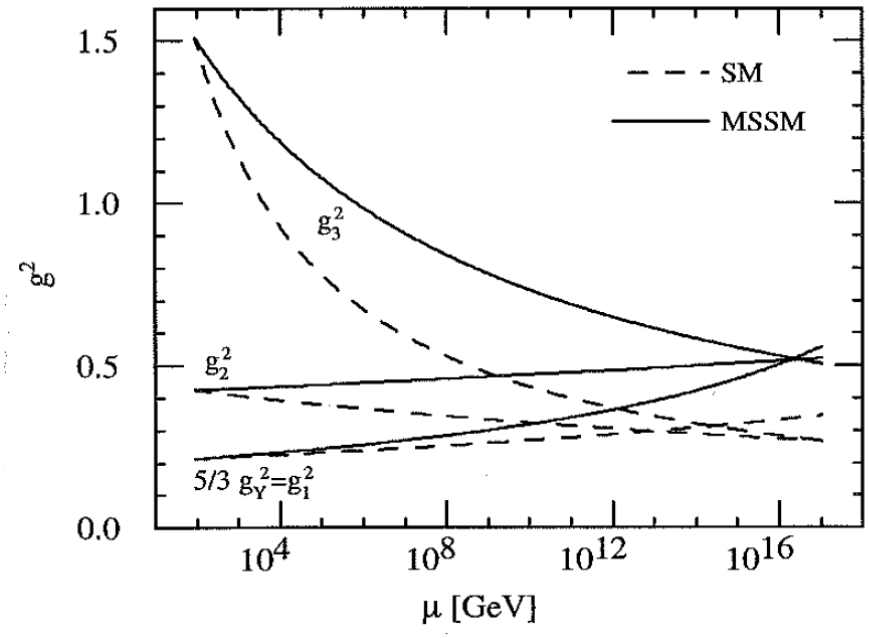

Figure 2.1: The running of the $U(1)$, $SU(2)_L$, and $SU(3)_C$ quadratic gauge coupling strengths above the Z mass scale in the Standard Model (dashed line) and in the MSSM (solid line). [9]

This means that the Lagrangian of the MSSM can be written as follows

$$\mathcal{L}_{MSSM} = \mathcal{L}_{SUSY} + \mathcal{L}_{soft}. \tag{2.2}$$

The first term $\mathcal{L}_{SUSY}$ provides the invariance of Supersymmetry. It comprises gauge, matter, and Higgs-Yukawa interaction terms. $\mathcal{L}_{soft}$ contains soft interaction terms and the mass terms of the heavier sparticles. This provides the SUSY breaking.

2.3.2 The Phenomenological MSSM

Unfortunately the symmetry breaking of SUSY introduces 105 new free parameters, such as all the arbitrary masses, phases, and mixing angles. Therefore models used for SUSY searches include several simplifying assumptions which define the breaking process. Thus the number of free parameters can be massively reduced and then the less arbitrary predictions of those constrained models can be verified by experiment. In the phenomenological MSSM (pMSSM) [18] the following assumptions are made:

- No new source of CP violation in addition to the one from the CKM-matrix in the Standard Model;
- Absence of flavor changing neutral currents at tree level;
- First and second generation of the sfermions have the same masses at low energy scales ($m < 1$ TeV).

These assumptions severely reduce the number of free parameters down to 22. The focus of this thesis are the direct neutralino, chargino, or stau production. Thus only a handful of free parameters play a role like the mass parameters of the gauginos M_1 and M_2, the Higgs mass parameter $|\mu|$, the mass of the stau $m_{\tilde{\tau}}$, and the ratio of the vacuum expectation values of the two Higgs doublet fields $\tan\beta$.
Another approach to reduce the high number of free parameters is to expand the MSSM with a certain model for the SUSY breaking process. Possible models are gravity mediated SUSY breaking (mSUGRA), gauge mediated SUSY breaking (GMSB), or anomaly mediated SUSY breaking (AMSB). Especially the minimal Supergravity model (mSUGRA) has been used, because it provides rather high cross sections at rather low mass parameters. In this model the number of free parameters gets reduced to five, the scalar mass parameter m_0, the gaugino mass parameter $m_{\frac{1}{2}}$, the trilinear coupling parameter A_0, the sign of the Higgs mass parameter, and the ratio of the vacuum expectation values of the two Higgs doublets $\tan\beta$.

2.3.3 Simplified Models

Another approach are the simplified models [14][15]. In these models a particular short decay chain defines the parameter space. Therefore the model is built with the minimal particle content necessary to produce such a process. As an advantage such models can be parametrized directly with the small amount of different particle masses. Although simplified models are not describing a complete SUSY model, they can be used effectively as a starting point to develop a SUSY model if deviations to the Standard Model can be found in data. Moreover due to the few parameters it is possible to identify kinematic ranges and event topologies very clearly. With limits on simplified models it is possible to derive constraints on a variety of SUSY models.

2.3.4 Constraints on SUSY

The search for SUSY particles at collider experiments has not been successful so far. Only exclusion limits on the cross-sections of the production processes of SUSY particles have been established. These limits set constraints on the parameter spaces of the various SUSY models.
Figure 2.2 shows the exclusion limits for the parameter space of mSUGRA, that have been determined at the detectors of the Tevatron [19] and the LEP [20] colliders.
The LHC experiments cover a wide range of SUSY models. With data recorded in the years 2011 and 2012 the constraints on SUSY models have been further improved. An overview of the recent (2013) mass boundaries set by the ATLAS collaboration [21] can be seen in figure 2.3.

2.3.5 Production of SUSY Particles

At the LHC SUSY particles are produced from the interaction of the partons in the proton. Thus only gluons and quarks are available at the hard scattering process to pro-

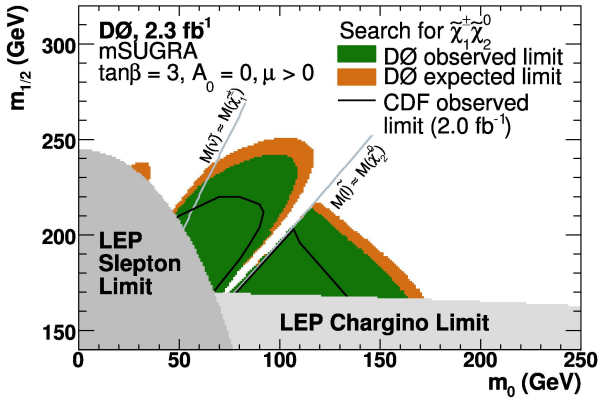

Figure 2.2: Limits in the m_0-$m_{\frac{1}{2}}$ plane provided by the DØ Collaboration [19], also including results from LEP and the other Tevatron detector CDF.

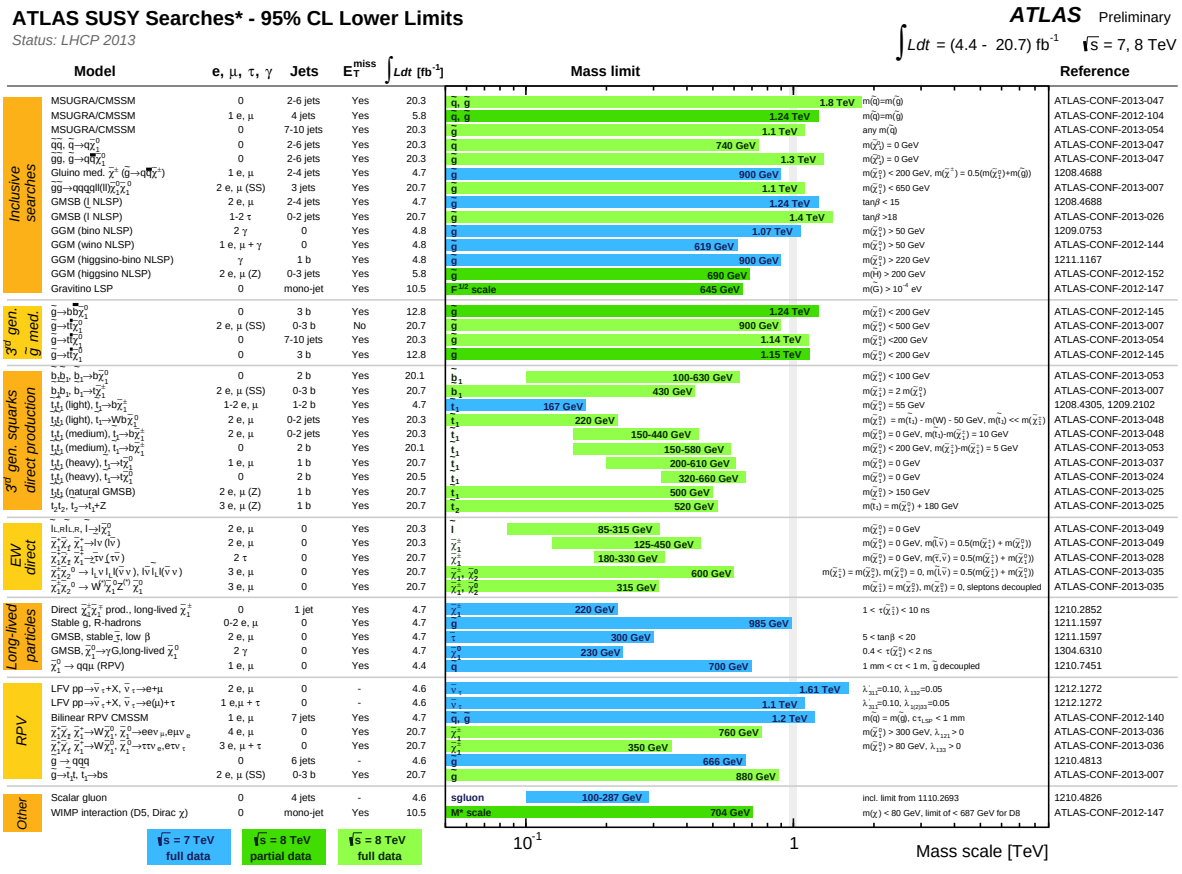

*Only a selection of the available mass limits on new states or phenomena is shown. All limits quoted are observed minus 1σ theoretical signal cross section uncertainty.

Figure 2.3: Mass reach of ATLAS searches for Supersymmetry [21].

duce a pair of SUSY particles. The dominant processes are strong production processes where gluinos and squarks are produced in a gluon fusion process with other gluons or quarks, in a quark-antiquark annihilation, or in a quark-quark scattering. The Feynman diagrams for such processes can be seen in the figures 2.4 and 2.5.

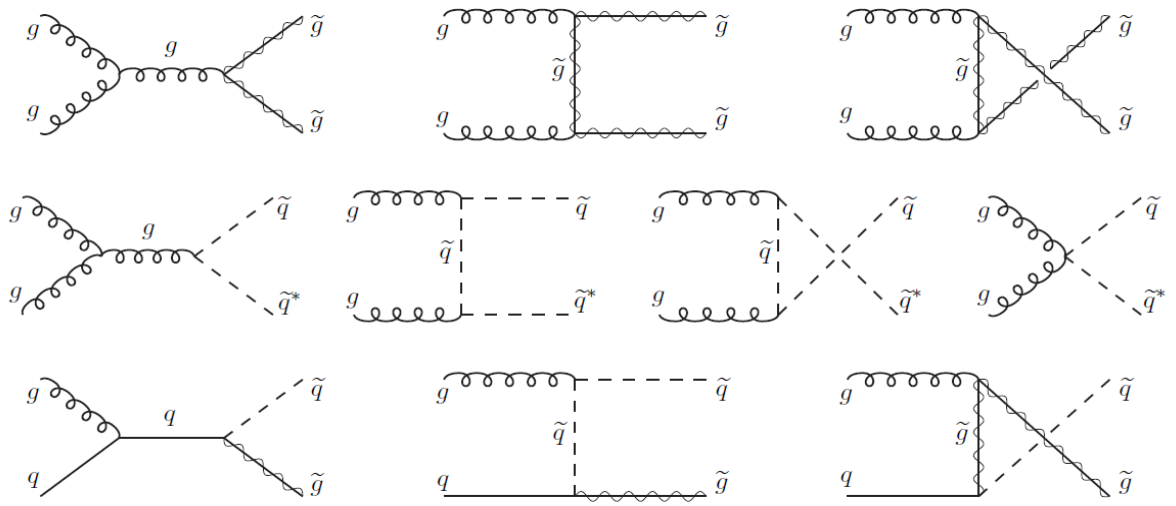

Figure 2.4: Feynman diagrams for gluino and squark production at hadron colliders from gluon-gluon and gluon-quark fusion. [10]

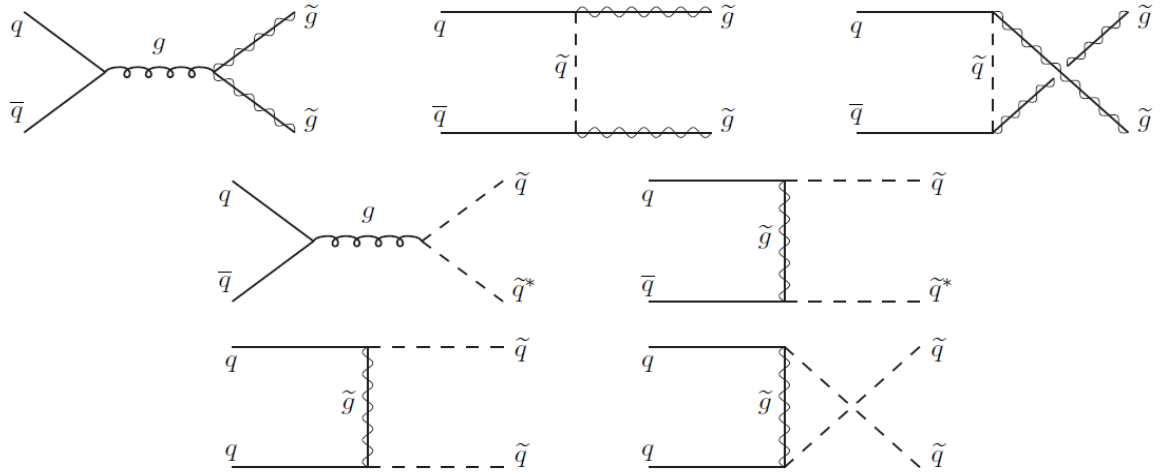

Figure 2.5: Feynman diagrams for gluino and squark production at hadron colliders from strong quark-antiquark annihilation and quark-quark scattering. [10]

Electroweak production processes that lead to a direct production of neutralinos, charginos, or sleptons are highly suppressed with a much lower cross section. They might

become the dominant SUSY interaction if the energy of the collision process is below the mass scales of squarks and gluinos. Feynman diagrams for electroweak sparticle production can be seen in figure 2.6. The cross sections of SUSY particle production processes at the LHC for proton-proton collisions at a center of mass energy of $\sqrt{s} = 8\,\text{TeV}$ can be calculated with the prospino program [22]. They are shown in figure 2.7.

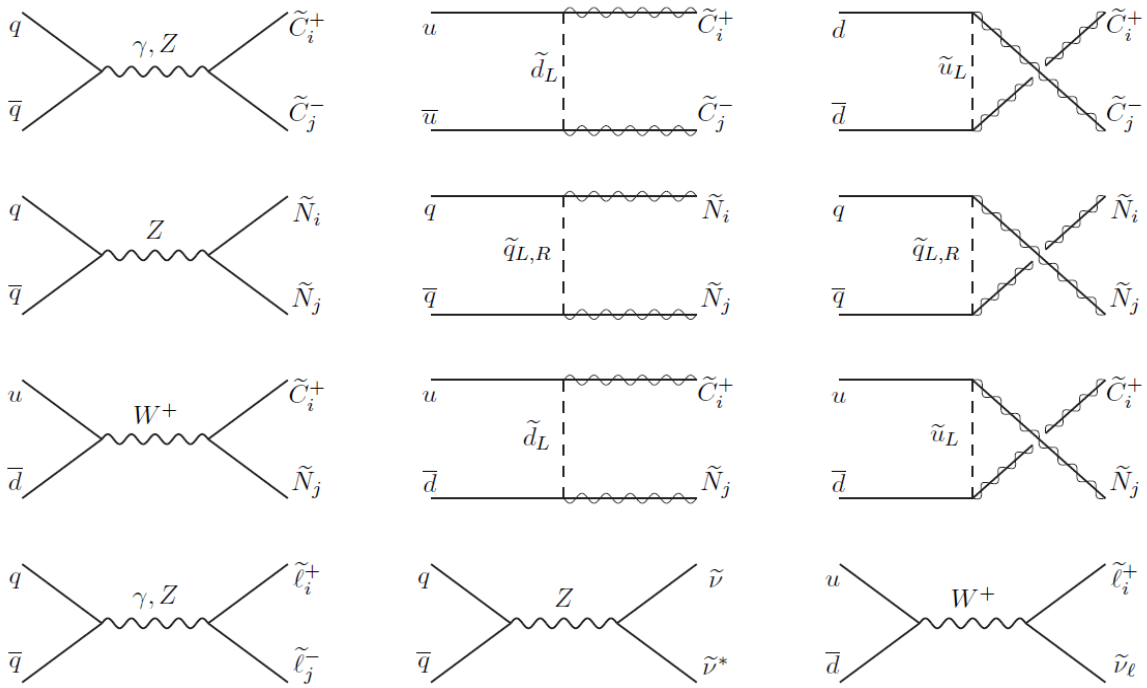

Figure 2.6: Feynman diagrams for electroweak production of sparticles at hadron colliders from quark-antiquark annihilation. [10]

2.3.6 Decay of SUSY Particles

Since R-parity is assumed to be conserved in the MSSM a SUSY particle will always decay into another lighter sparticle until the decay process reaches the stable lightest sparticle, the LSP. The LSP is assumed to be the lightest neutralino $\tilde{\chi}_1^0$ throughout the SUSY models used for the analysis in this thesis.

- **Charginos and Neutralinos**
  The charginos and neutralinos are a mixture of the higgsinos and the electroweak gauginos. Thus they have an electroweak coupling and can decay into fermion boson pairs with one being a Standard Model particle and one a sparticle:

$$\tilde{\chi}_i^0 \rightarrow \quad Z^0\tilde{\chi}_j^0, \quad W^{\pm}\tilde{\chi}_j^{\mp}, \quad h^0\tilde{\chi}_j^0, \quad l\tilde{l}, \quad \nu\tilde{\nu}$$

$$\tilde{\chi}_i^{\pm} \rightarrow \quad W^{\pm}\tilde{\chi}_j^0, \quad Z^0\tilde{\chi}_j^{\mp}, \quad h^0\tilde{\chi}_j^{\pm}, \quad l\tilde{\nu}, \quad \nu\tilde{l}$$

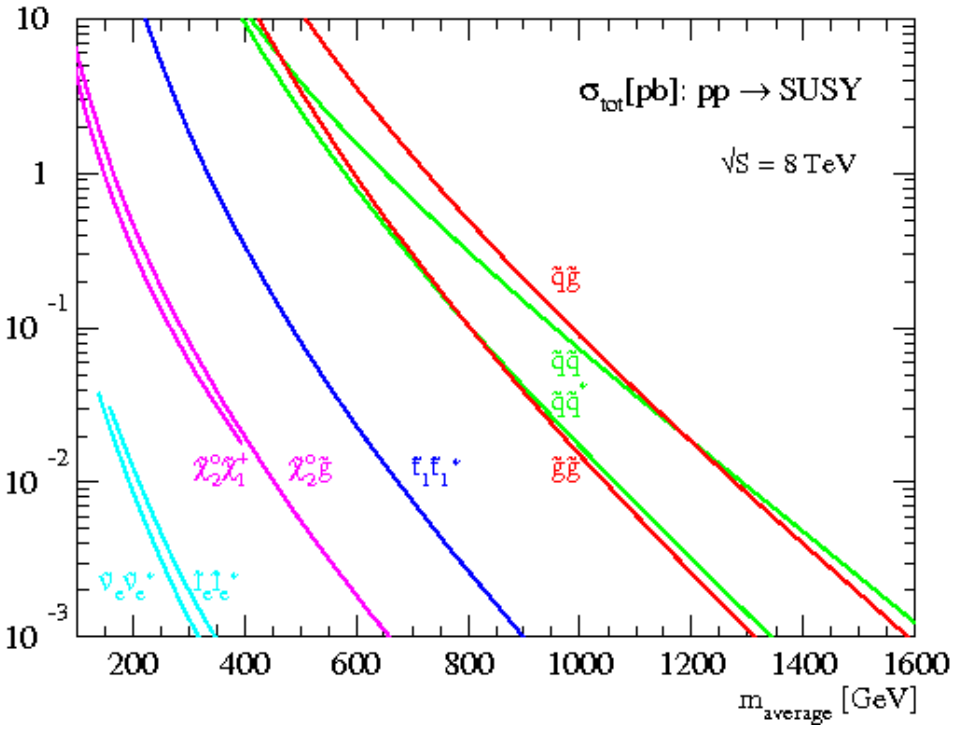

Figure 2.7: Cross-sections of various SUSY production modes from proton-proton collisions at $\sqrt{s} = 8\,\text{TeV}$. [22]

Here index j denotes a lighter neutralino or chargino than the decaying particle with index i. A decay into a heavier Higgs boson and a chargino or neutralino or the decay into a quark-squark pair is also possible in general. But in most models the other four Higgs bosons and the squarks are at a higher mass scale than the neutralinos and charginos.
It is also possible that a three-body decay into a fermion-antifermion pair together with a sparticle might occur if the other processes are all kinematically forbidden:

$$\tilde{\chi}_i^0 \to \quad f\bar{f}\tilde{\chi}_j^0, \quad f\bar{f}'\tilde{\chi}_j^{\mp}$$

$$\tilde{\chi}_i^{\pm} \to \quad f\bar{f}'\tilde{\chi}_j^0, \quad f\bar{f}\tilde{\chi}_j^{\mp}$$

Index j denotes a lighter neutralino or chargino than the decaying particle with index i. f' is a different fermion from f. The fermions in this case might be leptons or quarks.

- **Sleptons**
  Sleptons decay into a Standard Model lepton and a chargino or neutralino. Usually the direct decay into LSP will be the dominant process, but if the slepton is sufficiently heavy the other neutralinos and charginos also come into consideration.

$$\tilde{l} \to \quad l\tilde{\chi}_i^0, \quad \nu\tilde{\chi}_i^{\pm}$$

$$\tilde{\nu} \rightarrow \quad \nu\tilde{\chi}_i^0, \quad l\tilde{\chi}_i^{\pm}$$

- **Squarks**
  Squarks can have vertices with strong coupling strength. Thus the decay into a quark and a gluino will be dominating. But electroweak decays into a quark and a neutralino or chargino are possible decay modes as well.

$$\tilde{q} \rightarrow \quad q\tilde{g}, \quad q\tilde{\chi}_i^0, \quad q'\tilde{\chi}_i^{\pm}$$

- **Gluinos**
  Gluinos can only decay into squarks.

$$\tilde{g} \rightarrow \quad q\tilde{q}$$

  If the gluino mass is actually below each squark mass, the decay is realized via an off-shell squark in a three-body decay into a quark pair and a neutralino or chargino.

$$\tilde{g} \rightarrow \quad q\bar{q}\tilde{\chi}_i^0, \quad qq'\tilde{\chi}_i^{\pm}$$

3 Experimental Setup

3.1 The Large Hadron Collider (LHC)

At the European Organization for Nuclear Research (CERN) [23] near Geneva the Large Hadron Collider (LHC) [24] has been built. This high energy particle accelerator is designed for the discovery of the Higgs boson and physics beyond the Standard Model. It is located 100 m underground in a circular 27 km long tunnel which was formerly used for the Large Electron Positron Collider (LEP) from 1989 to 2000. In the LEP experiment electrons were collided with positrons at center of mass energies up to 209 GeV. The synchrotron radiation of the light particle beams prevented the reach of higher energies with the same diameter of the accelerator. In order to reach even higher energies, the following accelerator was designed to be a proton-proton collider, which is not limited by the synchrotron radiation because of the much higher proton mass ($m_p \approx 2000 m_e$). The LHC was designed to have a center of mass energy of $\sqrt{s} = 14\,\text{TeV}$ with a luminosity of $L = 10^{34} cm^{-2} s^{-1}$. A schematic overview of the LHC and the experiments is shown in figure 3.1.

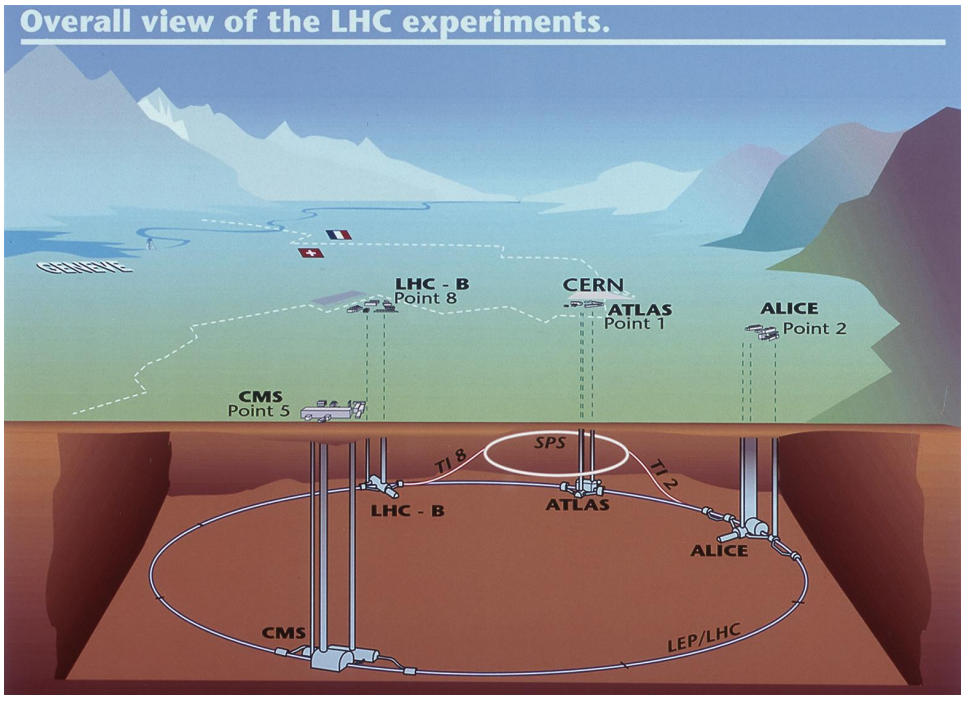

Figure 3.1: Pictorial representation of the LHC at CERN and the position of the experiments. [25]

The protons for the LHC are provided by the injector chain Linac2 - Proton Synchrotron Booster (PSB) - Proton Synchrotron (PS) - Super Proton Synchrotron (SPS). The Linac2 is a linear accelerator, while the other parts of the injector chain are ring shaped accelerators. The Linac2 was upgraded for the LHC to provide a 180 mA current with 50 MeV protons for the PSB. In the following accelerators the proton energy is further increased from 1.4 GeV (PSB) over 26 GeV (PS) until the LHC injection energy of 450 GeV in the SPS.
From the SPS the protons are injected into the LHC ring via two transfer lines, where the two proton beams are rotating around the tunnel in opposite directions in separated vacuum tubes. The protons are injected in bunches of up to $1.5 \cdot 10^{11}$ protons with a bunch spacing of 50 ns (design values are 10^{11} protons per bunch with a bunch spacing of 25 ns). To direct them around the circle and keep them focused the same magnets are used for both beams. These magnets consist of two sets of coils and beam channels so that both pipes can be within the same mechanical structure and cryostat. There are 1232 superconducting dipole magnets with a magnetic field strength of up to 8.33 T around the circle to keep the beams on their track. To keep the beams focused there are 392 superconducting quadrupole magnets and additional multipole magnets for beam correction installed. In total the LHC uses 9593 magnets.
The proton beams are led to collision at four points around the LHC ring. At these interaction points the main experiments are located, the two general-purpose detectors ATLAS and CMS, the LHCb detector aiming for B-physics, and the ALICE detector, which is focused on the collisions of heavy ions.
The first beams were circulated successfully on 10th September 2008. On the 19th of September 2008 an incident occured, which destroyed several superconducting magnets and it became clear that the design beam energy of 7 TeV cannot be reached without additional safety upgrades to the beam magnet system.
Data taking started on the 30th of March 2010. Proton-proton collisions have been performed with a beam energy of 3.5 TeV in 2010 and 2011 and with 4 TeV in 2012. In 2010 a total integrated luminosity of $48.1\,\mathrm{pb}^{-1}$ was delivered to the ATLAS experiment. In 2011 it was $5.61\,\mathrm{fb}^{-1}$ and in 2012 it was $23.3\,\mathrm{fb}^{-1}$. At the end of 2010 and 2011 also lead-lead collisions and at the beginning of 2013 proton-lead collsions have been performed. After the 10th of February 2013 the LHC was shut down to upgrade the accelerator and experiments to run at the full design energy in the future.

3.2 The ATLAS Experiment

At interaction point 1 of the LHC the ATLAS (**A** **T**oroidal **L**HC Apparatu**S**) [26][27] experiment is installed. A schematic overview of the detector is shown in figure 3.2. It is designed for detailed studies of a broad spectrum of physics processes in collisions at the TeV scale. The detector is required to have very good calorimetry for precise electron, photon, jet, and missing transverse energy (E_T^{miss}) measurements (E_T^{miss} is defined in section 4.3.5). It is also demanded to have a high precision in tracking leptons and identifying taus, photons, and heavy flavor objects. In addition the detector acceptance

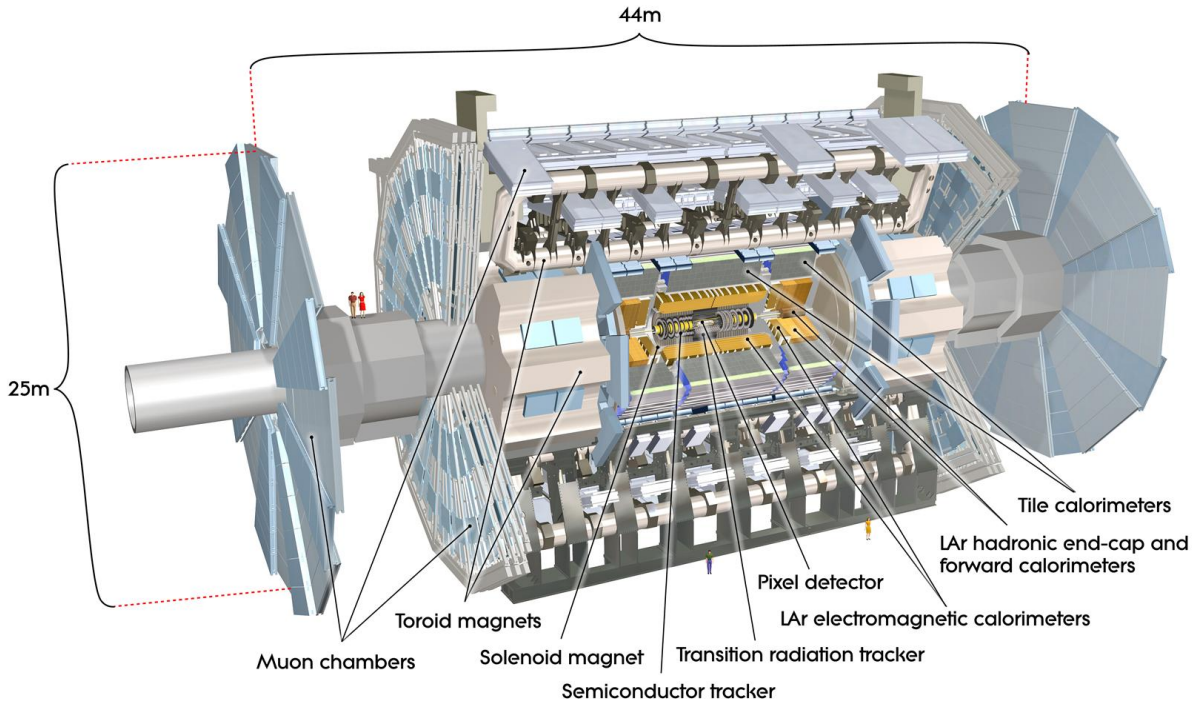

Figure 3.2: The ATLAS-Detector. [25]

should cover a wide spherical area around the interaction point. The detector is built in several concentric layers of subdetector systems around the interaction point. All subdetectors are built in a cylindrical shape along the beam axis. Around the interaction point in the beampipe the first subdetector is the inner detector for tracking charged particles, which is surrounded by a solenoid magnet. The next layer are the electromagnetic and hadronic calorimeters measuring the energy deposits of charged and neutral particles, which get absorbed by interacting with the detector material. The outermost subdetector system is the muon spectrometer, a second tracking device for muons, which are the only visible particles of the Standard Model that can pass the calorimeters. The complete detector is 46 m long, has a diameter of 25 m and a weight of 7000 t. It is the largest detector at the LHC.

3.2.1 Coordinate System

For the ATLAS Detector a right handed coordinate system is used, in which the z-axis is along the beam direction and the $x-y$-plane is perpendicular to the beam. The x-axis points towards the center of the LHC ring and the y-axis points upward. The azimuthal angle ϕ is defined in the $x-y$-plane starting from the x-axis at 0° and pointing to the y-axis at 90°. The polar angle θ is the angle from the z-axis. The coordinate system is depicted in figure 3.3. As a useful alternative representation for the polar angle the

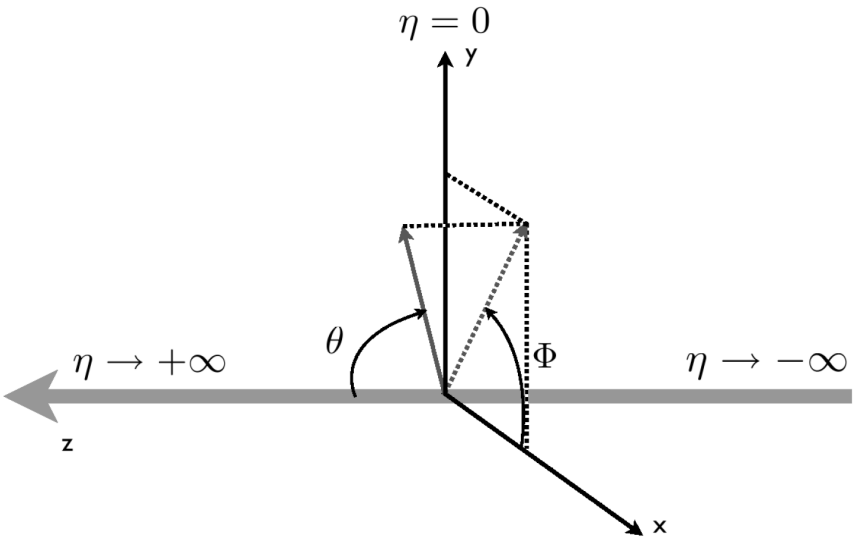

Figure 3.3: ATLAS coordinate system. [28]

pseudorapidity is used, defined as:

$$\eta = -\ln(\tan\frac{\theta}{2}). \tag{3.1}$$

Often used is the transverse mapping of vector variables like the transverse momentum p_T, which is defined as the projection into the $x-y$-plane. Another useful variable is the distance ΔR in the pseudorapidity-azimuthal angle space ($\eta - \phi$-plane), defined as:

$$\Delta R = \sqrt{\Delta\eta^2 + \Delta\phi^2}. \tag{3.2}$$

3.2.2 The Magnet System

To measure the charge and the momentum of particles in the inner detector and the muon spectrometer, the tracks of the particles are bent with magnetic fields. Because the deflection via the Lorentz force is proportional to the momentum and the charge of a particle moving through a magnetic field, the momentum can be calculated with a given magnetic field strength and the charge can be determined from the curvature of the track. Hence the inner detector is surrounded by a solenoid and in the muon spectrometer a toroid magnetic system is embedded. The superconducting magnets are cooled with a forced helium flow at 4.5 K.

- The **central solenoid** is the superconducting magnetic system surrounding the inner detector. The position between the interaction point and the calorimeters where the total energy gets measured leads to the additional requirement to be as thin as possible. The central solenoid has an inner diameter of 2.44 m and is about 10 cm thick. Its length is 5.3 m. It provides a magnetic field of 2 T with a peak at the superconductor of 2.6 T.

- The bending in the muon spectrometer is provided by three **toroid magnets**, one barrel toroid and two end-cap toroids. The toroids are each composed of eight coils with air-cores assembled symmetrically around the beam axis. The average magnetic field strengths is 0.5 T, with a peak magnetic field strength of 3.9 T in the barrel region and 4.1 T in the end-caps. The overall length of this cylindric setup is 25 m with a diameter of 20 m. The magnetic field is provided in an η-range of 0-1.3 for the barrel toroid and 1.6-2.7 for the end-caps, while in the transition region $1.3 < |\eta| < 1.6$ the magnets overlap and the bending power is lowered.

3.2.3 The Inner Detector

The inner detector is the subsystem of ATLAS closest to the interaction point. A schematic overview of the inner detector is shown in figure 3.4. To reconstruct tracks of charged particles with a very high resolution, the detection has to be as close as possible to the interaction point. Therefore the detection starts at a radius of 5 cm with several layers of high resolution semiconducting pixel detectors and continues with layers of straw detectors at the outer part of the inner detector. The inner detector has a radius of 1.15 m and a length of 7 m. All subsystems cover a spatial area of up to $|\eta| \leq 2.5$. Typically particles pass 47 layers of detecting devices. Together with the curvature of the track provided by the 2 T magnetic field of the central solenoid it is possible to measure direction and momentum of charged particles with a very high precision. Moreover the inner detector is able to get information about the impact parameter, secondary vertices, and the decay of short lived particles like τ's and b quarks.
The inner detector is divided into three subsystems:

- **Pixel detector**
  The pixel detector is the closest subsystem to the interaction point. It provides the best granularity of all subsystems. The pixel detector consists of three concentric layers in the barrel region with radii of 5, 9, and 12 cm and three disks in the end-cap region on each side. Typically a particle crosses three pixel layers on its track. With three very high precision measurements it is the main source of information about deviations of the track from the primary vertex, such as b quark or τ decays. The barrel consists of 1456 and the disks of 288 modules. Each module is 62.4 mm long, 21.4 mm wide, and has 46080 pixel elements, making it a total of $\sim$ 80 million pixels. The resolution of a single pixel is 50 μm in Rϕ direction and 300 μm in z. Due to the high frequency of particles passing through the material has to withstand a radiation of over 300 kGy and is subject to be changed during the shutdown phases. During the first long shutdown starting in early 2013 a fourth pixel layer is going to be installed [29].

- **Semiconductor tracker (SCT)**
  Surrounding the pixel detector is the semiconductor tracker. It is comprised of silicon microstrip detectors with 6.2 million readout channels. One strip has a width of 80 μm and is 12.8 cm long. The barrel SCT has 4 cylindrical layers of

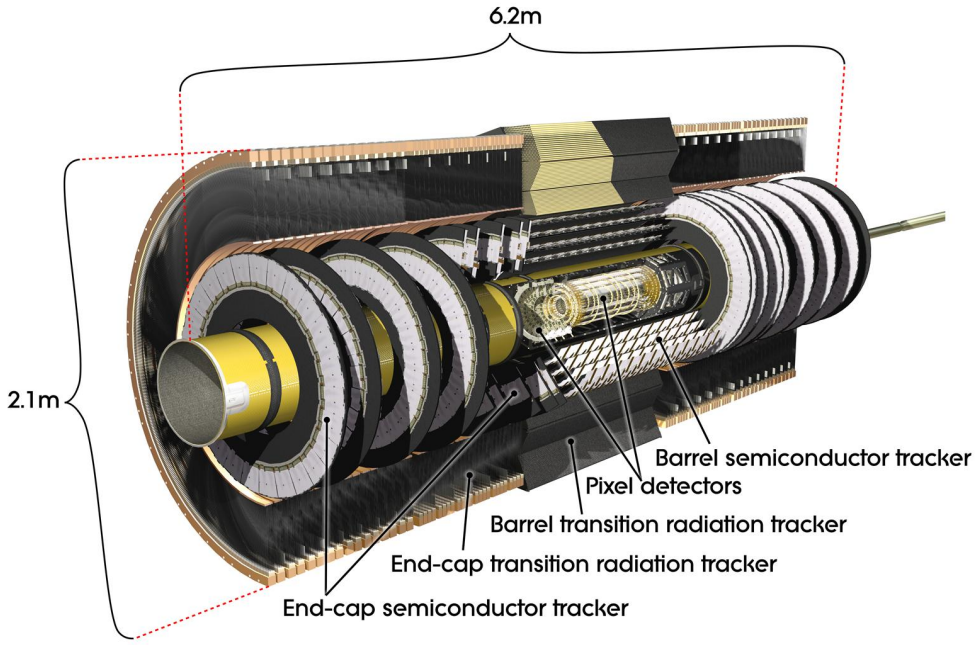

Figure 3.4: The layers of the ATLAS inner detector subsystem. [25]

double sided silicon detectors axially aligned to the beam, so that 4 precise space points can be reconstructed at radii of 30, 37, 44, and 52 cm. The end-cap region is built from nine wheels of tapered microstrip detectors which are perpendicular to the beam axis. The resolution is 16 μm in Rϕ and 580 μm in z. With typically 8 precision measurements per track the SCT is contributing to the determination of the momentum of particles, the impact parameter of a particle track, and the vertex position.

- **Transition radiation tracker (TRT)**
  The outermost part of the inner detector is built with straw detectors, that can operate at high detecting rates. They have lesser granularity than semiconductor detectors, but are much cheaper, and the lower resolution is compensated by a large number of measurements and overall higher range of radii at which a measurement is performed. Because of the high number of layers the TRT also has a significant impact on the momentum measurement. Moreover not only the tracks are reconstructed. By the measurement of transition radiation photons in a Xenon dominated gas mixture an additional discrimination method between the light electrons and hadrons is provided. The transition radiation increases with the speed of a crossing particle. So for a given momentum the radiation is stronger for lighter particles.
  In a radial range from 56 to 107 cm in the barrel area and 18 wheels in the end-caps a much bigger number of track points can be measured than in the semiconductor detectors. Typically 36 straw hits are detected per track. Each straw has a 4 mm

diameter and inside is a 30 μm diameter gold-plated W-Re wire. The maximum length of a straw is 144 cm. There are about 50000 straws oriented along the beam axis in the barrel region each divided into two in the middle. The end-caps consist of 320000 radial straws, making it 420000 straws in total. With a precise drift-time measurement, a spatial resolution of 170 μm per straw is obtained. The gas mixture in the TRT is composed of Xe(70%)CO_2(27%)O_2(3%) and has a total volume of 3 m^3.

3.2.4 The Electromagnetic Calorimeter

After the tracking and momentum measurement in the inner detector, the following two layers of subdetectors are aiming for the energy measurement of the particles produced in the collision. The first subsystem is the electromagnetic (EM) calorimeter, which is focused on the detection of the mostly electromagnetically interacting photons and electrons. While these lighter particles are completely absorbed and deposit their entire energy via an electromagnetic shower in this calorimeter, the heavier hadrons and muons pass through this detector part without loosing too much energy. A schematic overview of the electromagnetic calorimeter is shown in figure 3.5.

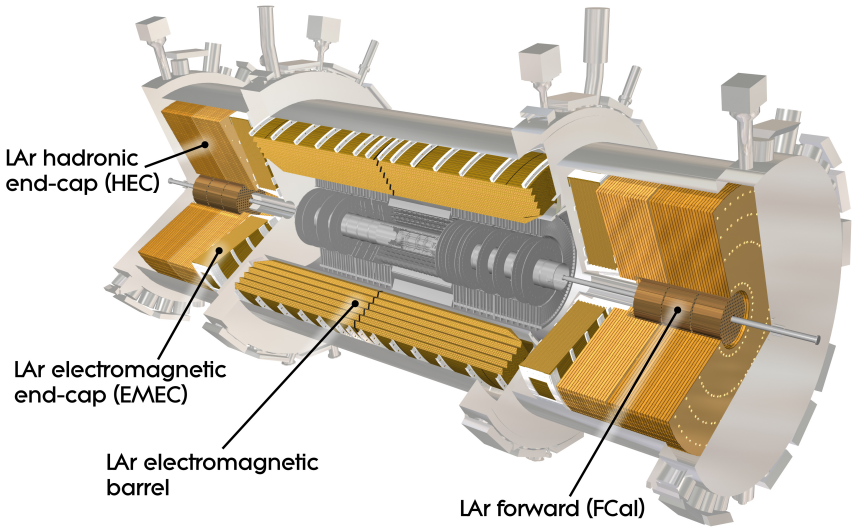

Figure 3.5: The liquid argon calorimeter. [25]

The electromagnetic calorimeter is built with liquid argon (LAr) as active material and has accordion-shaped electrodes and lead plates as absorber. To correct the energy lost in the material of the ID, solenoid, and cryostat, which corresponds to more than 2.3 radiation lengths, a presampler detector is installed upstream the calorimeters.
The EM calorimeter has a radius of 2.25 m and is 13.3 m long. It covers a pseudorapidty

range of $|\eta| < 3.2$. It is divided into a cylindrical barrel part, which covers $|\eta| < 1.475$, and two end-caps at each side, which are divided into an outer wheel covering $1.375 < |\eta| < 2.5$ and an inner wheel covering $2.5 < |\eta| < 3.2$. The EM calorimeter thickness covers more than 24 radiation lengths (X_0) in the barrel region (more than 26 in the end-caps). The detector is then further divided in regions of different granularity. The first is the strip section, which has a thickness of 6 X_0 and consists of thin strips with a pitch of only ∼4 mm in η direction. It helps analyzing preshowers and increases the particle discrimination performance between photons and π^0 or electrons and $\pi^{\pm}$, because the pions are not directly starting an electromagnetic shower. With its resolution of $\Delta\eta \times \Delta\phi = 0.003 \times 0.1$ it provides precise position measurement in η. Until the end of the middle section particles have passed around 24 X_0. It is segmented into square towers with a resolution of $\Delta\eta \times \Delta\phi = 0.025 \times 0.025$. The back section comprises the last 2-12 X_0, with a lowered resolution of $\Delta\eta \times \Delta\phi = 0.05 \times 0.025$. The total number of channels is ∼190000. The confirmed energy resolution of the EM calorimeter is:

$$\frac{\Delta E}{E} = \frac{10\%}{\sqrt{E/[\mathrm{GeV}]}} \oplus 1\% \tag{3.3}$$

3.2.5 The Hadronic Calorimeter

The next subsystem is the hadronic calorimeter. This part of the detector absorbs the hadrons that have passed the EM calorimeter. Via strong interactions with the detector material the hadrons decay in a so-called hadronic shower. To absorb the entire energy of all hadrons that can be produced at the center of mass energy of the LHC the hadronic calorimeter has to be thick enough. Otherwise the particles produced in a hadronic shower would pass the calorimeters and get to the muon spectrometer behind. The energy could not be measured precisely anymore and the detection in the muon spectrometer would also be affected. Therefore the diameter has been chosen to be 11 interaction lengths (λ). Around 10 λ are enough to obtain a good jet resolution at high energies and reduce the punch-through to a level where only prompt and decay muons pass the calorimeter. A schematic overview of the hadronic calorimeter is shown in figure 3.6.
The hadronic calorimeter has a radius of 4.25 m and a length of 12.2 m. Over its wide pseudorapidity coverage of $\eta < 4.9$ several detecting techniques are used to cope with the different radiation load. The hadronic barrel calorimeter covering $|\eta| < 1.7$, also called tile calorimeter, consists of 3 sections, a central barrel and two extended barrels. It is a sampling calorimeter with plastic scintillator plates (tiles) as the active material and is embedded into an iron absorber. The resolution is $\Delta\eta \times \Delta\phi = 0.1 \times 0.1$ (0.2×0.1 in the last layer). There are about 10000 readout channels in total. The hadronic end-cap calorimeters (HEC) cover a range of $1.5 < |\eta| < 3.2$ and the wheels have an outer radius of 2.03 m. This calorimeter uses the more radiation resistant LAr technology like the EM calorimeter with copper absorbers. The subsystem of the hadronic calorimeter closest to the beam pipe ($3.1 < |\eta| < 4.9$) and hence exposed to the highest radiation is the forward calorimeter (FCAL). It is a dense LAr calorimeter with rod-shaped electrodes

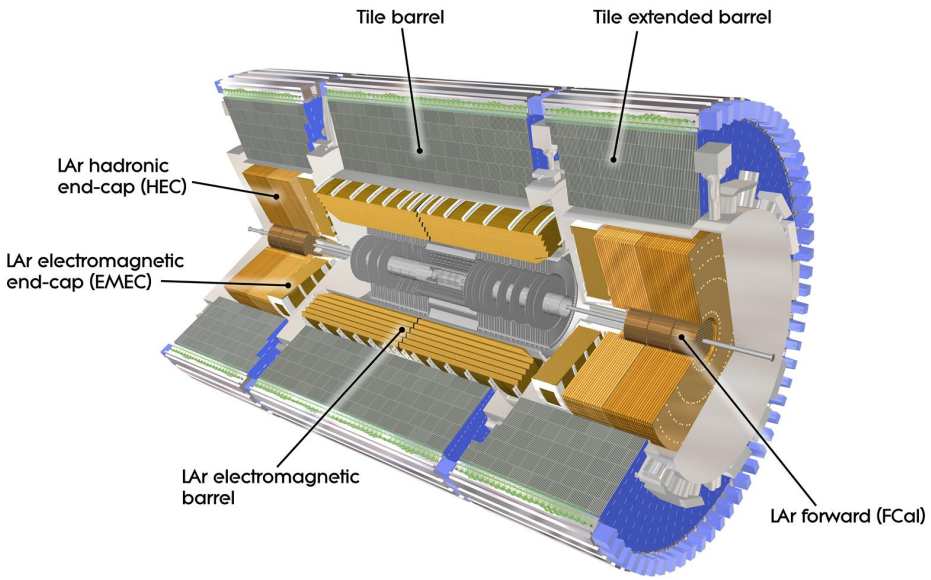

Figure 3.6: The calorimeter layers of the ATLAS-Detector. [25]

in a tungsten matrix.
The hadronic calorimeter reaches an energy resolution of:

$$\frac{\Delta E}{E} = \frac{50\%}{\sqrt{E/[\text{GeV}]}} \oplus 3\% \tag{3.4}$$

3.2.6 The Muon-Spectrometer

Muons are the only directly measurable particles in the Standard Model that are able to pass the calorimeters, because they do not strongly interact with the material and are massive enough to not produce an electromagnetical shower as quickly as electrons. Their track and momentum can also be determined in the inner detector. But to improve this identification and distinguish the muons from other charged particles, another independent tracking detector, the muon spectrometer (MS), is built around the calorimeters. A schematic overview of the muon spectrometer is shown in figure 3.7.
Three concentric cylinder layers (stations) in the barrel cover $|\eta| < 1$ and have radii of 5, 7.5, and 10m. This is optimized to be near the inner and outer field boundaries and directly inside the magnetic field of the toroids. The end-cap range is $1 < |\eta| < 2.7$. There are four disks at 7, 10, 14, and 21-23m from the interaction point along the beam line. The last layer of the forward muon chambers is mounted on the cavern wall. The energy resolution of the spectrometer depends on the momenta of the muons and ranges from 4% to 10%. In total there are 1232000 readout channels in the spectrometer.

- The precision measurement is mostly done with **Monitored Drift Tubes** (MDTs). The aluminium tubes used have a diameter of 30 mm, 400 μm wall

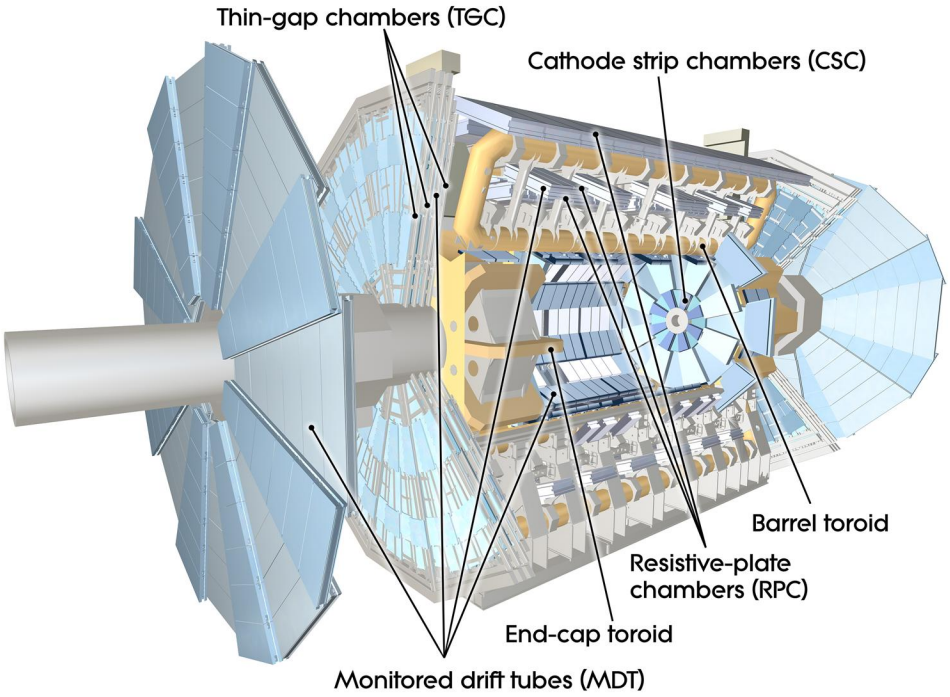

Figure 3.7: The muon spectrometer at the ATLAS-Detector. [25]

thickness, and have a 50 μm W-Re wire inside. A mixture of $Ar(93\%)CO_2(7\%)$ gas at 3 bar floats through the tubes. The MDTs provide 80 μm resolution per wire and have a maximum drift time of $\sim$ 700 ns.

- To deal with the higher rates in the forward direction, **Cathode Strip Chambers** (CSCs) with high granularity are used in the inner plane at $2 < |\eta| < 2.7$. They are multiwire proportional chambers. With an anode wire pitch of 2.54 mm and cathode readout pitch of 5.08 mm position resolutions of 60 μm and time resolutions of 7 ns are possible. The baseline CSC gas mixture consists of $Ar(30\%)CO_2(50\%)CF_4(20\%)$.

- The triggering system covers a range of $|\eta| < 2.4$, with better time resolution ($\sim$ 1 ns). The **Resistive Plate Chambers** (RPCs) in the barrel and **Thin Gap Chambers** (TGCs) in the end-cap regions are used for the triggering. There are three RPC stations located on both sides of the middle MDT layer and inside the outer station. Likewise there are three stations of TGCs, which are near the middle MDT end-cap station.

The only Standard Model particles that are not visible in the detector directly or via their decay products are the neutrinos. Since they carry no electric charge and only interact weakly, the neutrinos pass the detector material without detection. However they can be indirectly measured by accounting the transverse momenta of all visible

particles and checking for imbalances in the event. For a completely reconstructed event the vectorial sum of all transverse momenta should be 0, since the proton collision did not have any momentum in the $x - y$ plane (see section 4.3.5).

3.2.7 The Trigger System

With the aforementioned bunch spacing of 50 ns (25 ns nominal) the event rate is 20 MHz (40 MHz respectively). It is not possible for the computing system to record and store events in such a high rate. Hence the data acquisition has to be lowered by a three step triggering system to a nominal rate of a few hundred Hz. The actual rate of data taking in the year 2012 is shown in figure 3.8. A diagram giving an overview of the trigger system is given in figure 3.9.

- **Level 1 trigger**: The first hardware filter tries to identify rather coarse-grained regions of interest (ROI). Only information with lower granularity from the calorimeters and from the trigger chambers of the muon spectrometer are used for this first classification. With this very raw physical objects like leptons, jets, or missing transverse energy can be defined. The trigger decision is then based on a combination of objects being present in coincidence. This already reduces the event rate to $\sim$ 100 KHz. The required latency for the trigger decision is lower than 2.5 μs.

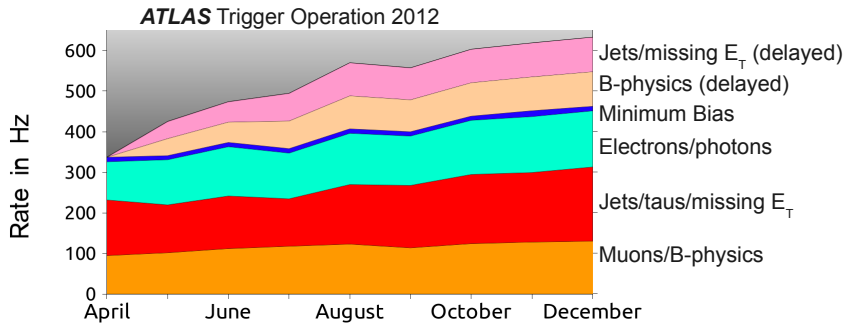

Figure 3.8: Event Filter rates per month, averaged over the periods for which the LHC declared stable beams (2012 at 8TeV). [30]

- **Level 2 trigger**: The events selected by the Level 1 trigger are then seeded into the software readout system. The ROI defined before are investigated with the full detector information at the full resolution by the software based Level 2 trigger. With more information about the event topology and higher quality requirements the rate is further reduces to $\sim$ 4KHz.

- **Event filter**: The last step of the online selection is the Event filter. With tighter criteria than the Level 2 trigger and more sophisticated offline algorithms it finally

decides which events get written to mass storage. This filter further reduces the rate to 400-600 Hz which then corresponds to a data rate of $\sim$ 1 GB/s.

The data measured with the ATLAS detector is recorded in several different "streams" depending on the trigger requirements. The data used for this analysis is taken from the "JetTauEtmiss" stream, which focuses on events which are selected by a jet, tau or transverse missing energy trigger.

3.2.8 Computing Infrastructure

For the storage and analysis of ~25 PByte of data per year the LHC and ATLAS use the so-called Worldwide LHC Computing Grid (WLCG) [32]. This grid is designed as a 4 level computing structure (Tiers) which is distributed over 157 computer centers around the world.

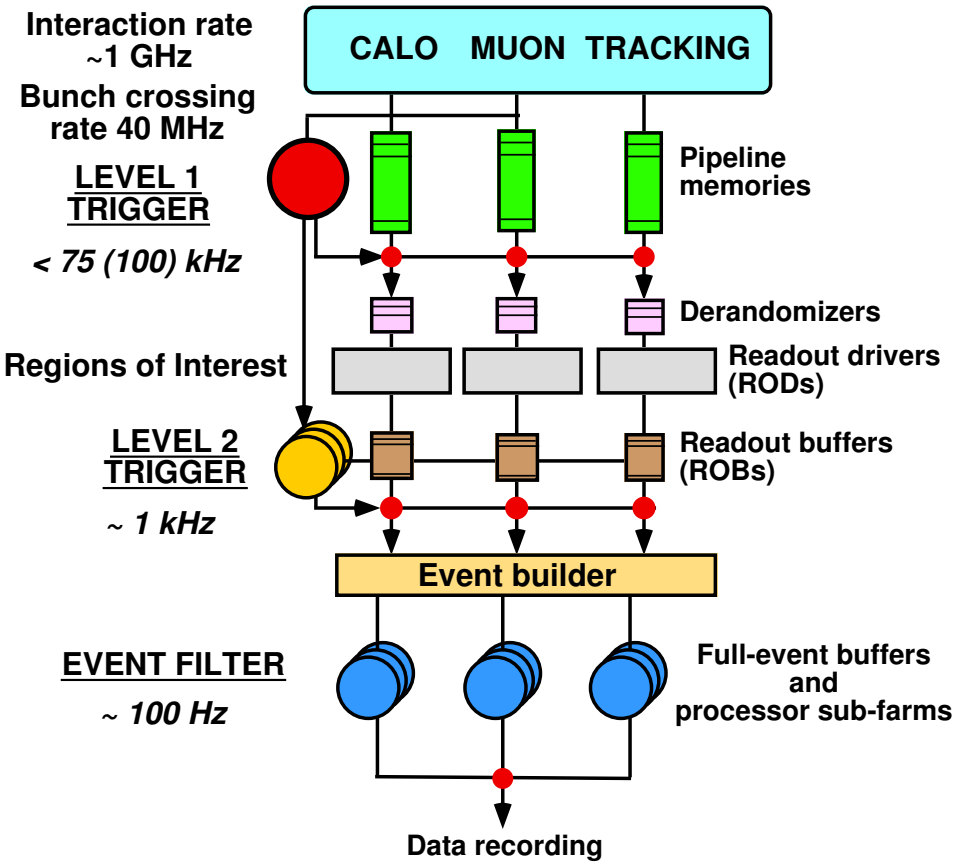

Figure 3.9: Diagram for the trigger system of ATLAS. [25]

- The CERN Computer Center is the **Tier-0** site. All raw data is stored here and a first event reconstruction is processed. The raw data or reconstructed output is then distributed to the Tier-1 sites for further processing. It has about 20% of the total computing capacity.

- There are 13 **Tier-1** sites in various countries mostly in Europe but also in Taiwan, USA, and Korea. These are computing centers with large computing power and storage space. Each center stores a proportional share of the raw and reconstructed data and distributes it further to the Tier-2 sites. Their computing power is used for the reprocessing of data and for Monte Carlo simulation.

- The **Tier-2** sites are smaller computer clusters at around 140 universities and other scientific institutes. They are also used to process the simulation of data events and they provide computing power for the various analysis tasks to perform on the data. They also provide storage for the real and simulated data in certain formats.

- **Tier-3** sites are local computer clusters with access to the grid storage system that are used to perform the user analysis in a smaller scale and with more specialized formats of data.

3.2.9 Software Infrastructure

For ATLAS the software framework ATHENA [33] is used to reconstruct data events measured by the detector. It is also used to generate Monte Carlo (MC) simulations of proton-proton collsions. ATHENA contains various analysis tools and is based on the GAUDI [34] architecture, which is built with Python scripting interfaces to load and configure modules written in C++. The user analysis is then supported by the data analysis software framework ROOT [35] but can also be done in ATHENA.
Monte Carlo simulated events are generated in a 3 step process [36]. First a certain physical process of proton-proton collisions is created with an external generator (e.g. Alpgen, MC@NLO etc.), which are usually not exclusively used for ATLAS. The generator only generates prompt decays of unstable physical particles (e.g. the Z boson) and then stores all particles that would then travel through the detector. In the next step the generated event is fed into a GEANT4 [37] based detector simulation. For each generated particle the interaction with the detector material is simulated. The energy deposited in the material is then stored as a detector "hit" together with the position and the time. For the event generation and the detector interaction also a history is stored as the so-called "truth" information. The "hit"-output is then put into the digitization. In this final step the input into the detector electronics is emulated as well as the level 1 trigger. In this step detector noise or pile-up (overlay by soft collisions in the same bunch crossing) can be included into the event as well. The output of that is in a format similar to raw data and can then be reconstructed with the same software packages. An overview of the various steps that need to be applied to reconstruct an event from Monte Carlo simulation is given in figure 3.10.
There are a variety of data formats stored for ATLAS data and simulation:

- The RAW data is the output directly from the ATLAS triggers and online event reconstruction or the digitization process in a bytestream format with about 1.6 MB/event.

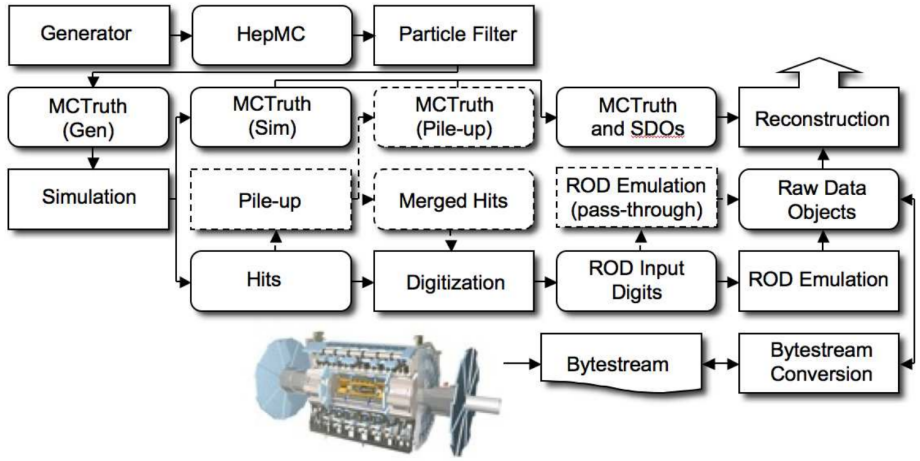

Figure 3.10: The flow of the ATLAS simulation software, from event generators (top left) through reconstruction (top right). [36]

- In the first step of reconstruction a dataset in the Event Summary Data (ESD) format is created. It contains detailed information about tracks and calorimeter hits and provides a combined reconstruction of physical objects. The size is $\sim 0.5 - 1\,\mathrm{MB/event}$. RAW and ESD data formats are not used for user analysis.
- From ESD the Analysis Object Data (AOD) format can be created. This is a summary of event reconstruction information and contains physical objects like electrons and jets. This is already sufficient for common analyses but the size is still rather large with 100-200 KB/event.
- In the Derived Physics Data (DPD) formats physics groups can include information specialized for certain analyses or they can omit information and even complete events to reduce the event size for optimized processing of the files. A typical aim for the event size is 10 KB/event.

4 Description of the Search for SUSY in Events With at Least Two Hadronic Taus

This chapter introduces the analysis for the search of R-parity conserving SUSY events with at least two hadronic taus in the final state.

4.1 Motivation

Electroweak production processes for SUSY particles are promising candidates for the discovery of Supersymmetry with R-parity conservation at hadron-hadron colliders. Normally squark and gluino production processes would dominate. In SUSY models like the pMSSM, which is used as the underlying SUSY model in this thesis, the sleptons and / or gauginos are assumed to have the lightest masses in the parameter space. If the gluino

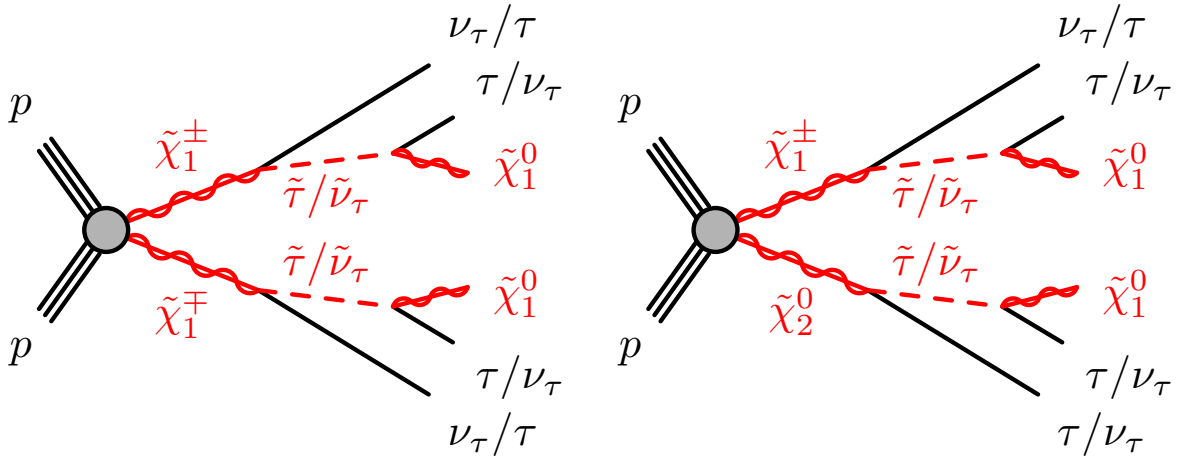

Figure 4.1: Feynman diagram for $\tilde{\chi}_1^{\pm}\tilde{\chi}_1^{\mp}$ production (left) and for $\tilde{\chi}_2^0\tilde{\chi}_1^{\pm}$ production (right), which then decay via an intermediate left-handed stau or stau neutrino.

and squark masses are very heavy, the strong processes are not dominating over the weak processes, because their cross-sections decrease with increasing mass (see figure 2.7). Their production might not be possible at all at the LHC. First searches with the ATLAS detector for strong production processes described by the MSUGRA model

excluded wide mass ranges for the gluino up to 1.1 - 1.8 TeV depending on the event topology (an overview of the results can be seen in figure 2.3).
The processes with the highest probability are the pair production of charginos and neutralinos $\tilde{\chi}_1^{\pm}\tilde{\chi}_1^{\mp}$, $\tilde{\chi}_2^0\tilde{\chi}_1^{\pm}$ and the pair production of the lightest slepton. For the pMSSM model used in this thesis the stau is chosen to be the lightest slepton. In the ATLAS collaboration the different SUSY analyses are subdivided depending on the objects present in the final state. In the analysis presented in this thesis events with two or more hadronically decaying taus and no light additional leptons are investigated. This is based on the analysis in [38] and is complementary to the analysis with two light leptons in the final state [39] and to the analysis with at least three leptons [40].
An event topology with two or more taus can be obtained from chargino decays into left-handed $\tilde{\tau}\nu_\tau$ or $\tilde{\nu_\tau}\tau$, or next to lightest neutralino decays into $\tilde{\tau}\tau$. Feynman diagrams for gaugino pair production are shown in figure 4.1. The $\tilde{\chi}_2^0\tilde{\chi}_1^{\pm}$ might also yield a two tau final state if one tau is not reconstructed. The possible Feynman diagram for a direct stau decay process is shown in figure 4.2. The analysis presented in this thesis is not sensitive to the direct stau production due to the low cross-section.

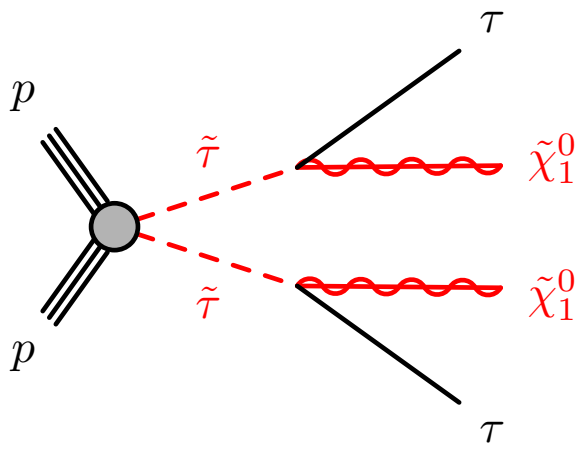

Figure 4.2: Feynman diagram for the pair production of staus, which then further decay into the LSP and a tau lepton each.

Since the lightest neutralinos leave the detector without interacting with its material, it is expected that these SUSY events have a large missing transverse energy (defined in section 4.3.5).
The main Standard Model background contribution comes from QCD multi-jet and W + jets production. In the former process both taus are a mis-reconstructed jet (see section 4.3.2) and in the latter case the W decays into a real τ and the other tau is a mis-reconstructed jet. A jet that is mis-reconstructed as a tau is called a fake tau. The fake-tau contribution to the Standard Model background is estimated with a data driven method, shown in section 5.1. Other background contributions from diboson, top, and $Z/\gamma*$ + jets are estimated with Monte Carlo simulations.

4.2 Datasets

4.2.1 Data

The data analyzed in this thesis was taken with the ATLAS detector in the 2012 proton-proton collision run at $\sqrt{s} = 8\,\text{TeV}$. The total recorded data of that year corresponds to an integrated luminosity of $\int \mathcal{L}\,\mathrm{dt} \approx 21.7\,\text{fb}^{-1}$ [31]. An overview of the data taking throughout the year 2012 can be seen in figure 4.3.

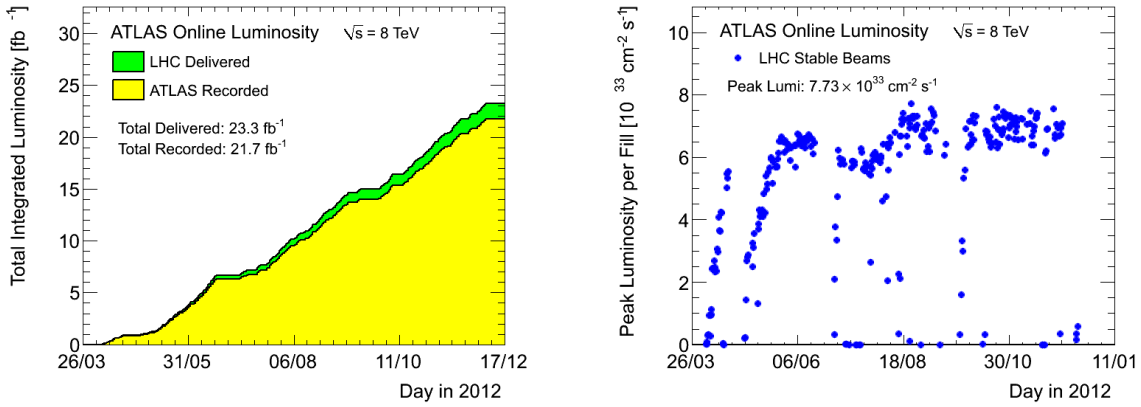

(a) (b)

Figure 4.3: Cumulative delivered and recorded luminosity versus day by ATLAS (4.3a) and maximum instantaneous luminosity versus day recorded by ATLAS (4.3b). [31]

To be useful for a physics analysis all detector components need to work acceptably during the measurement. The data taking periods that fulfill the data quality requirements are listed in a so-called "Good Run List" (GRL). The GRL used for this analysis reduces the available integrated luminosity to $\int \mathcal{L}\,\mathrm{dt} = 20.3398\,\text{fb}^{-1}$.

4.2.2 SUSY Signal

pMSSM grid

For the generation of the SUSY signal grid of Monte Carlo samples the ISASUSY 7.80 generator [41] is used. This signal grid is generated according to the pMSSM model (see section 2.3.2) with the following properties:

- $\tan\beta = 50$ (large);
- $M_1 = 50\,\text{GeV}$ (small);
- M_2 and μ are varied between 100 and 500 GeV;
- lightest stau mass fixed at 95 GeV (LEP limit);

- other sleptons, squarks, and gluinos are set to very high masses (3 TeV).

With all other masses set to high values the only available processes are the direct production of two staus or the pair production of charginos and neutralinos. The dominating processes with 2-3 taus in the final state are:

- $\tilde{\tau}^+\tilde{\tau}^- \rightarrow \tau^+\tilde{\chi}_1^0\tau^-\tilde{\chi}_1^0$
- $\tilde{\chi}_1^\pm\tilde{\chi}_1^\mp \rightarrow \tau^\pm\nu\tilde{\chi}_1^0\tau^\mp\nu\tilde{\chi}_1^0$
- $\tilde{\chi}_1^\pm\tilde{\chi}_2^0 \rightarrow \tau^\pm\nu\tilde{\chi}_1^0\tau\tau(\nu\nu)\tilde{\chi}_1^0$

Simplified Models
A second set of signal grids is generated according to the Simplified Models. Two production modes are considered:

- C_1N_2 production: $\tilde{\chi}_1^\pm\tilde{\chi}_2^0$
- C_1C_1 production: $\tilde{\chi}_1^\pm\tilde{\chi}_1^\mp$

To reproduce the decay processes shown in figure 4.1 all particle masses except for $\tilde{\chi}_2^0$, $\tilde{\chi}_1^0$, $\tilde{\chi}_1^\pm$, $\tilde{\nu_\tau}$, and $\tilde{\tau}$ are set to extremely high values $O(100\,\text{TeV})$. The stau and the stau neutrino are assumed to have the same mass and the mass of $\tilde{\chi}_2^0$ and $\tilde{\chi}_1^\pm$ is assumed to be degenerate as well.
For the Monte Carlo grids the lightest chargino and the lightest neutralino mass are varied. In the C_1N_2 production the $\tilde{\chi}_1^\pm$ mass is varied from 100 to 500 GeV and the $\tilde{\chi}_1^0$ mass from 0 to 357.5 GeV. For the C_1C_1 production the $\tilde{\chi}_1^\pm$ mass range is between 0 and 400 GeV and the $\tilde{\chi}_1^0$ mass is set to values between 0 and 182.5 GeV.
Throughout this thesis two reference points "SUSY Ref. P1" and "SUSY Ref. P2" are used as benchmarks, one for each production mode:

- SUSY Ref. P1: C_1N_2 production, $C_1 = 250\,\text{GeV}$, $N_1 = 100\,\text{GeV}$ (Process ID: 176802)
- SUSY Ref. P2: C_1C_1 production, $C_1 = 250\,\text{GeV}$, $N_1 = 50\,\text{GeV}$ (Process ID: 176873)

4.2.3 Standard Model Monte Carlo

For the simulation of the most important Standard Model processes Monte Carlo simulated samples are used aside of data driven techniques. The W + jets and Z + jets samples are produced with the Sherpa [42] generator. The diboson samples make use of the Sherpa and MC@Nlo [43] generators. For the single top samples the MC@Nlo and AcerMC [44] generators have been used. The generators for the $t\bar{t}$ samples are Sherpa and MadGraph [45]. In table 4.1 all Standard Model samples used in this thesis are listed in detail with their properties.

W + jets						
Process	Process ID	Generator	σ [pb]	k-factor	ϵ_{Filter}	N_{MC}
$W \to e\nu$	147774	Sherpa	11878	1.0259	1.0	31348848
$W \to \mu\nu$	147775	Sherpa	11879	1.0258	1.0	36426652
$W \to \tau\nu$	147776	Sherpa	11872	1.0264	1.0	6998385
Z + jets and Drell-Yan						
Process	Process ID	Generator	σ [pb]	k-factor	ϵ_{Filter}	N_{MC}
$Z \to ee$	147770	Sherpa	1207.9	1.0276	1.0	4999887
$Z \to \mu\mu$	147771	Sherpa	1207.9	1.0276	1.0	9998983
$Z \to \tau\tau$	147772	Sherpa	1207.1	1.0282	1.0	4999989
$Z \to \nu\nu$	147773	Sherpa	6521.4	1.028	1.0	2659998
$Z \to \tau\tau(m_{ll}(8,15))$	173045	Sherpa	92.116	1.0	1.0	4999693
$Z \to \tau\tau(m_{ll}(15,40))$	173046	Sherpa	279.11	1.0	1.0	14992666
Diboson						
Process	Process ID	Generator	σ [pb]	k-factor	ϵ_{Filter}	N_{MC}
$WW \to ll\nu\nu$	126892	Sherpa	5.4982	1.06	1.0	2699994
$WZ \to lll\nu$	126893	Sherpa	9.7534	1.05	1.0	2699893
$ZZ \to llll$	126894	Sherpa	8.7356	1.0	1.0	3799491
$ZZ \to ll\nu\nu$	126895	Sherpa	0.4962	1.05	1.0	899899
$WW \to ll\nu\nu$ SS	126988	Sherpa	0.0181	1.0	1.0	49900
$WW \to ll\nu\nu jj$ SS	126989	Sherpa	0.0208	1.0	1.0	100000
$ggWW \to e^+\nu e^-\nu$	106011	MC@Nlo	0.01747	1.196	1.0	30000
$ggWW \to e^+\nu\mu^-\nu$	106012	MC@Nlo	0.01747	1.196	1.0	29900
$ggWW \to e^+\nu\tau^-\nu$	106013	MC@Nlo	0.01747	1.196	1.0	30000
$ggWW \to \mu^+\nu\mu^-\nu$	106014	MC@Nlo	0.01747	1.196	1.0	30000
$ggWW \to \mu^+\nu e^-\nu$	106015	MC@Nlo	0.01747	1.196	1.0	30000
$ggWW \to \mu^+\nu\tau^-\nu$	106016	MC@Nlo	0.01747	1.196	1.0	30000
$ggWW \to \tau^+\nu\tau^-\nu$	106017	MC@Nlo	0.01747	1.196	1.0	30000
$ggWW \to \tau^+\nu e^-\nu$	106018	MC@Nlo	0.01747	1.196	1.0	30000
$ggWW \to \tau^+\nu\mu^-\nu$	106019	MC@Nlo	0.01747	1.196	1.0	30000
$ggZZ \to 4lep$	116600	MC@Nlo	0.00279	1.0	0.56875	40000
$ggZZ \to 4e$	116601	MC@Nlo	0.001535	1.0	1.0	90000
$ggZZ \to 4\mu$	116602	MC@Nlo	0.001535	1.0	1.0	90000
$ggZZ \to 2e2\mu$	116603	MC@Nlo	0.001535	1.0	1.0	90000
$VV \to eeqq$	157814	Sherpa	1.702	1.0	1.0	200000
$VV \to \mu\mu qq$	157815	Sherpa	1.687	1.0	1.0	200000
$VV \to \tau\tau qq$	157816	Sherpa	1.702	1.0	1.0	199999
$VV \to e\nu qq$	157817	Sherpa	9.557	1.0	1.0	889996
$VV \to \mu\nu qq$	157818	Sherpa	9.554	1.0	1.0	999996
$VV \to \tau\nu qq$	157819	Sherpa	9.557	1.0	1.0	999899
Single top						
Process	Process ID	Generator	σ [pb]	k-factor	ϵ_{Filter}	N_{MC}
$t(\mathrm{s-channel})e\nu$	108343	Mc@Nlo	0.56444	1.074	1.0	199997
$t(\mathrm{s-channel})\mu\nu$	108344	Mc@Nlo	0.56426	1.074	1.0	200000

$t(\mathrm{s}-\mathrm{channel})\tau\nu$	108345	Mc@Nlo	0.56404	1.074	1.0	199999
tW	108346	Mc@Nlo	20.658	1.083	1.0	1999194
$t(\mathrm{t}-\mathrm{channel})e$	117360	AcerMC	8.604	1.1	1.0	299899
$t(\mathrm{t}-\mathrm{channel})\mu$	117361	AcerMC	8.604	1.1	1.0	300000
$t(\mathrm{t}-\mathrm{channel})\tau$	117362	AcerMC	8.604	1.1	1.0	293499
$\mathrm{t\bar{t}}$						
Process	Process ID	Generator	σ [pb]	k-factor	ϵ_{Filter}	N_{MC}
$t\bar{t} \to ll$	117800	Sherpa	9.1616	1.212	1.0	1799288
$t\bar{t} \to l\tau_l$	117801	Sherpa	9.1724	1.211	0.352	599698
$t\bar{t} \to \tau_l\tau_l$	117802	Sherpa	2.2595	1.229	0.123904	55000
$t\bar{t} \to ljj$	117803	Sherpa	55.53	1.246	1.0	8750233
$t\bar{t} \to l\tau_h$	117804	Sherpa	9.2582	1.199	0.648	1099994
$t\bar{t} \to \tau_l jj$	117805	Sherpa	27.766	1.252	0.352	1797891
$t\bar{t} \to \tau_l\tau_h$	117806	Sherpa	2.3107	1.201	0.456192	200000
$t\bar{t} \to jjjj$	117807	Sherpa	83.578	1.302	1.0	5498350
$t\bar{t} \to jj\tau_h$	117808	Sherpa	27.788	1.251	0.648	3199884
$t\bar{t} \to \tau_h\tau_h$	117809	Sherpa	2.3031	1.205	0.419904	179900
$t\bar{t}W$	119353	MadGraph	0.1041	1.175	1.0	399997
$t\bar{t}Wj$	119354	MadGraph	0.093317	1.175	1.0	399896
$t\bar{t}Z$	119355	MadGraph	0.06769	1.34	1.0	399996
$t\bar{t}Zj$	119356	MadGraph	0.087339	1.34	1.0	399895

Table 4.1: List of all Standard Model Monte Carlo samples used in this analysis with their generator, cross-section σ, k-factor (necessary to scale the cross-section from leading order Feynman diagrams to next-to-leading order or beyond), filter efficiency ϵ_{Filter}, and number of events in the sample N_{MC}.

4.3 Object Definition

In order to perform a physics analysis with a detector in a collider experiment the measured currents, times, and hits in all of the detector components need to be reconstructed into physical objects. The reconstruction is limited by the resolution and the spatial coverage of the detector components. The reconstruction algorithms need to be optimized for the conditions of a data taking period and the reach of a certain analysis. In this section the definitions of the reconstructed particle properties and other necessary physical variables needed for this analysis are given.

4.3.1 Jets

Particle bundles that propagate into almost the same direction are called jets. These bundles are identified as only one object, because they can originate from only one quark produced in the hard proton proton scattering, which generates a multitude of hadrons via the hadronization process of the strong interaction. Also electrons and photons

produce a particle bundle while interacting with the detector, but an electromagnetic shower has a much shorter decay length than a hadronic jet and can be differentiated. Hadronically decaying taus are also identified as jets with special properties. Their identification is discussed in the next subsection.
A jet is identified using the energy deposits in the calorimeters. Depending on the reconstruction algorithm this might just be a cone around the highest energy deposits or a more sophisticated sequential recombination of the calorimeter clusters. For this analysis jets are reconstructed using the collinear and infrared safe anti-k_t algorithm [46] with a distance parameter $R = 0.4$. The energy measured with the calorimeters needs to be calibrated with algorithms derived from simulated jets. For the anti-k_t jets the Local Hadronic Calibration (LC) is used [47].
The basic cuts on those jets are:

- Transverse momentum $p_T > 20\,\text{GeV}$
- Pseudorapidity $|\eta| < 2.5$
- Additionally jets have to pass a set of quality criteria which exclude jet reconstructions that are not associated to real energy deposits in the calorimeters. These misidentified jets could arise from hardware problems, LHC beam conditions, or cosmic-ray showers. The "Looser" threshold is used, which is defined by the ATLAS JetETMiss group.
- Overlap Removal (see section 4.3.8)

This set of cuts defines the baseline jet definition. For the signal and control regions further cuts are applied and the jets are distinguished into three categories. These jets are then called signal jets.
A useful variable to identify jets coming from a hard scattering vertex is the jet-vertex fraction (JVF) [48]. It is calculated with an algorithm which associates tracks of charged particles and their associated primary vertex with calorimeter jets. Additionally a tagging weight for b flavor jets is determined with the MV1 algorithm, which is based on a neural network [49]. A value greater than 0.122 for the MV1 weight corresponds to an 85% efficiency. For the jet-vertex fraction and the b-tagging information from the inner detector is needed. This limits the η range to 2.5. The following three signal jet categories are defined for jets that pass the baseline cuts:

- **Central Light Jets:** $p_T > 25\,\text{GeV}$, $|\eta| < 2.5$, $JVF > 0.2$, and $MV1 \leq 0.122$. These cuts mean that these jets are not coming from a b quark decay and they are associated to the hard scattering.
- **B-Jets:** $p_T > 20\,\text{GeV}$, $|\eta| < 2.5$, and $MV1 > 0.122$ (no JVF cut). These are the jets that are supposed to originate from a b quark decay.
- **Forward Jets:** $p_T > 30\,\text{GeV}$ and $2.5 < |\eta| < 4.5$. These are the jets that are detected outside of the tracking system coverage at angles closer to the beam axis.

4.3.2 Taus

Tau leptons are the most important objects for this particular SUSY search. Taus have a mass of 1.777 GeV and a mean life time of $\tau = 291 \times 10^{-15}$ s, which corresponds to $c\tau = 87\,\mu$m. A tau does not interact with detector material before decaying, because the first layer of the inner detector is at a 5 cm distance from the interaction point. Therefore the tau needs to be reconstructed indirectly. The reconstruction depends on the decay mode of the tau. The main decay modes are listed in table 4.2. The leptonic decays,

Decay Mode	Branching Ratio
Leptonic Modes (τ_l)	
$\tau^\pm \to e^\pm \nu_e \nu_\tau$	17.8%
$\tau^\pm \to \mu^\pm \nu_\mu \nu_\tau$	17.4%
Hadronic Modes (τ_h)	
1 Prong	
$\tau^\pm \to \pi^\pm \nu_\tau$	10.8%
$\tau^\pm \to \pi^\pm \pi^0 \nu_\tau$	25.5%
$\tau^\pm \to \pi^\pm \pi^0 \pi^0 \nu_\tau$	9.3%
3 Prongs	
$\tau^\pm \to \pi^\pm \pi^\pm \pi^\mp \nu_\tau$	9.3%
$\tau^\pm \to \pi^\pm \pi^\pm \pi^\mp \pi^0 \nu_\tau$	4.6%

Table 4.2: Overview of the most common τ decay modes. [6]

where an electron or muon is produced together with neutrinos, are not considered in this analysis, because leptonically decaying taus are very difficult to distinguish from directly produced lighter leptons. Moreover these events are considered in SUSY searches that focus on light leptons in the final state [39].
The hadronic decays, where the tau decays into a certain number of hadrons and a neutrino, are further subdivided into modes with one or three charged particles in the decay (the modes are called 1 prong or 3 prong). This distinctive property can be used to differentiate between taus and jets from quarks and gluons. Nevertheless also the hadronically decaying taus are difficult to reconstruct, because quark or gluon decays that produce a jet of hadrons look very similar. It is also possible for an electron or muon to be mis-reconstructed as a 1 prong tau decay.
To reconstruct taus [50] all anti-k_T jets with $p_T > 10\,\text{GeV}$, $|\eta| < 2.5$, and distance parameter $R = 0.4$ are used as a tau candidate. Various information from the tracking devices and the calorimeters are used to distinguish between taus and other particles. Aside of the number of charged particles in the jet there are some additional differences between QCD jets and tau jets. Taus are expected to have a secondary vertex and a rather narrow cone, because of the low number of hadrons. The identification method for the taus used in this thesis is based on boosted decision trees (BDT). The output

variables of the BDTs provide a scale for various efficiencies of background suppression and signal identification.
For the BDT based jet discrimination the trees are trained with taus from simulated $Z \to \tau\tau$ events for the signal and simulated QCD multi-jet events for the background. The "loose", "medium", and "tight" thresholds have been defined and correspond to 60%, 50%, and 30% signal efficiency for 1-prong candidates and 65%, 55%, and 35% signal efficiency for 3-prong candidates.
To differentiate between electrons and 1 prong taus the BDTs have been trained with simulated $Z \to ee$ events for the background. An electron veto is defined for three working points also called "loose", "medium", and "tight", which correspond to 95%, 85%, and 75% signal efficiency for 1-prong decay modes. The electron veto is only used for tau candidates with one charged track, because electrons are unlikely to produce more than one charged track and the BDT based discrimination does not need to be applied to 3-prong candidates.
Muons are rather unlikely to be misidentified as hadronically decaying taus, because they do not deposit large amounts of energy in the calorimeters. Hence only a cut based muon veto is used for the exclusion of those. The muon veto is defined at a signal efficiency of 96%. With the veto approximately 55% of muons misidentified as taus are rejected.
Together with the BDT based tau identification algorithms the following cuts are used on the tau candidates to define the baseline taus for this analysis:

- Transverse momentum $p_T > 20\,\text{GeV}$;
- Pseudorapidity $|\eta| < 2.5$;
- Number of tracks (prongs) = 1 or 3;
- Electric charge $|q| = 1$;
- Muon Veto (defined above);
- "Loose" Electron BDT Veto, only applied to 1 prong taus;
- "Medium" threshold for the Jet BDT score;
- Overlap Removal (see section 4.3.8).

To further improve the requirements on taus in this analysis the quality of the jet discrimination is adjusted at certain points. For the signal regions at least one tau is required to pass the "tight" threshold. For the background studies also different working points are applied, which are outlined in the corresponding section.

4.3.3 Muons

A muon passes the entire ATLAS detector as long as its energy is high enough, because the muon mean life time is $\tau = 2.2 \times 10^{-6}\,\text{s}$, which is much longer than for the tau lepton. Also the muon mass is sufficiently high to not lose their entire energy via bremsstrahlung

during their trajectory. Thus a muon is supposed to be detected with one track reconstructed in the inner detector and one in the muon spectrometer. The energy deposits in the calorimeters are expected to be very small for a muon.
For the reconstruction of muons the STACO (STAtistical COmbination) algorithm is used [51][52]. In this algorithm the tracks of the inner detector and the muon spectrometer are statistically combined. The following cuts are applied to muon candidates:

- Transverse momentum $p_T > 10\,\text{GeV}$;
- Pseudorapidity $|\eta| < 2.4$;
- The muon needs to be reconstructed from a combination of an inner detector track and muons spectrometer track or it needs to be at least an inner detector track which is matched to a segment of the most inner layer of the muon spectrometer.
- "Loose" STACO quality criteria;
- Additional quality cuts on the track reconstruction in the SCT, TRT, and pixel detector;
- Overlap Removal (see section 4.3.8).

4.3.4 Electrons

The electron loses its energy via bremsstrahlung much faster than heavier leptons or hadrons while passing the detector material. Hence electrons deposit their entire energy in the electromagnetic calorimeter and do not reach the hadronic calorimeter. The electrons are reconstructed with the egamma algorithm [53]. In this algorithm quality criteria are applied to reconstruct an electron from energy deposits in the electromagnetic calorimeter. For higher electron identification efficiency also tracking information and matching between inner detector and calorimeter information is used.
The electrons are then identified as:

- Transverse momentum $p_T > 10\,\text{GeV}$;
- Pseudorapidity determined from clusters $|\eta_{cl}| < 2.47$;
- "Medium++" quality criteria and additional "object quality" cuts;
- Electron "author" 1 or 3; this excludes candidates that are not from cluster seeded electrons or other possible objects that the egamma algorithm reconstructs (e.g. photons).
- Overlap Removal (see section 4.3.8).

4.3.5 Missing Transverse Energy

A very useful variable that provides a scale for undetected particles is the missing transverse energy E_T^{miss}. Since the protons that collide have no momentum perpendicular to the beam axis, momentum conservation predicts that also the vectorial sum of all decay products of the collision should add up to zero in the transverse plane. For R-parity conserving SUSY searches the LSP escapes the detector without interacting with the material and thus leading to missing energy. From the Standard Model also the neutrinos do not interact with the ATLAS detector and yield missing energy. In this analysis final states with tau leptons are analyzed. Since taus decay into at least one neutrino, also Standard Model processes with taus in the final state are expected to have a certain amount of missing energy.
To calculate E_T^{miss} the transverse vector components of the energy deposits in the calorimeters of all jets, electrons, photons, muons, and the clusters that are not able to be associated to a physical object are negatively added up. This can be written as

$$E_{x(y)}^{miss} = -\sum_i E_{x(y),i}, \tag{4.1}$$

where i is an index for all reconstructed objects and also the energy not assigned to any of those object. Thus not only the particles from the hard scattering are considered but also particles from pile-up are taken into account. The missing transverse energy is then calculated as

$$E_T^{miss} = \sqrt{(E_x^{miss})^2 + (E_y^{miss})^2}. \tag{4.2}$$

4.3.6 Transverse Mass

Another variable used throughout this analysis is the transverse mass. It is invariant under Lorentz boosts along the z-axis. The transverse component of the mass of a particle, which decays into two particles, can be reconstructed from the kinematic properties of the decay products as follows

$$m_T^2 = (E_{T,1} + E_{T,2})^2 - (\vec{p}_{T,1} + \vec{p}_{T,2})^2. \tag{4.3}$$

With the energy of the two decay products $E_{T,i}^2 = m_i^2 + \vec{p}_{T,i}^2$ inserted into the equation, the mass can be written as

$$m_T^2 = m_1^2 + m_2^2 + 2(E_{T,1}E_{T,2} - \vec{p}_{T,1}\vec{p}_{T,2}). \tag{4.4}$$

If one of the decay particles is invisible like for a $W \to e\nu$ decay, the kinematic properties can only be described with $\vec{E}_T^{miss}$. With the assumption that the visible and invisible particle have negligible masses compared to their momentum, the equation can be simplified to

$$m_T^2 = 2|\vec{E}_T^{miss}||\vec{p}_{T,vis}|(1 - cos\phi), \tag{4.5}$$

where ϕ is the angle between E_T^{miss} and the visible particle. This variable is useful to distinguish processes where the missing energy is coming from the neutrino in a $W \to l\nu$ decay. For instance in section 7.3 the top background can be discriminated from the Z + jets background with the sum of two transverse masses.

4.3.7 Stransverse Mass

For the reconstruction of a particle pair where each particle decays into one visible and one invisible pair the "stransverse mass" is introduced [54][55]. The transverse mass alone is not enough to describe such a kinematic system. The stransverse mass is defined as the bigger one of the two transverse masses of the particle pair. If the two invisible particles could be reconstructed individually the calculation was straight forward from the transverse mass definition. But only their vectorial sum can be reconstructed as the missing transverse energy. With the minimization of arbitrary variables $\vec{q}_1$ and $\vec{q}_2$, which fulfill $\vec{E}_T^{miss} = \vec{q}_1 + \vec{q}_2$, the stransverse mass is defined as:

$$m_{T2}^2 = \min_{\vec{q}_1+\vec{q}_2=\vec{E}_T^{miss}} \left[\max \left\{ m_T^2(\vec{p}_{T,1}, \vec{q}_1) \ , \ m_T^2(\vec{p}_{T,2}, \vec{q}_2) \right\} \right]. \tag{4.6}$$

The ideal decay process described by the stransverse mass is the direct slepton decay, shown in figure 4.2. The direct gaugino processes, which are also the focus of this thesis, are influenced by the additional neutrinos in the process, which contribute to the E_T^{miss} vector, but the variable is still useful to identify these processes as well. Such SUSY processes are expected to have a high stransverse mass. Without any additional cuts the only irreducible Standard Model backgrounds to a cut on m_{T2} would be $W^+W^- \to l^+l^-\nu\nu$ and $t\bar{t} \to b\bar{b}W^+W^- \to jjl^+l^-\nu\nu$. The $t\bar{t}$ contribution can be suppressed with a jet veto cut and the diboson process should peak around the W mass. Therefore m_{T2} is very useful to discriminate between SUSY events and Standard Model background.

4.3.8 Overlap Removal

The overlap removal describes an object definition step, where reconstructed physical objects close to other objects are excluded for various reasons.
One reason is that a physical object can be reconstructed more than once by the various reconstruction algorithms for jets and leptons. These double counted objects need to be excluded. Electrons and hadronically decaying taus are always reconstructed as a jet as well. These double counted jets need to be discarded. As described in the tau definition (section 4.3.2), a muon or electron might be mis-reconstructed as a tau. In addition to the applied electron and muon veto in the tau object definition taus are discarded if a reconstructed electron or muon is found in close vicinity to the tau. If two muons are found extremely close to each other, one muon might be falsely reconstructed as two. Since those particles have a larger uncertainty on their direction and energy reconstruction they are completely cut out of the event.
Another reason to exclude reconstructed objects that are close to others are physical processes that occur after the hard scattering process. Light leptons that are produced

in a semi-leptonic decay of a b or c quark inside a jet are considered to be part of the jet and the reconstructed lepton object is rejected. It is also possible that an electron is reconstructed as more than one particle, if it emits bremsstrahlung in a way that the radiation is identified as another object. Therefore electrons reconstructed very close to each other are considered to be one particle. Another possibility are muons, which emit enough bremsstrahlung in the calorimeter to be also reconstructed as an electron. In this case both particles are discarded.
The overlap removal in this analysis also includes the rejection of lepton pair resonances with a low invariant mass coming from meson decays.
In the following each rejection is outlined. They are consecutively applied step by step on the identified objects that are still present after the step before:

1. $\Delta R(e_1, e_2) \leq 0.1$: If the distance between two electrons e_1, e_2 is $\Delta R \leq 0.1$, then the electron with the lower energy is rejected. This rejects electrons falsely reconstructed from the bremsstrahlung of a correctly reconstructed electron.

2. $\Delta R(j, e) \leq 0.2$: If a jet is closer than $\Delta R \leq 0.2$ to an electron, the jet is rejected. This rejection is due to the double reconstruction of an electron also as a jet.

3. $\Delta R(e, j) \leq 0.4$: If an electron is in the broader range $\Delta R \leq 0.4$ of the remaining jets after the second step, the electron is discarded. This rejects electrons that are produced in a semi-leptonic decay inside a jet. These electrons are considered to be part of the jet.

4. $\Delta R(\mu, j) \leq 0.4$: Muons that are in the range $\Delta R \leq 0.4$ of a jet are rejected. This rejects muons that are produced in a semi-leptonic decay inside a jet. These muons are considered to be part of the jet.

5. $\Delta R(\mu, e) \leq 0.1$: If an electron and muon are closer than $\Delta R \leq 0.1$, both particles are rejected. This cut rejects muons emitting enough bremsstrahlung in the calorimeters to be also identified as electrons and also the corresponding electron object.

6. $\Delta R(\mu_1, \mu_2) \leq 0.05$: In the case that a muon pair is in the range $\Delta R \leq 0.05$, both muons are excluded. This cut rejects muons that are falsely reconstructed as two.

7. $m_{ll}(\mu^{\pm}, \mu^{\mp}) \leq 12\,\text{GeV}$: If the invariant mass of a muon pair with opposite charges is less than 12 GeV, then both muons are discarded. This cut rejects lepton pair resonances with a low invariant mass coming from meson decays.

8. $m_{ll}(e^{\pm}, e^{\mp}) \leq 12\,\text{GeV}$: If the dilepton mass of two oppositely charged electrons is less than 12 GeV, then both electrons are discarded. This cut rejects lepton pair resonances with a low invariant mass coming from meson decays.

9. $\Delta R(\tau, e) \leq 0.2$: If a τ is closer than $\Delta R \leq 0.2$ to an electron, the tau is rejected. Electrons might also be mis-reconstructed as taus. Thus the double counted object is rejected.

10. $\Delta R(\tau, \mu) \leq 0.2$: If a τ is in the range $\Delta R \leq 0.2$ of a muon, the tau is excluded. Muons might also be mis-reconstructed as taus. Thus the double counted object is rejected.

11. $\Delta R(j, \tau) \leq 0.2$: Jets that are as close as $\Delta R \leq 0.2$ to a tau are discarded. This rejection is due to the double reconstruction of a hadronically decaying tau also as a jet.

12. $m_{ll}(\tau^{\pm}, \tau^{\mp}) \leq 12\,\text{GeV}$: If a tau pair has an invariant mass of less than 12 GeV, then both taus are excluded. This cut rejects lepton pair resonances with a low invariant mass coming from meson decays.

4.4 Trigger

For this analysis a combination of a ditau and an E_T^{miss} trigger is used. At least one of the triggers is required to have fired, which corresponds to a logical OR. For the taus and the E_T^{miss} that are reconstructed for the analysis the thresholds are higher than the cuts on the trigger objects, because the trigger is only reliable when it reaches the efficiency plateau. The trigger description with requirements on the trigger object and the corresponding offline cuts on the reconstructed objects is shown in table 4.3.

Trigger	online thresholds	offline thresholds
ditau	$p_T(\tau_1) > 29\,\text{GeV}$, $p_T(\tau_2) > 20\,\text{GeV}$	$p_T(\tau_1) > 40\,\text{GeV}$, $p_T(\tau_2) > 25\,\text{GeV}$
E_T^{miss}	$E_T^{miss} > 80\,\text{GeV}$	$E_T^{miss} > 150\,\text{GeV}$

Table 4.3: List of triggers.

4.5 MC Event Weights

The Monte Carlo generated events need to be weighted to simulate a physical process. For some generators like the Sherpa generator the generated events need to be weighted with an additional "MC event weight" to simulate physically meaningful distributions. This is a weight that is stored with each MC event and it should always be applied for ATLAS analyses. The next step is to simulate the Standard Model processes with the actual data-taking conditions with additional weights. The following weights are used in this analysis:

- **Pile-up weight:** Pile-up is the collection of several effects. During the bunch crossing soft interactions occur with the highest probability. In a soft interaction only a small amount of momentum is transferred. Tracks and energy deposits add to the hard scattering event. These effects are called in-time pile-up. Additionally to this in-time pile-up effects the time some detector components need to read

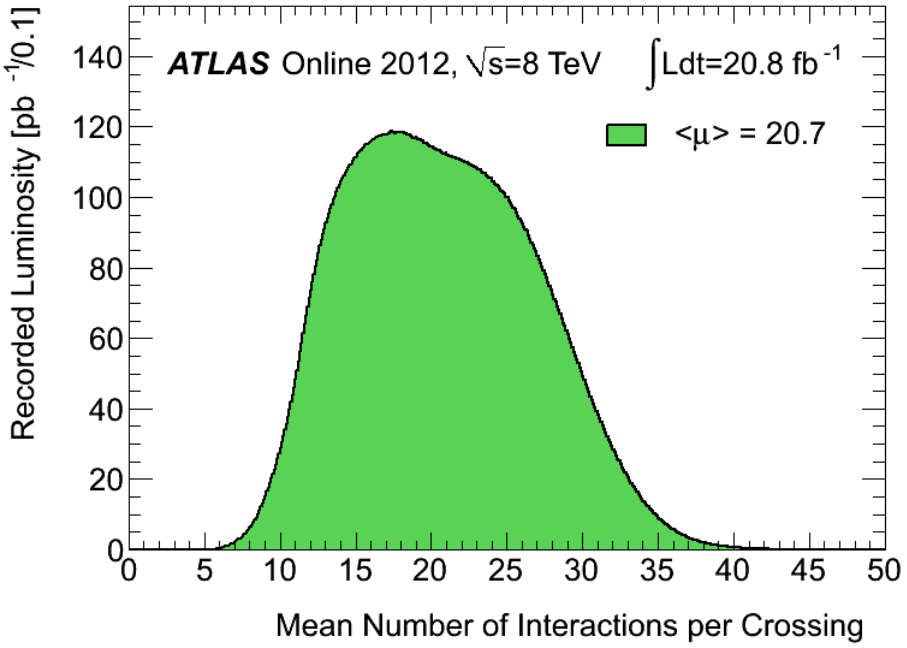

Figure 4.4: Luminosity-weighted distribution of the mean number of interactions per crossing for 2012 taken up to November 26th. [31]

out measurements have influence on the event reconstruction as well. Especially the calorimeters need several bunch crossings to read out and reset their cells. Thus particle identifications from previous events can also overlay an event. This is called out-of-time pile-up. The pile-up varies as a function of the number of interactions per bunch crossing $< \mu >$. The Monte Carlo samples are generated with a certain $< \mu >$ distribution. However this distribution needs to be reweighted to the conditions during the data-taking. The distribution of the mean number of interactions for the data used for this analysis is shown in figure 4.4.

- **Tau Identification and Trigger Scale Factors:** The most important object in this analysis are the taus. Therefore differences in the identification process between data and MC need to be corrected. A multiplicative scale factor for the event weight is determined for every tau. It depends on the tau classification, the trigger and whether the reconstructed tau can be matched within $\Delta R < 0.2$ to the simulated object. Taus that cannot be matched to a simulated object, like jets that are misidentified as a tau, are weighted in a different way than real taus, where the reconstructed object can be associated to a simulated tau.

- **B-tagging weight:** When selecting or vetoing b-jets a weight to correct the b-tagging efficiency needs to be applied to MC events.

4.6 Systematic Uncertainties

For Monte Carlo simulated background events a variety of event weights or variation of scales need to be applied to estimate the systematic uncertainties. The following systematic uncertainties are considered:

- The uncertainty on the jet energy scale (JES) [56].
- The uncertainty due to jet energy resolution (JER) [56].
- The uncertainty on the tau energy scale (TES) [57].
- The uncertainty in the tau identification (TIDSF), (TEVSF), (TFAKESF).
- The uncertainty in the tau trigger efficiency (TTRIGSF).
- The uncertainty on the E_T^{miss} energy scale (SCALEST) [58].
- The uncertainty on the E_T^{miss} energy resolution (RESOST) [58].
- The pile-up weight is found to be optimal with an additional scaling factor of 1/1.11. This factor is compared with 1/1.08 and 1/1.14 (PILEUP).
- The b-tagging weight is varied with weights that are corresponding to the b-jet tagging efficiency (BJETEFF), the c-jet tagging efficiency (CJETEFF), and the light jet tagging efficiency (LJETEFF).
- The uncertainty on the integrated luminosity is 3.6%. It is derived following the same methodology as that detailed in [59].
- The theoretical uncertainty on the cross section of Z+jets is $\sim$5% [60]. The uncertainties on the top background are $^{+9,2}_{-10,1}$% for $t\bar{t}$, $^{+4.07}_{-2.69}$%, $^{+4.032}_{-3.89}$%, and $^{+7.43}_{-7.69}$% for the single top t-, s-, and Wt- channels. For the diboson processes the uncertainty is 5% for WW, 5% for ZZ, and 7% for WZ [61].
- The Monte Carlo estimation is also compared with different generators. The nominal samples for W + jets and Z + jets listed in section 4.2.3 are compared with Alpgen [62] samples. For $t\bar{t}$ the baseline Sherpa samples are compared with the MC@Nlo generator. The diboson samples are compared with Herwig [63] samples.

4.7 Event Preselection

Before applying the analysis cuts a set of quality criteria have to be fulfilled.

1. **GRL:** The first cut is to apply the aforementioned Good Run List on all data events to ensure only events are analyzed that were recorded with full detector functionality.

2. **Incomplete events:** In 2012 data-taking the Timing, Trigger and Control (TTC) system restart was developed to recover detector busy conditions. Shortly after a TTC restart there can be incomplete events with missing detector information. These events should be discarded.

3. **LAr & tile error:** If there was a LAr or tile error the event is rejected.

4. **Jet cleaning:** There are two cases, where an event needs to be rejected, because of certain conditions for a jet.
   The first case happens if a jet with $p_T > 20\,\text{GeV}$ is reconstructed, which does not pass the "looser" requirements for jets (see section 4.3.1). Such a jet is called a "bad" jet. If such a jet exists and does not overlap with an electron or tau, then the entire event is discarded.
   The second case to reject an event is fulfilled if a jet is found with $p_T > 40\,\text{GeV}$, which is close to the missing transverse energy vector $\Delta\phi(E_T^{miss}, jet) < 0.3$ and does not pass a quality cut for dead cell corrections.

5. **Primary Vertex:** The primary vertex of an event must have more than four tracks associated to it. Otherwise the event is rejected.

6. **Bad Muons:** If the charge Q and the momentum p of a baseline muon before overlap removal fulfill $\sigma(Q/p)/|Q/p| > 0.2$ the event is rejected.

7. **Cosmic Muons:** Muons after the overlap removal must come from the interaction point. Therefore the longitudinal impact parameter with respect to the primary vertex z_0^{PV} needs to fulfil $|z_0^{PV}| < 1\,\text{mm}$ and the transverse impact parameter with respect to the primary vertex d_0^{PV} is required to have $|d_0^{PV}| < 0.2\,\text{mm}$.

4.8 Signal Regions

The next step after the event preselection is to apply the analysis cuts on physical variables and objects. A complete set of cuts then defines a signal region (SR). For the search of weakly produced SUSY events with taus the following requirements are applied:

- **Tau and trigger requirements:**
  - ≥ 2 taus: At least two baseline taus are required to be in the event. One of the taus has to fulfill the "tight" BDT threshold. No additional light leptons are allowed.
  - Trigger plateau: The offline trigger thresholds are required. If the ditau trigger has fired events are discarded if they do not have two taus with $p_T(\tau_1) > 40\,\text{GeV}$ and $p_T(\tau_2) > 25\,\text{GeV}$. If the E_T^{miss} trigger has fired events are rejected if the missing transverse energy is not $E_T^{miss} > 150\,\text{GeV}$. This ensures that the corresponding trigger is in its plateau. Later in this section also a general E_T^{miss} cut is introduced that is applied to all events.

  - Trigger: The event needs to be triggered by either the ditau or the E_T^{miss} trigger.
  - Trigger matching: In case the event is selected by the ditau trigger it is checked in addition if two taus can be matched to the trigger objects. Both trigger taus need to be in $\Delta R < 0.2$ range to an offline tau.
  - Opposite Charge: The decay of a chargino or slepton pair leads to a pair of leptons with opposite charges. Thus at least one pair of taus with opposite charge is required.

- **Jet veto:** Since no gluons or quarks are produced in the analyzed SUSY decay process, no high energetic jets are expected. Therefore a jet veto is applied to the events. Due to initial state radiation there might still be some jets in a SUSY event. Hence one of the signal regions is defined with a veto only on b-jets instead of all signal jets.

- **Z veto:** To suppress the contributions of the Standard Model Z + jets processes,

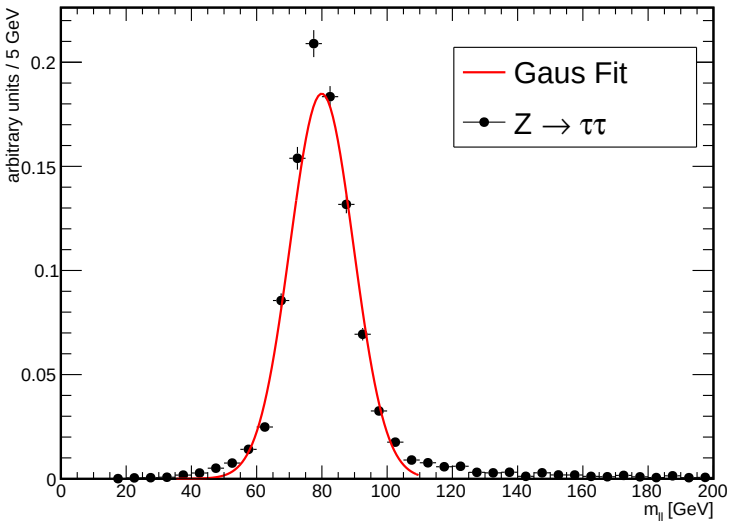

Figure 4.5: Invariant mass distribution of the tau pair for MC generated $Z \to \tau\tau$ events with a Gaussian fit.

which also produce an event signature with two taus, no jets, and some E_T^{miss}, a Z veto is chosen for the invariant mass of the opposite sign tau pair. Since the neutrino in the tau decay is not included in the reconstructed tau object, some of the energy is missing. In general the invariant mass of a pair of tau objects emerging from a Z boson decay will be lower than the original Z mass $m_Z = 91.2\,\text{GeV}$. To define a proper Z veto the invariant mass distribution of Monte Carlo generated $Z \to \tau\tau$ events is investigated. The distribution peaks at a value below 91 GeV. A Gaussian fit of the peak yields a mean value of $80.01 \pm 0.1\,\text{GeV}$. Therefore the

Z veto is chosen such that all events with $|m_{\tau\tau} - 80\,\text{GeV}| < 10\,\text{GeV}$ are rejected. The distribution and Gaussian fit are shown in figure 4.5.

- $\mathbf{E_T^{miss}}$**:** The LSPs and the neutrinos in the analyzed SUSY processes lead to a high amount of missing energy in the event. A cut on $E_T^{miss} > 40\,\text{GeV}$ also suppresses a large amount of Standard Model background such as QCD multi-jet or diboson events.

- $\mathbf{m_{T2}}$**:** The "stransverse mass" m_{T2} is the most sensitive variable used to select weakly produced SUSY events. A cut of $m_{T2} > 90\,\text{GeV}$ or $m_{T2} > 100\,\text{GeV}$ is used for different signal regions.

Two signal regions (SR) "OS-m_{T2}" and "OS-m_{T2}-nobjet" are defined. The specific cuts of each SR are listed in table 4.4. The cut values were optimized by other members of the SUSY working group for the analysis in [38].

Signal Region	Requirements
OS-m_{T2}	$\geq 2\tau's$, 1 OS pair
	signal jet veto
	Z veto
	$E_T^{miss} > 40\,\text{GeV}$
	$m_{T2} > 90\,\text{GeV}$
OS-m_{T2}-nobjet	$\geq 2\tau's$, 1 OS pair
	b-jet veto
	Z veto
	$E_T^{miss} > 40\,\text{GeV}$
	$m_{T2} > 100\,\text{GeV}$

Table 4.4: Signal region definition.

4.9 Monte Carlo Based Background Contribution to the Signal Regions

A first estimation of the Standard Model background can be given with the direct use of the available Monte Carlo samples. But the statistics and physical accuracy of the Monte Carlo simulations has its limitations. Most of the Monte Carlo samples have only very few or no events left in the signal regions. The event yield of the background processes is summarized in table 4.5. While no events at all of the Z + jets, $t\bar{t}$, and Single Top processes are left in signal region OS-m_{T2}, the W + jets background is rather high. However only two events in signal region OS-m_{T2} and five in OS-m_{T2}-nobjet produce

the high event yield and high error for W + jets after scaling to $20.3\,\mathrm{fb}^{-1}$ luminosity. The QCD multi-jet processes are missing completely, because no sample with enough statistics exists.
In the next chapter methods to estimate the background with lower uncertainty are described. The contribution from QCD multi-jet and W + jets will be estimated from data. The other contributions will be estimated from MC and additional methods will be applied to improve the statistics.

SM Process	OS-m_{T2}	OS-m_{T2}-nobjet
W + Jets	26.42 ± 25.10	49.48 ± 31.34
Z + Jets	0 ± 1.0	0.70 ± 0.7
$t\bar{t}$	0 ± 1.0	0.87 ± 0.48
Single Top	0 ± 1.0	0.44 ± 0.44
Diboson	1.91 ± 0.28	2.74 ± 0.49
SM Total	28.33 ± 25.10	54.23 ± 31.36

Table 4.5: Summary of the event yields from Standard Model Monte Carlo samples. The numbers are scaled to the luminosity of the analyzed data $\int \mathcal{L}\,\mathrm{dt} = 20.3\,\mathrm{fb}^{-1}$.

5 Background Estimation

Other members of the ATLAS SUSY working group developed the methods and derived the numbers that are presented in this chapter. The methods are presented for completeness to be compared with the alternative methods presented in chapter 6.

5.1 QCD Multi-Jet and W + Jets

The dominant Standard Model background to this analysis is the QCD multi-jet production. To be identified as a ditau event at least two jets have to be misidentified as taus. To suppress influences from "fake" taus, good tau identification quality is required for the signal regions. Also the E_T^{miss} requirement reduces the multi-jet contribution greatly. However it is not negligible due to the large cross-sections of QCD multi-jet processes. The MC datasets with simulated QCD multi-jet events are very limited to describe this properties. The simulation of jets faking taus and E_T^{miss} is not well described. The biggest problem is the huge statistics needed to obtain proper distributions of QCD multi-jet background events in the signal regions of this analysis. With the currently available datasets only very few events remain after the signal cuts. These events are not enough for proper interpretations. Thus an alternative method to estimate the QCD multi-jet background from data is described in this section. This method is called "ABCD method" and is introduced in [38]. The ABCD method estimating the QCD multi-jet contribution to the signal regions is greatly influenced by W + jets processes. The ditau event topology can only be generated in W + jets decay events if at least one tau is generated by a misinterpreted jet in the event. Thus the W + jets events have similar properties as QCD multi-jet events concerning their tau identification quality. In principle one could subtract the W + jets contribution with the estimation from Monte Carlo simulation, like it is done with other Standard Model processes. But fake taus are not well described in the simulation and the W + jets would have to be estimated from data as well. This estimation would be dominated by the QCD multi-jet background then. Because of their similar properties the QCD multi-jet and W + jets background are estimated together with the ABCD method as the entire fake tau contribution.

5.1.1 The ABCD Method

In the ABCD method the contribution of a certain process in a signal region "D" is estimated from three control regions "A", "B", and "C". To define these regions two variables are chosen, which should not be correlated in the optimal case. A schematic overview is shown in figure 5.1. In this picture the two variables are drawn on the x and y axis.

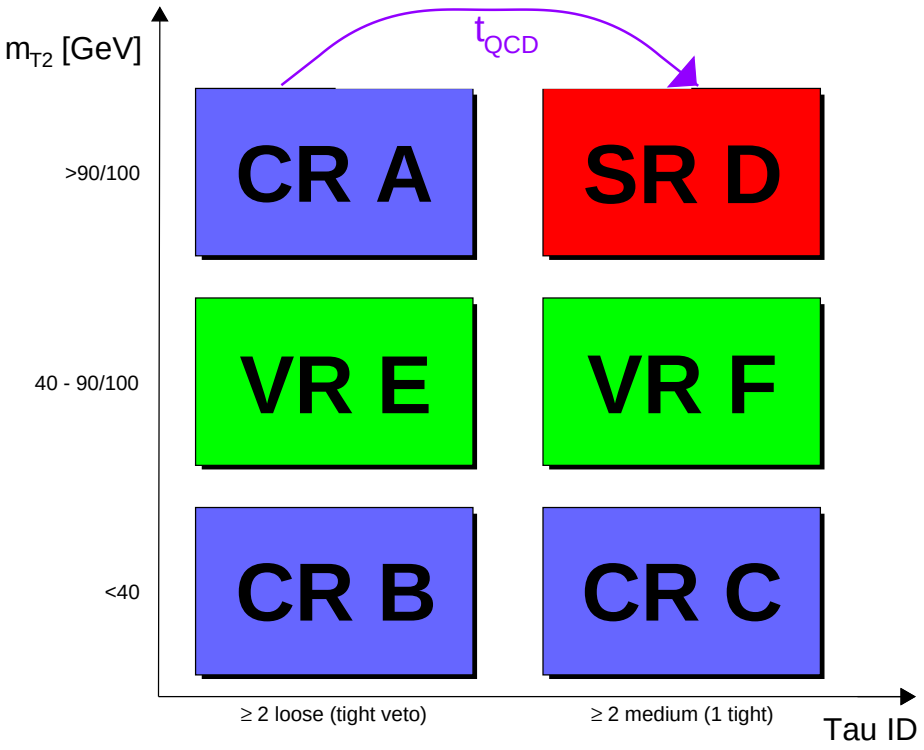

Figure 5.1: Schematic drawing of the ABCD regions with the definitions of the control regions for the QCD multi-jet and W + jets estimation. The two variables m_{T2} and Tau ID are displayed as the axes of a two dimensional space. The control regions A, B, and C are shown in blue, the signal region is shown in red, and the validation regions for cross checks and systematics are shown in green. The contribution of the background in the signal region D can be estimated from control region A with the transfer factor t_{QCD} (violet).

With the first variable on the x axis a split into two regions is defined. The first region is shown on the right side in the picture and has the definition for the signal region for this variable and consists of the signal region D, the control region C (and the validation region F). The second region on the left side consists of control region A and B (and the validation region E). This region uses complementary cuts that define a region where the background process that needs to be estimated is dominating. The other variable on the y axis then divides the two regions into the final four (six with the validation regions). The uppermost regions in the picture A and D have the signal region cut for the second variable, while the bottom regions B and C use a complementary cut, which defines regions that are more dominated by the background process. (Between the upper and lower regions the validation regions are defined.)
If the correlation between the variables is weak, the ratios between the four regions fulfill $C/B = D/A$. Thus the estimation of one background process (x) in signal region D can

be estimated from the background dominated control region A with the multiplication of the transfer factor $t_x = C/B$. The control regions should have a good purity of the desired background process so that the estimation from data is not influenced by other processes that might have a different transfer factor. Moreover the control regions should be chosen as close as possible to the signal region to avoid extrapolation problems.

Regions	QCD multi-jet + W Control regions			Signal Region
	A	B	C	D
OS-m_{T2}	≥ 2 loose taus tight tau veto $m_{T2} > 90\,\text{GeV}$	≥ 2 loose taus tight tau veto $m_{T2} < 40\,\text{GeV}$	≥ 1 medium taus ≥ 1 tight taus $m_{T2} < 40\,\text{GeV}$	≥ 1 medium taus ≥ 1 tight taus $m_{T2} > 90\,\text{GeV}$
OS-m_{T2}-nobjet	≥ 2 loose taus tight tau veto $m_{T2} > 100\,\text{GeV}$	≥ 2 loose taus tight tau veto $m_{T2} < 40\,\text{GeV}$	≥ 1 medium taus ≥ 1 tight taus $m_{T2} < 40\,\text{GeV}$	≥ 1 medium taus ≥ 1 tight taus $m_{T2} > 100\,\text{GeV}$

Table 5.1: Summary of the cut regions used for the ABCD method to estimate the QCD multi-jet and W + jets in both signal regions. [38]

To estimate the QCD multi-jet & W + jets background the tau identification criterion is used as the first variable to distinguish between the signal region and the control region. As explained in the previous chapter (4.3.2) the signal taus need to fulfill the "medium" threshold for the jet BDT score and for the signal regions one tau needs to be "tight" in addition. However for the control regions A and B this is inverted and only the "loose" threshold is required and "tight" taus are vetoed. This yields a region where the contribution of fake taus from jets is higher while real taus are rejected. The second variable is the stransverse mass m_{T2}. In a region above $90-100\,\text{GeV}$ the Standard Model processes are suppressed and SUSY processes become dominant, while in the inverted region the background processes are much more relevant. For region A and D the cut $m_{T2} > 90\,\text{GeV}$ is chosen for signal region OS-m_{T2} and $m_{T2} > 100\,\text{GeV}$ for signal region OS-m_{T2}-nobjet. As a complementary cut for the control regions B and C $m_{T2} < 40\,\text{GeV}$ is chosen. In this range the other Standard Model processes are almost negligible and the fake tau processes are dominating. The range $40\,\text{GeV} < m_{T2} < 90/100\,\text{GeV}$ defines the validation regions E and F. They are used as a cross check and for the uncertainty estimation of the correlation between the tau identification and m_{T2}. All other cuts for the control regions are the same as in the corresponding signal region. The definition of the regions is summarized in table 5.1.
Figure 5.2 and 5.3 show the m_{T2} distributions for the tight and loose tau identification criteria chosen for the control regions. In these histograms the Standard Model backgrounds are stacked and the W + jets contribution is taken from the Monte Carlo datasets. An overview of the numbers is given in tables 5.2 and 5.3. To obtain the QCD multi-jet & W + jets contribution in the different control regions, the other backgrounds need to be subtracted from the data events.

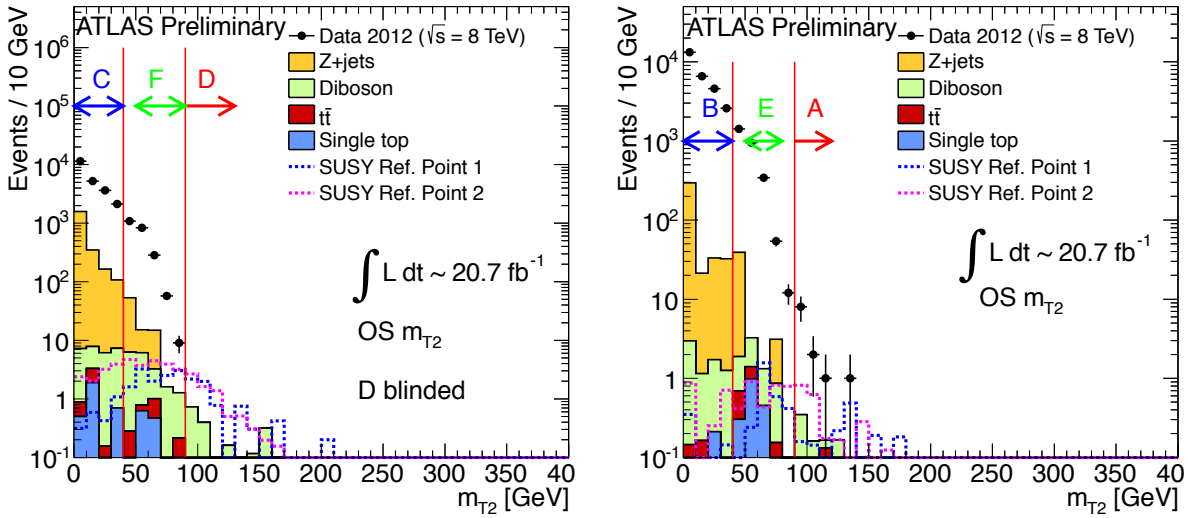

(a) ≥ 2 Medium Taus (1 Tight) (b) ≥ 2 Loose Taus (Tight Veto)

Figure 5.2: m_{T2} distribution for the OS-m_{T2} signal region before applying the m_{T2} cut (5.2a). In (5.2b) the tau identification criteria are changed to ≥ 2 loose taus with tight tau veto instead of ≥ 1 medium taus and ≥ 1 tight taus. The Standard Model backgrounds are stacked. Together the two histograms show the distribution in all regions of the ABCD method for the QCD multi-jet & W + jets estimation. [38]

	region A	region B	region C	region E	region F	t_{QCD}	QCD+W in SR
Data	12	26932	22382	2781	2270		
Z+jets	-	$(3.7 \pm 0.6) \times 10^2$	$(2.13 \pm 0.19) \times 10^3$	40±23	68±21		
di-boson	0.84±0.22	6.6±0.8	23.1±1.3	4.8±0.7	15.8±1.2		
single top	-	0.21±0.21	3.1±1.9	1.7±1.1	1.1±0.5	0.760	8.4
$t\bar{t}$	0.13±0.13	0.31±0.20	2.0±0.7	1.0±0.4	1.2±0.4	±0.010	±3.0
Drell-Yan	-	0.7±0.7	43±25	-	-		
Multi-jet, W+jets	11.0±3.5	$(2.655 \pm 0.018) \times 10^4$	$(2.018 \pm 0.024) \times 10^4$	$(2.73 \pm 0.06) \times 10^3$	$2.08 \pm 0.04 \times 10^3$		
Ref. P1	1.5 ±0.5	0.6±0.3	2.4±0.6	2.9±1.4	12.4±1.5		
Ref. P2	2.2±0.4	1.9±0.4	11.5±1.1	3.4±0.5	20.0±1.1		

Table 5.2: Expected backgrounds in the OS-m_{T2} QCD multi-jet and W + jets background control region and validation region and the estimate of the QCD multi-jet and W + jets background contribution in the signal regions. The uncertainty in the last column is the total uncertainty on the multi-jet and W + jets background estimate, including both statistical and systematic uncertainties. For comparison also the expected SUSY signal from the reference points SUSY Ref. P1 and SUSY Ref. P2 is shown. [38]

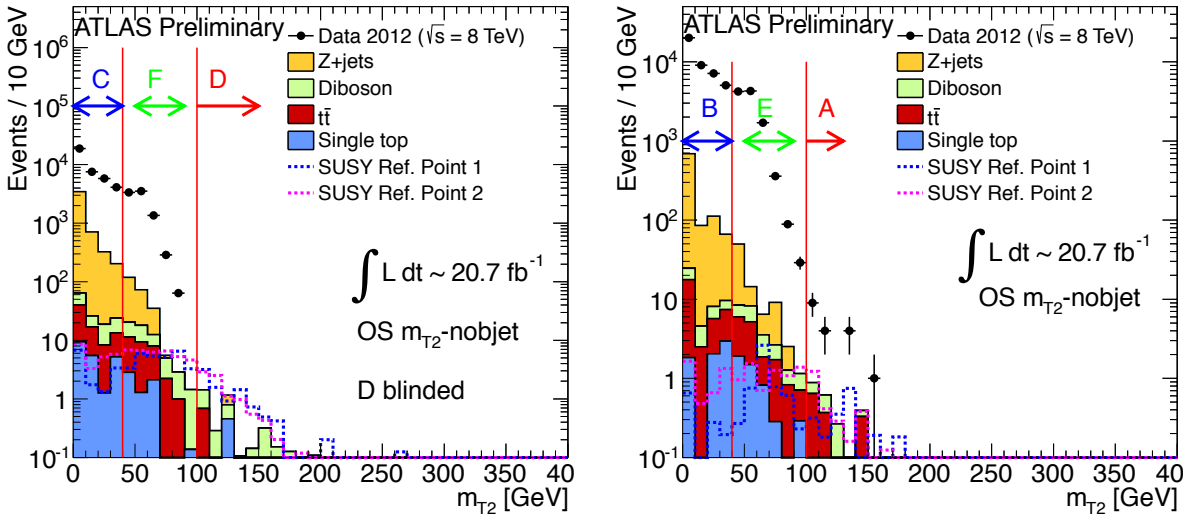

(a) ≥ 2 Medium Taus (1 Tight)

(b) ≥ 2 Loose Taus (Tight Veto)

Figure 5.3: m_{T2} distribution for the OS-m_{T2}-nobjet signal region before applying the m_{T2} cut (5.3a). In (5.3b) the tau identification criteria are changed to ≥ 2 loose taus with tight tau veto instead of ≥ 1 medium taus and ≥ 1 tight taus. The Standard Model backgrounds are stacked. Together the two histograms show the distribution in all regions of the ABCD method for the QCD multi-jet & W + jets estimation. [38]

	region A	region B	region C	region E	region F	t_{QCD}	QCD+W in SR
Data	18	41372	36291	10652	8597		
Z+jets	-	$(9.0 \pm 1.0) \times 10^2$	$(4.47 \pm 0.21) \times 10^3$	56±24	175±29		
di-boson	0.98±0.23	13.6±1.1	52.2±2.0	8.9±0.9	26.8±1.4		
single top	-	6.8±2.5	21±4	4.8±1.5	6.4±1.8	0.782	12
$t\bar{t}$	1.3±0.6	26.3±2.8	51.6±3.5	13.6±2.0	23.5±2.4	±0.008	±5
Drell-Yan	-	9±5	89±30	2.1 ±1.3	2.1±2.1		
Multi-jet, W+jets	16±4	$(4.042 \pm 0.022) \times 10^4$	$(3.160 \pm 0.029) \times 10^4$	$(1.057 \pm 0.011) \times 10^3$	$(8.26 \pm 0.08) \times 10^3$		
Ref. P1	2.0±0.6	1.2±0.4	13.3±0.2	5.3±1.5	29.7±2.2		
Ref. P2	2.6±0.4	4.1±0.5	22.8±1.4	6.9±0.7	36.3±1.5		

Table 5.3: Expected backgrounds in the OS-m_{T2}-nobjet QCD multi-jet and W + jets background control region and validation region and the estimate of the QCD multi-jet and W + jets background contribution in the signal regions. The uncertainty in the last column is the total uncertainty on the multi-jet and W + jets background estimate, including both statistical and systematic uncertainties. For comparison also the expected SUSY signal from the reference points SUSY Ref. P1 and SUSY Ref. P2 is shown. [38]

5.1.2 Uncertainties

Several systematic uncertainties are evaluated for the ABCD method.

- **Purity:** To obtain an estimation method for the QCD multi-jet background from data, the control regions are supposed to have only small contributions of the other Standard Model background processes. The other Standard Model backgrounds only reach $\sim 10\%$ of the event yields of the data distributions in the control regions B and C. In the validation regions E and F the W + jets background is getting more relevant. However the distributions have strong statistical fluctuations. Therefore the estimation of the transfer factor is done in the purely QCD multi-jet dominated lower m_{T2} region. A systematic uncertainty can be calculated with the systematic errors of each non-QCD background contribution in region A.

- **Correlation:** The correlation between m_{T2} and the tau identification needs to be low, so the transfer factor t_{QCD} obtained from regions C/B can be used to estimate the contribution in signal region D from A. The uncertainty for the correlation of the variables is calculated using the transfer factor from the validation regions E and F which fill the gap in the m_{T2} distributions between 40 GeV and 90/100 GeV. The relative difference of the transfer factor is then used as the systematic uncertainty for the correlation.

- **Difference in the transfer factor between W + jets and QCD multi-jet:** The background contribution of QCD multi-jet events with two jets misidentified as taus and the W + jets background, where at least one tau is coming from a misidentified jet are estimated together in the ABCD method. In the control regions the W + jets contribution is small. However, in the W + jets events, there is generally one real tau. This may influence the transfer factor between the loose tau and the tight tau regions. A systematic uncertainty is calculated from the difference between the transfer factor t_{QCD}, which is estimated in the region $m_{T2} < 40$ GeV, and the transfer factor t_W. t_W is calculated from the W + jets Monte Carlo sample in the complete region $m_{T2} < 90/100$ GeV below the signal regions.

The final estimation with both the statistical and the systematic uncertainty is listed in table 5.4. An overview of the uncertainties derived for this estimation is presented in table 5.5.

OS-m_{T2}	OS-m_{T2}-nobjet
$8.4 \pm 2.6 \pm 1.4$	$12 \pm 3 \pm 3$

Table 5.4: QCD multi-jet & W + jets estimation in the signal regions. The first uncertainty is the statistical uncertainty and the second uncertainty is the systematic uncertainty. [38]

Systematic Error	OS-m_{T2}	OS-m_{T2}-nobjet
Correlation	5%	1%
Transfer factor difference	15%	24%
Subtraction of other backgrounds	2%	6%
Statistics region A	31%	27%
Total	35%	37%

Table 5.5: Summary of the relative systematic uncertainties of the ABCD method for the QCD multi-jet & W + jets estimation in the signal regions. [38]

5.2 Z + Jets and Drell-Yan

The Z + jets and Drell-Yan contribution in the signal regions predicted from the Monte Carlo samples is statistically limited. In signal region OS-m_{T2} no events at all are left after the final m_{T2} cut. Therefore the estimation is improved with an "ABCD"-like method, which is completely Monte Carlo driven [38]. For the Z + jets background estimation it is not possible to apply a data driven or semi data driven method, because every possible control region would be dominated by the QCD multi-jet background, which prevents a precise prediction for Z + jets.

Regions	Z + Jets Control Regions			Signal Region
	A	B	C	D
OS-m_{T2}	≥ 2 loose taus	≥ 2 loose taus	≥ 1 medium taus ≥ 1 tight taus	≥ 1 medium taus ≥ 1 tight taus
	$E_T^{miss} > 0\,\text{GeV}$ $m_{T2} > 90\,\text{GeV}$	$E_T^{miss} > 0\,\text{GeV}$ $40 < m_{T2} < 80\,\text{GeV}$	$E_T^{miss} > 40\,\text{GeV}$ $40 < m_{T2} < 80\,\text{GeV}$	$E_T^{miss} > 40\,\text{GeV}$ $m_{T2} > 90\,\text{GeV}$
OS-m_{T2}-nobjet	≥ 2 loose taus	≥ 2 loose taus	≥ 1 medium taus ≥ 1 tight taus	≥ 1 medium taus ≥ 1 tight taus
	$E_T^{miss} > 0\,\text{GeV}$ $m_{T2} > 100\,\text{GeV}$	$E_T^{miss} > 0\,\text{GeV}$ $40 < m_{T2} < 80\,\text{GeV}$	$E_T^{miss} > 40\,\text{GeV}$ $40 < m_{T2} < 80\,\text{GeV}$	$E_T^{miss} > 40\,\text{GeV}$ $m_{T2} > 100\,\text{GeV}$

Table 5.6: Summary of the regions used for the "ABCD"-like method to estimate the Z + jets and Drell-Yan background in both signal regions.

Similar to the method in the previous section three control regions A, B, and C are chosen in addition to the signal region D. These control regions are defined with two sets of variables which are assumed to be only weakly correlated. The cuts on these variables are chosen in a way that the control regions yield a good amount of Z + jets events. With a constant ratio over the complete range of the variables the control regions fulfill the relation $C/B = D/A$. The event yield in the signal region can be estimated with the transfer factor $t = C/B$ as $D = t \cdot A$. The estimation in the signal region is just a scaling on the Monte Carlo simulation. With better statistics in the control regions the

low event count in the signal regions can be neglected and a prediction of the background process can be given with less uncertainty.
The definition of the control regions is summarized in table 5.6. The estimation into the signal region from the "ABCD"-like method is listed in table 5.7 together with the original prediction from the Monte Carlo datasets.

Z + Jets	OS-m_{T2}	OS-m_{T2}-nobjet
MC Prediction	0±1.0	0.70±0.70
"ABCD" Method	$0.28 \pm 0.26 \pm 0.23$	$0.4 \pm 0.3 \pm 0.3$

Table 5.7: Z + jets background contribution to the signal regions. The estimations are taken from the Monte Carlo generated datasets and from the "ABCD"-like method. [38]

5.3 $t\bar{t}$ and Single Top

Regions	Z + Jets Control Regions			Signal Region
	A	B	C	D
OS-m_{T2}	≥ 2 loose taus $E_T^{miss} > 0\,\text{GeV}$ $m_{T2} > 90\,\text{GeV}$	≥ 2 loose taus $E_T^{miss} > 0\,\text{GeV}$ $40 < m_{T2} < 80\,\text{GeV}$	≥ 1 medium taus ≥ 1 tight taus $E_T^{miss} > 40\,\text{GeV}$ $40 < m_{T2} < 80\,\text{GeV}$	≥ 1 medium taus ≥ 1 tight taus $E_T^{miss} > 40\,\text{GeV}$ $m_{T2} > 90\,\text{GeV}$
OS-m_{T2}-nobjet	≥ 2 loose taus $E_T^{miss} > 0\,\text{GeV}$ $m_{T2} > 100\,\text{GeV}$	≥ 2 loose taus $E_T^{miss} > 0\,\text{GeV}$ $40 < m_{T2} < 80\,\text{GeV}$	≥ 1 medium taus ≥ 1 tight taus $E_T^{miss} > 40\,\text{GeV}$ $40 < m_{T2} < 80\,\text{GeV}$	≥ 1 medium taus ≥ 1 tight taus $E_T^{miss} > 40\,\text{GeV}$ $m_{T2} > 100\,\text{GeV}$

Table 5.8: Summary of the control regions used for the ABCD method to estimate the $t\bar{t}$ and Single Top background in both signal regions.

The $t\bar{t}$ and single top contribution predicted from the Monte Carlo samples suffers the same statistical limitations as the Z + jets background in the signal regions. In signal region OS-m_{T2} no events are left after all cuts and in signal region OS-m_{T2}-nobjet few events are left with high statistical uncertainty. To improve the estimation a similar "ABCD"-like method as for the Z + jets background is applied. The definition of the control regions is summarized in table 5.8.
The estimation into the signal region from the "ABCD"-like method is listed in table 5.9 together with the original prediction from the Monte Carlo datasets.

$t\bar{t}$ and Single Top	OS-m_{T2}	OS-m_{T2}-nobjet
MC Prediction	0±1.0	1.32±0.66
$t\bar{t}$	0±1.0	0.87±0.48
Single Top	0±1.0	0.44±0.44
"ABCD" Method	$0.2 \pm 0.5 \pm 0.1$	$1.6 \pm 0.8 \pm 1.2$

Table 5.9: $t\bar{t}$ and Single Top background contribution to the signal regions. The estimations are taken from the Monte Carlo generated datasets and from the "ABCD"-like method. [38]

5.4 Diboson

The diboson Monte Carlo samples have enough statistics even in the high m_{T2} range. Thus an "ABCD"-like method is not needed to improve the estimation. The signal region predictions for the dibosonic background estimation are listed in table 5.10.

Diboson	OS-m_{T2}	OS-m_{T2}-nobjet
MC Prediction	$2.2 \pm 0.5 \pm 0.5$	$2.5 \pm 0.5 \pm 0.9$

Table 5.10: Diboson background contribution to the signal regions. The estimations are taken from the Monte Carlo generated datasets. [38]

6 Alternative Method for the Z + Jets and Top Estimation

In this chapter alternative approaches to the "ABCD"-like method, which was used for the estimation of the Z + jets and top background in the previous chapter, are presented. With a different choice of variables that define the control regions we try to improve the statistics in these regions and to reduce the uncertainty of the background estimation in the signal region.

6.1 Z + Jets and Drell-Yan

For the Z + jets background estimation in [38] the tau identification criteria and the missing transverse energy E_T^{miss} are used as the first variable and the stransverse mass m_{T2} as the second variable that defines the four regions A, B, C, and D.

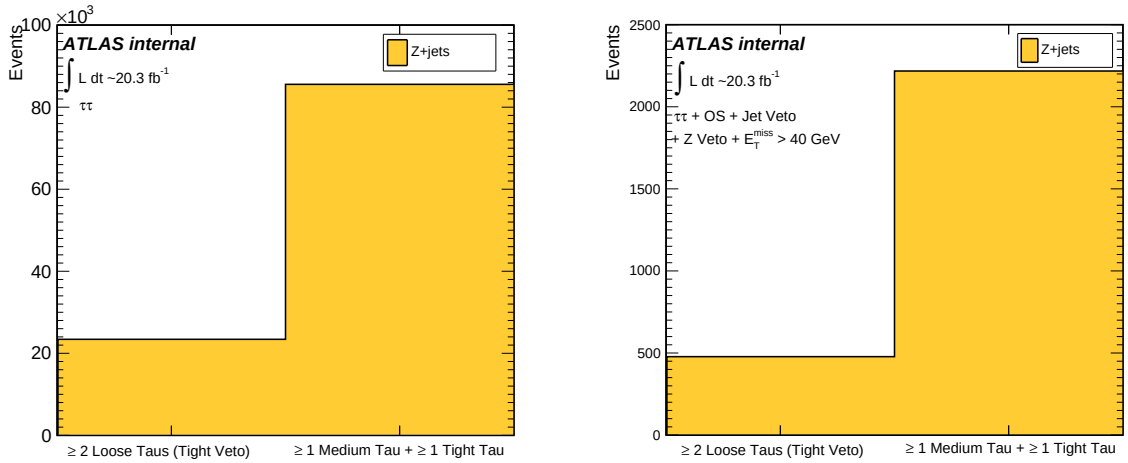

(a) OS-m_{T2} (b) OS-m_{T2}-nobjet

Figure 6.1: Distribution of different tau quality criteria for Monte Carlo generated Z + jets events with the requirement two taus in the event (6.1a) or with the requirements of signal region OS-m_{T2} before the m_{T2} cut (6.1b).

But the tau identification criterion is not a good parameter to enrich the statistics for Z + jets events in the control regions. Vetoing the tight taus, as was done for the QCD

multi-jet background, rejects a lot of Z + jets events, because of the overall good quality of reconstructed tau objects in this process. This can be seen in figure 6.1.

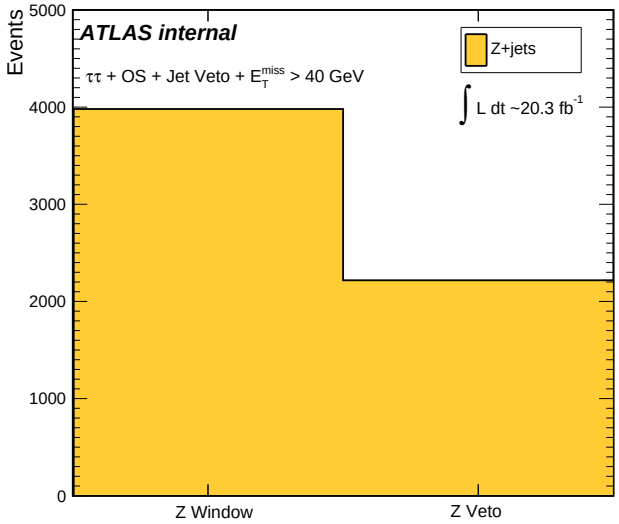

Figure 6.2: Distribution for Monte Carlo generated Z + jets events with a Z veto applied or inside of the Z Window $|m_{\tau\tau} - 80\,\text{GeV}| < 10\,\text{GeV}$.

As an alternative approach the signal region cut on the invariant mass of the tau pair $m_{\tau\tau}$ is inverted for the definition of the control regions A and B. The region $|m_{\tau\tau} - 80\,\text{GeV}| < 10\,\text{GeV}$ was rejected to suppress the Z + jets contribution for the signal regions. To obtain the enriched control regions only the events in this window at the Z peak are selected. The increase of events in the control region can be seen in figure 6.2. As the second variable again the stransverse mass m_{T2} is chosen. The orthogonal range to the signal region cuts $10 < m_{T2} < 90\,\text{GeV}$ for signal region OS-m_{T2} and $10 < m_{T2} < 100\,\text{GeV}$ for signal region OS-m_{T2}-nobjet is chosen for the control regions B and C. Below 10 GeV there is a correlation between m_{T2} and the choice of either a Z veto or window. Therefore this is excluded for the control regions.

The definition of the control regions is summarized in table 6.1. In figure 6.3 the m_{T2} distributions of the selection with Z veto for regions C and D is compared with the distribution for control regions A and B where the $m_{\tau\tau}$ is inside the Z window. The distributions are scaled to unity to compare the shape. The shapes look very similar and a low correlation between the m_{T2} and the Z veto/window cut can be assumed. Hence the method should be valid to estimate the Z + jets background from the control regions.

Unfortunately the m_{T2} cut is suppressing the Z + jets background in such a way that even in the enriched Z window no events are left above the signal region cut. Hence region A is empty. This problem can be solved by an extrapolation of the m_{T2} distribution from lower values. To describe the shape of the distribution the function $f(x) = e^{-(\alpha x+\beta)} \cdot x^{\gamma}$ is tried. Several functions have been tested by other members of the ATLAS group for

Regions	Z + Jets Control Regions			Signal Region
	A	B	C	D
OS-m_{T2}	Z Window $m_{T2} > 90\,\text{GeV}$	Z Window $m_{T2} < 90\,\text{GeV}$ $m_{T2} > 10\,\text{GeV}$	Z Veto $m_{T2} < 90\,\text{GeV}$ $m_{T2} > 10\,\text{GeV}$	Z Veto $m_{T2} > 90\,\text{GeV}$
OS-m_{T2}-nobjet	Z Window $m_{T2} > 100\,\text{GeV}$	Z Window $m_{T2} < 100\,\text{GeV}$ $m_{T2} > 10\,\text{GeV}$	Z Veto $m_{T2} < 100\,\text{GeV}$ $m_{T2} > 10\,\text{GeV}$	Z Veto $m_{T2} > 100\,\text{GeV}$

Table 6.1: Summary of the regions used for the "ABCD"-like method to estimate the Z + jets and Drell-Yan background in both signal regions.

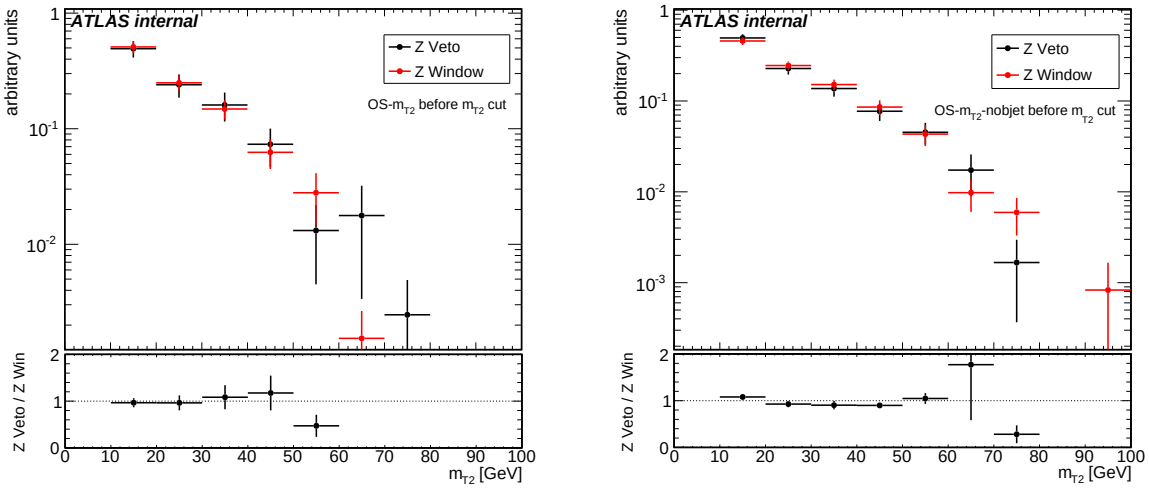

(a) OS-m_{T2} (b) OS-m_{T2}-nobjet

Figure 6.3: m_{T2} distribution for Monte Carlo generated Z + jets events with Z Veto (black) and in the Z Window $|m_{\tau\tau} - 80\,\text{GeV}| < 10\,\text{GeV}$ (red) for signal region OS-m_{T2} (6.3a) and for OS-m_{T2}-nobjet (6.3b). The distributions are scaled to unity to compare the shapes. In the bottom plots the ratio between the distributions with opposing $m_{\tau\tau}$ cut is shown.

the analysis in [38] but this one provided the best fit results.
As a first attempt the fit is applied to a sample where only at least 2 taus, one opposite sign pair, and a signal jet veto are required. In this case the statistical fluctuations of the simulated Z + jets samples are smaller. This is shown in figure 6.4.

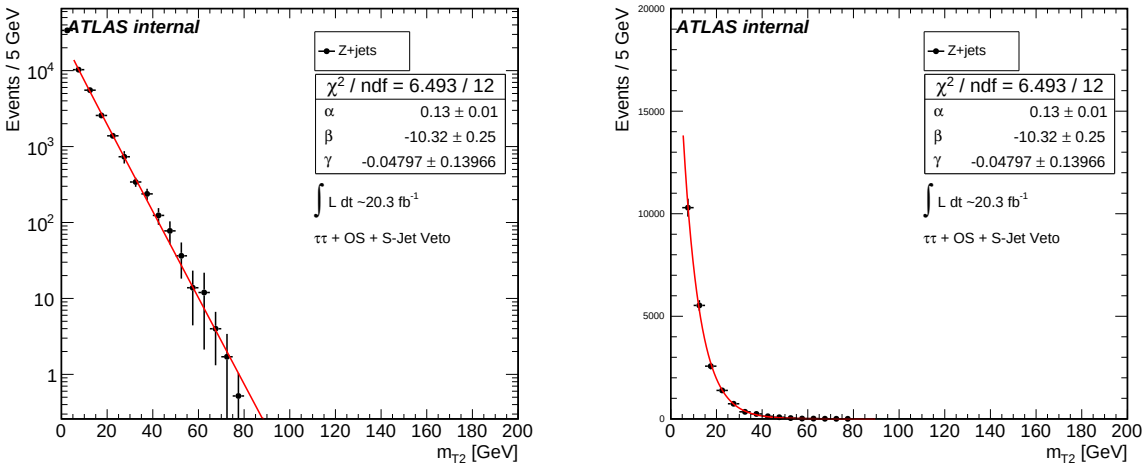

Figure 6.4: m_{T2} distribution in logarithmic (left) and linear (right) scale for Monte Carlo generated Z + jets events with $\geq$ 2 taus, 1 OS pair, and signal jet veto requirement. The fitted function in red is $f(x) = e^{-(\alpha x+\beta)} \cdot x^{\gamma}$.

The fit in this figure is calculated in the range between 5 and 90 GeV to leave out the first bin of the histogram with the entries of the events at 0 GeV, to avoid the case when the algorithm that calculates the stransverse mass m_{T2} fails and returns 0 GeV. The distribution matches the fit function within the statistical uncertainty.
Now the fit function is applied to the distribution in control region B. This is shown in figure 6.5 for both signal regions. Here the fit function does not fit completely to the distribution. But this deviation is due to the distribution of the Z + jets which has high statistical fluctuations. The fit parameters for signal region OS-m_{T2} are $\alpha = 0.184 \pm 0.023$, $\beta = -2.2 \pm 1.7$, and $\gamma = 2.6 \pm 0.7$. For signal region OS-m_{T2}-nobjet the parameters are $\alpha = 0.099 \pm 0.014$, $\beta = -5.7 \pm 1.1$, and $\gamma = 1.0 \pm 0.5$. The function is then extrapolated into the control region A above the signal region cut $m_{T2} > 90\,\text{GeV}$ or $> 100\,\text{GeV}$ respectively. This leads to an event yield in region A of 0.05 ± 0.04 for OS-m_{T2} and 1.7 ± 0.9 for OS-m_{T2}-nobjet. The estimation into the signal region from the "ABCD"-like method is listed in table 6.2 together with the original prediction from the Monte Carlo datasets and it is compared with the estimation in the ATLAS note [38]. The estimated numbers differ from the numbers in the note. In signal region OS-m_{T2} the estimation is smaller but compatible within uncertainty and in signal region OS-m_{T2}-nobjet the estimation is bigger compared to the ATLAS note and the Monte Carlo prediction but fits to it within uncertainty. However, the relative statistical uncertainties are smaller for the estimation presented in this analysis and the estimation is based on control regions with much better statistics. The relative statistical uncertainty for the

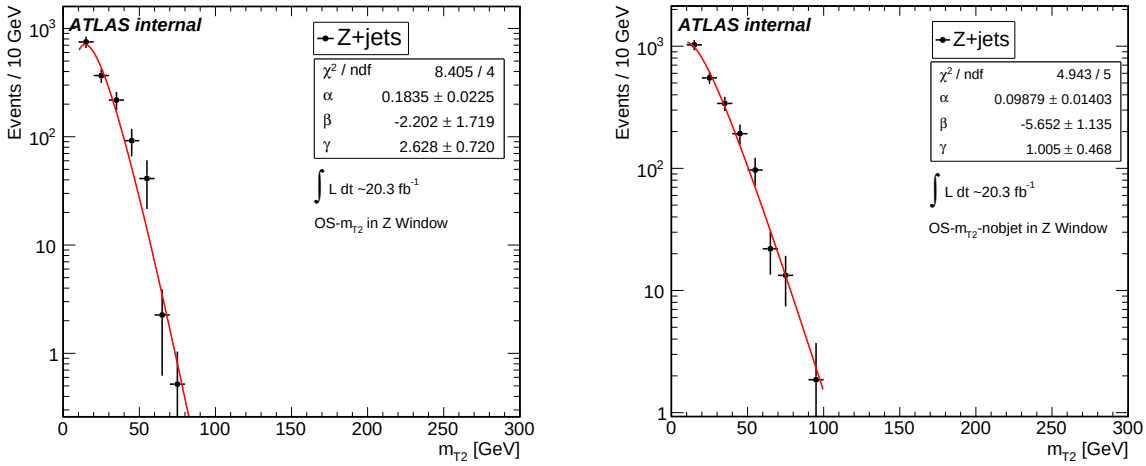

(a) OS-m_{T2} (b) OS-m_{T2}-nobjet

Figure 6.5: m_{T2} distribution for Monte Carlo generated Z + jets events in the Z Window $|m_{\tau\tau} - 80\,\text{GeV}| < 10\,\text{GeV}$ (black) for signal region OS-m_{T2} (6.5a) and for OS-m_{T2}-nobjet (6.5b). The fitted function in red is $f(x) = e^{-(\alpha x+\beta)} \cdot x^{\gamma}$.

Z + jets background prediction is reduced in signal region OS-m_{T2} from 93% to 72% and in signal region OS-m_{T2}-nobjet from 75% to 54%. The statistics in control regions B and C has been improved by a factor of 5 and 10, respectively, for signal region OS-m_{T2} and by a factor of 3 and 8, respectively, for signal region OS-m_{T2}-nobjet. The numbers in the control regions are listed together with a detailed overview of the systematic uncertainties in tables 6.3 and 6.4.

Z + Jets	OS-m_{T2}	OS-m_{T2}-nobjet
MC Prediction	0±1.0	0.7±0.7
"ABCD" Method	$0.025 \pm 0.018^{+0.029}_{-0.014}$	$1.0 \pm 0.6^{+0.9}_{-0.9}$
ATLAS Note	$0.28 \pm 0.26 \pm 0.23$	$0.4 \pm 0.3 \pm 0.3$

Table 6.2: Z + jets background contribution to the signal regions. The estimations are taken from the Monte Carlo generated datasets, from the "ABCD"-like method presented in this thesis, and from the "ABCD"-like method used in the ATLAS note. [38]

	A	B	C	D_{est}	Syst(%)
Nominal MC	0.05±0.04	1472±117	694±77	0.025±0.018	-
Generator	0.04±0.08	1285±74	631±54	0.02±0.04	13.8
Luminosity					3.6
Cross Sec.					5.0
TES up	0.08±0.06	1717±131	973±90	0.043±0.033	+73.3
TES down	0.05±0.04	1167±105	557±65	0.023±0.019	-7.6
TTRIGSF up	0.06±0.04	1548±123	749±84	0.026±0.018	+5.5
TTRIGSF down	0.05±0.04	1398±112	646±72	0.024±0.017	-4.6
TIDSF up	0.06±0.04	1606±128	754±84	0.028±0.020	+13.8
TIDSF down	0.046±0.031	1343±107	637±71	0.022±0.015	-12.7
TEVSF up	0.06±0.04	1740±142	800±89	0.026±0.018	+3.1
TEVSF down	0.050±0.034	1226±96	596±66	0.024±0.017	-2.8
TFAKESF up	0.06±0.04	1490±119	733±81	0.028±0.019	+13.9
TFAKESF down	0.047±0.032	1454±116	657±74	0.021±0.015	-15.4
JES up	0.08±0.06	1552±122	757±82	0.039±0.031	+57.8
JES down	0.038±0.028	1409±114	684±75	0.018±0.014	-27.0
JER	0.06±0.05	1552±123	797±82	0.029±0.026	+15.4
SCALEST up	0.07±0.06	1662±124	871±89	0.038±0.031	+52.4
SCALEST down	0.045±0.034	1294±111	638±73	0.022±0.017	-11.1
RESOST	0.05±0.04	1564±121	773±85	0.024±0.017	-2.2
PILEUP up	0.07±0.05	1492±116	702±76	0.034±0.023	+34.2
PILEUP down	0.03±0.02	1448±119	684±78	0.015±0.011	-38.5
BJETEFF up	0.05±0.04	1471±117	694±77	0.025±0.018	+0.2
BJETEFF down	0.05±0.04	1472±117	694±77	0.025±0.018	+0.1
CJETEFF up	0.05±0.04	1471±117	694±77	0.025±0.018	+0.2
CJETEFF down	0.05±0.04	1473±117	695±77	0.025±0.018	+0.2
LJETEFF up	0.05±0.04	1463±116	690±77	0.025±0.017	-1.9
LJETEFF down	0.05±0.04	1481±118	699±78	0.026±0.018	+2.3
Total				$0.025^{+0.029}_{-0.014}$	+116.2 –55.2

Table 6.3: Summary of the event yields and the systematic uncertainties for signal region OS-m_{T2} in the Z + jets control regions. The second-to-last column shows the estimated Z + jets contribution to the signal region. The last column shows the relative systematic uncertainty. The abbreviations for the systematic uncertainties are explained in section 4.6.

	A	B	C	D_{est}	Syst(%)
Nominal MC	1.7±0.9	2242±132	1397±94	1.0±0.6	-
Generator	0.7±0.4	2143±106	1543±94	0.48±0.30	53.8
Luminosity					3.6
Cross Sec.					5.0
TES up	1.0±0.6	2560±146	1855±109	0.7±0.4	-28.2
TES down	2.2±1.2	1803±118	1183±82	1.4±0.8	+37.3
TTRIGSF up	2.2±1.2	2384±139	1519±102	1.4±0.8	+35.5
TTRIGSF down	1.2±0.6	2106±125	1288±87	0.7±0.4	-30.3
TIDSF up	1.9±1.0	2446±143	1514±101	1.2±0.6	+11.7
TIDSF down	1.5±0.8	2047±121	1285±86	0.9±0.5	-11.6
TEVSF up	1.8±0.9	2654±159	1618±109	1.1±0.6	+3.6
TEVSF down	1.6±0.8	1864±108	1192±80	1.0±0.5	-4.0
TFAKESF up	1.7±0.9	2263±133	1469±99	1.1±0.6	+3.1
TFAKESF down	1.7±0.9	2221±131	1326±89	1.0±0.5	-3.7
JES up	1.5±0.7	2429±138	1546±100	0.9±0.4	-9.6
JES down	2.0±1.0	2075±127	1352±91	1.3±0.7	+23.4
JER	1.9±1.1	2465±140	1583±100	1.2±0.7	+18.7
SCALEST up	1.1±0.8	2485±139	1617±104	0.7±0.5	-28.6
SCALEST down	1.2±0.6	1996±125	1343±96	0.8±0.4	-21.6
RESOST	1.2±0.6	2345±136	1501±101	0.8±0.4	-27.7
PILEUP up	1.6±0.8	2274±130	1419±92	1.0±0.5	-4.4
PILEUP down	1.7±0.9	2206±134	1375±95	1.0±0.6	+0.8
BJETEFF up	1.6±0.9	2238±132	1396±94	1.0±0.5	-5.4
BJETEFF down	1.8±0.9	2245±132	1398±94	1.1±0.6	+5.0
CJETEFF up	1.7±0.9	2234±131	1388±93	1.0±0.6	-0.4
CJETEFF down	1.7±0.9	2249±132	1407±94	1.0±0.6	+0.0
LJETEFF up	1.6±0.9	2223±131	1383±93	1.0±0.5	-3.0
LJETEFF down	1.7±0.9	2261±133	1411±94	1.1±0.6	+2.6
Total				$1.0^{+0.9}_{-0.9}$	+81.7 -83.7

Table 6.4: Summary of the event yields and the systematic uncertainties for signal region OS-m_{T2}-nobjet in the Z + jets control regions. The second-to-last column shows the estimated Z + jets contribution to the signal region. The last column shows the relative systematic uncertainty. The abbreviations for the systematic uncertainties are explained in section 4.6.

6.2 $t\bar{t}$ and Single Top

Also for the $t\bar{t}$ and single top background the method has been optimized with other control regions compared to [38]. The $t\bar{t}$ and single top background are mostly suppressed by the signal jet veto or b-jet veto. Therefore the jet veto cuts are inverted for the enriched control regions. To obtain regions A and B at least one signal jet is required for signal region OS-m_{T2} and at least one b-jet for signal region OS-m_{T2}-nobjet. The second variable to define the control regions is the stransverse mass m_{T2}. The control regions B and C are defined with a $0 < m_{T2} < 90\,\text{GeV}$ cut for signal region OS-m_{T2} and a $0 < m_{T2} < 100\,\text{GeV}$ cut for signal region OS-m_{T2}-nobjet. These two cuts define the orthogonal region to the signal region but leave out the events where the algorithm that calculates the stransverse mass m_{T2} fails and returns 0 GeV. The definition of the control regions is summarized in table 6.5.

Regions	Top Control Regions			Signal Region
	A	B	C	D
OS-m_{T2}	≥ 1 Signal Jet $m_{T2} > 90\,\text{GeV}$	≥ 1 Signal Jet $m_{T2} < 90\,\text{GeV}$ $m_{T2} > 0\,\text{GeV}$	Signal Jet Veto $m_{T2} < 90\,\text{GeV}$ $m_{T2} > 0\,\text{GeV}$	Signal Jet Veto $m_{T2} > 90\,\text{GeV}$
OS-m_{T2}-nobjet	≥ 1 B-jet $m_{T2} > 100\,\text{GeV}$	≥ 1 B-jet $m_{T2} < 100\,\text{GeV}$ $m_{T2} > 0\,\text{GeV}$	B-jet Veto $m_{T2} < 100\,\text{GeV}$ $m_{T2} > 0\,\text{GeV}$	B-jet Veto $m_{T2} > 100\,\text{GeV}$

Table 6.5: Summary of the control regions used for the ABCD method to estimate the $t\bar{t}$ and single top background in both signal regions.

To check the correlation between m_{T2} and the jet requirement, the shapes of the m_{T2} distributions with a b-jet veto and with at least 1 b-jet are compared. The comparison for signal region OS-m_{T2}-nobjet and for a looser selection without the Z veto and the E_T^{miss} cut to further improve the statistics is shown in figure 6.6. The shapes of the distribution look comparable, so that the correlation can be assumed to be rather low. The distribution with a signal-jet cut has too low statistics to be properly compared. Therefore it is assumed that the correlation is as low as for b-jets.
For the top background the control region A for both signal regions is not empty. Therefore the event yield in region A is not estimated with the extrapolation of a fit function like for the Z + jets background. There are large statistical fluctuations but the extrapolation would have an even higher statistical uncertainty.
The estimation into the signal region from the "ABCD"-like method is listed in table 6.6 together with the original prediction from the Monte Carlo datasets and the estimated numbers in the ATLAS note [38]. The estimated numbers differ from the numbers in the note. For both signal regions the estimation is smaller compared to the ATLAS note. However, the relative statistical uncertainties are smaller for the estimation presented in this analysis and the estimation is based on control regions with much better statistics.

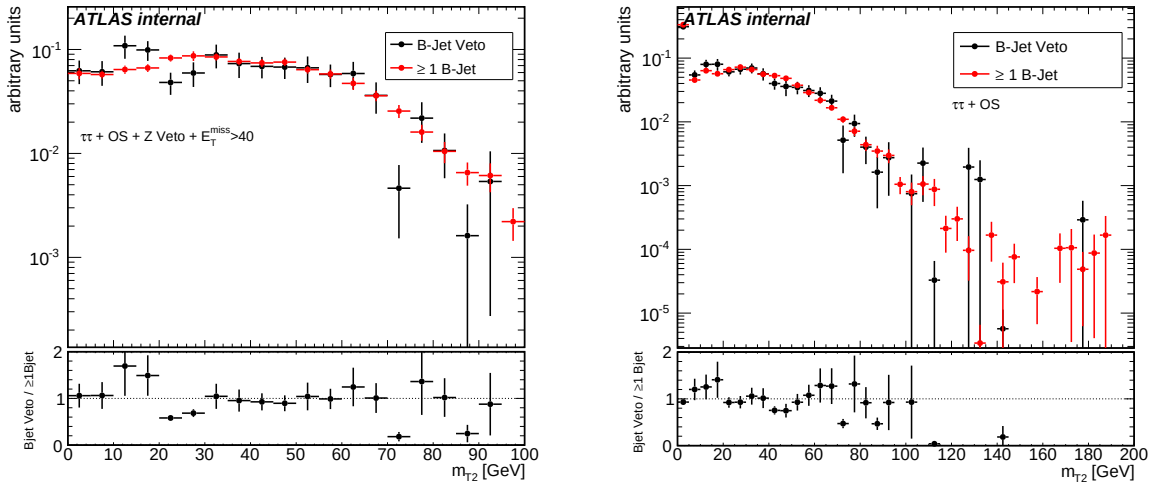

(a) OS-m_{T2}-nobjet (b) $\tau\tau$ + OS

Figure 6.6: m_{T2} distribution for Monte Carlo generated top events with b-jet veto (black) and with ≥ 1 b-jet (red) for OS-m_{T2}-nobjet (6.6a) before the m_{T2} cut and for a looser selection with just a $\tau\tau$ + OS requirement (6.6b) to compare the shapes with higher statistics. The distributions are scaled to unity to compare the shapes. In the bottom plots the ratio between the distributions is shown.

$t\bar{t}$ and Single Top	OS-m_{T2}	OS-m_{T2}-nobjet
MC Prediction	0±1.0	1.3±0.7
$t\bar{t}$, $t\bar{t}W$, $t\bar{t}Z$	0±1.0	0.9±0.5
Single Top, tW	0±1.0	0.4±0.4
"ABCD" Method	$0.13 \pm 0.04^{+0.08}_{-0.07}$	$0.64 \pm 0.14^{+0.35}_{-0.26}$
ATLAS Note	$0.2 \pm 0.5 \pm 0.1$	$1.6 \pm 0.8 \pm 1.2$

Table 6.6: $t\bar{t}$ and single top background contribution to the signal regions. The estimations are taken from the Monte Carlo generated datasets, from the "ABCD"-like method presented in this thesis, and from the "ABCD"-like method used in the ATLAS note [38].

The relative statistical uncertainty for the top background prediction is reduced in signal region OS-m_{T2} from 250% to 31% and in signal region OS-m_{T2}-nobjet from 50% to 22%. The statistics in control regions B and C has been improved by a factor of 158 and 4, respectively, for signal region OS-m_{T2} and by a factor of 7 and 3, respectively, for signal region OS-m_{T2}-nobjet. The numbers in the control regions are listed together with a detailed overview of the systematic uncertainties in tables 6.7 and 6.8.

	A	B	C	D_{est}	Syst(%)
Nominal MC	11.6±1.8	693±16	7.4±2.1	0.13±0.04	-
Generator	4±11	576±68	10±7	0.07±0.22	43.2
Luminosity					3.6
Cross Sec.					7.7
TES up	12.8±1.8	747±16	8.6±2.3	0.15±0.04	+17.1
TES down	10.3±1.8	633±16	6.6±2.1	0.11±0.04	-14.1
TTRIGSF up	12.5±2.0	755±17	8.9±2.7	0.15±0.05	+18.7
TTRIGSF down	10.9±1.6	637±15	6.1±1.7	0.105±0.033	-16.4
TIDSF up	12.1±1.8	730±17	8.1±2.3	0.13±0.04	+6.9
TIDSF down	11.2±1.7	658±15	6.8±2.0	0.12±0.04	-7.4
TEVSF up	12.2±1.8	759±17	8.3±2.3	0.13±0.04	+7.1
TEVSF down	11.1±1.7	632±15	6.6±2.0	0.12±0.04	-7.3
TFAKESF up	15.3±2.4	797±19	8.2±2.6	0.16±0.06	+25.5
TFAKESF down	8.6±1.4	596±13	6.7±1.7	0.097±0.029	-22.6
JES up	13.0±1.9	718±17	5.8±1.2	0.105±0.027	-15.9
JES down	10.9±1.7	667±15	8.5±2.2	0.14±0.04	+11.5
JER	11.6±1.8	714±17	7.4±2.1	0.12±0.04	-4.1
SCALEST up	12.4±1.9	696±16	7.7±2.2	0.14±0.04	+10.6
SCALEST down	11.6±1.8	695±16	7.7±2.2	0.13±0.04	+2.2
RESOST	11.9±1.8	696±16	7.7±2.2	0.13±0.04	+5.4
PILEUP up	11.7±1.8	693±16	7.3±2.1	0.12±0.04	-0.6
PILEUP down	11.5±1.8	693±16	7.5±2.3	0.13±0.04	+0.0
BJETEFF up	11.5±1.7	692±16	7.4±2.1	0.12±0.04	-2.5
BJETEFF down	11.9±1.9	695±16	7.5±2.2	0.13±0.04	+2.7
CJETEFF up	11.6±1.8	693±16	7.4±2.1	0.12±0.04	-0.5
CJETEFF down	11.7±1.8	694±16	7.4±2.1	0.13±0.04	+0.1
LJETEFF up	11.7±1.8	698±16	7.4±2.1	0.12±0.04	-0.7
LJETEFF down	11.6±1.8	689±16	7.5±2.1	0.13±0.04	+0.3
Total				$0.13^{+0.08}_{-0.07}$	+60.1 -57.5

Table 6.7: Summary of the event yields and the systematic uncertainties for signal region OS-m_{T2} in the top control regions. The second-to-last column shows the estimated $t\bar{t}$ and single top contribution to the signal region. The last column shows the relative systematic uncertainty. The abbreviations for the systematic uncertainties are explained in section 4.6.

	A	B	C	D_{est}	Syst(%)
Nominal MC	4.7±0.9	621±15	85±6	0.64±0.14	-
Generator	5±4	531±67	53±16	0.6±0.5	14.1
Luminosity					3.6
Cross Sec.					7.7
TES up	5.9±1.1	670±16	92±6	0.81±0.16	+27.3
TES down	4.2±1.1	567±15	77±6	0.57±0.16	-11.2
TTRIGSF up	5.0±1.0	677±16	94±7	0.69±0.14	+8.5
TTRIGSF down	4.4±0.9	571±14	78±5	0.60±0.13	-6.2
TIDSF up	4.9±1.0	654±16	90±6	0.67±0.14	+4.4
TIDSF down	4.5±0.9	590±14	81±6	0.62±0.13	-3.1
TEVSF up	5.0±1.0	679±16	94±6	0.69±0.14	+7.2
TEVSF down	4.4±0.9	566±14	77±5	0.60±0.13	-5.8
TFAKESF up	6.6±1.4	715±18	98±7	0.90±0.20	+39.9
TFAKESF down	3.2±0.7	534±13	73±5	0.44±0.10	-31.9
JES up	5.0±1.0	645±15	86±6	0.67±0.14	+4.6
JES down	4.1±0.9	595±14	86±6	0.60±0.13	-7.0
JER	4.9±0.9	636±16	91±6	0.70±0.14	+9.0
SCALEST up	4.7±0.9	625±15	85±6	0.64±0.14	-0.0
SCALEST down	4.8±0.9	625±15	83±6	0.64±0.13	+0.5
RESOST	4.5±0.9	623±15	87±6	0.62±0.13	-2.7
PILEUP up	4.8±0.9	622±15	85±6	0.65±0.13	+1.3
PILEUP down	4.6±0.9	620±15	86±6	0.63±0.14	-0.9
BJETEFF up	4.8±1.0	629±15	75±5	0.57±0.12	-10.6
BJETEFF down	4.6±0.9	612±15	96±7	0.72±0.15	+12.5
CJETEFF up	4.7±1.0	622±15	84±6	0.64±0.14	+0.3
CJETEFF down	4.7±0.9	620±15	86±6	0.65±0.14	+1.0
LJETEFF up	4.7±0.9	626±15	84±6	0.63±0.13	-2.0
LJETEFF down	4.7±0.9	616±15	86±6	0.66±0.14	+3.2
Total				$0.64^{+0.35}_{-0.26}$	+55.0 -40.8

Table 6.8: Summary of the event yields and the systematic uncertainties for signal region OS-m_{T2}-nobjet in the top control regions. The second-to-last column shows the estimated $t\bar{t}$ and single top contribution to the signal region. The last column shows the relative systematic uncertainty. The abbreviations for the systematic uncertainties are explained in section 4.6.

7 Validation Regions

In this chapter a cross-check method for the background estimation is presented to prove the validity of the scale factors used. For this analysis this concerns especially the tau trigger and the tau reconstruction scale factors as other scale factors have been validated independently.

7.1 Method

Originally the idea was to estimate the Z+jets and top background in the signal regions with a semi data driven method. With such a method a Monte Carlo simulated background process can be corrected if there are discrepancies between data and Monte Carlo. The correction can be obtained in form of a scaling factor, which would be obtained from the data to Monte Carlo ratio in a specific control region, where the background process that needs to be corrected is highly dominant. This ratio needs to be uncorrelated to the parameter requirements that are different between the control and signal region. To ensure this the control region needs to be defined as closely as possible to the signal region. In the case a control region can be developed for a certain background process A, which has a high purity for this process, the expected number of events in the signal region N_{SR}^{A} can be derived as follows:

$$N_{SR}^{A} = f_A \times N_{SR}^{A}(MC), \tag{7.1}$$

where $N_{SR}^{A}(MC)$ is the number prediction purely from Monte Carlo simulation and f_A is the scaling factor. The scaling factor is defined as:

$$f_A = \frac{N_{CR}^{data} - N_{CR}^{otherSM}}{N_{CR}^{A}(MC)}, \tag{7.2}$$

where N_{CR}^{data} is the number of data events in the control region. $N_{CR}^{otherSM}$ is the number of events from other Standard Model processes. This number should be small. $N_{CR}^{A}(MC)$ is the number of simulated events from the background process A in the control region.

Due to the dominant QCD multi-jet background in this analysis it is not possible to define control regions with good purity and reliable statistics. To suppress the QCD multi-jet background a high cut on the missing transverse energy E_T^{miss} should be applied. However in the E_T^{miss} range above 50 GeV the MC samples do not have enough statistics and the estimation of a scaling factor is not possible without very high uncertainties.

Nevertheless validation regions can be defined, that can be used for a cross-check of the background estimation presented before. Due to the large contribution of Z+jets or top background in such validation regions the validity of the tau scaling factors becomes more relevant than in the signal regions.
In addition the QCD multi-jet background is estimated differently to the method described in section 5.1.
A Z or $t\bar{t}$ decay produces two taus with electrical charges with opposite signs (OS). Thus in the validation regions two oppositely charged taus in the event are required. The probability for taus in Z+jets or top decays to have a misidentified charge is very small. Therefore the same validation regions with a same sign (SS) requirement have almost no contribution from real tau backgrounds. On the other hand the QCD multi-jet background should be equally distributed for both charge combinations of the tau pair. Thus the data events in the SS validation regions can be assumed to be coming almost entirely from QCD multi-jet production. The SS validation regions can be used to estimate the QCD multi-jet contribution in the OS validation regions.
If the MC distributions are comparable to data in the validation regions this would provide a very good validity check.

7.2 Z + Jets

To choose the Z validation region as closely as possible to the signal region, as few changes as possible are applied to the signal region cuts. In the validation region two taus with opposite sign are required. A jet veto is applied as in the signal region OS-m_{T2}. As a starting point also the cut on the transverse missing energy is kept ($E_T^{miss} > 40\,\text{GeV}$). A variation of this cut is discussed later. To achieve sufficient statistics the cut on m_{T2} is inverted ($m_{T2} < 90\,\text{GeV}$) to obtain a completely orthogonal region to the signal regions. The Z-veto cut is inverted, since this cut is meant to suppress mostly the Z+jets background in the signal regions. As explained in section 4.8, the invariant mass of the tau pair has a peak below the Z mass, because some of the energy is taken by the invisible neutrinos produced in the tau decay. The choice of a "Z Window" cut on the invariant mass of the tau pair with $|m_{\tau\tau} - 80\,\text{GeV}| < 10\,\text{GeV}$ is shown in figure 7.1.
To further reduce the QCD multi-jet contribution in this region two "tight" taus are required instead of the baseline selection for the signal regions of one "medium" and one "tight" tau. The increased tau quality requirement should reject events from QCD multi-jet background, in which jets are faking taus and no real taus are present. The difference between these two requirements on the tau identification is shown in figure 7.2. The requirement of two "tight" taus reduces the amount of data events by almost a factor of 2, while almost all Z + jets events fulfill this requirement.
In a Z decay with no jets in the event the momentum conservation leads to a back-to-back event topology for the two taus. Therefore the $\Delta\phi$ and ΔR between the two taus is investigated to further improve the validation region. This is shown in figures 7.3 and 7.4. The $\Delta\phi$ distribution peaks at 180° for Z + jets. The other processes have

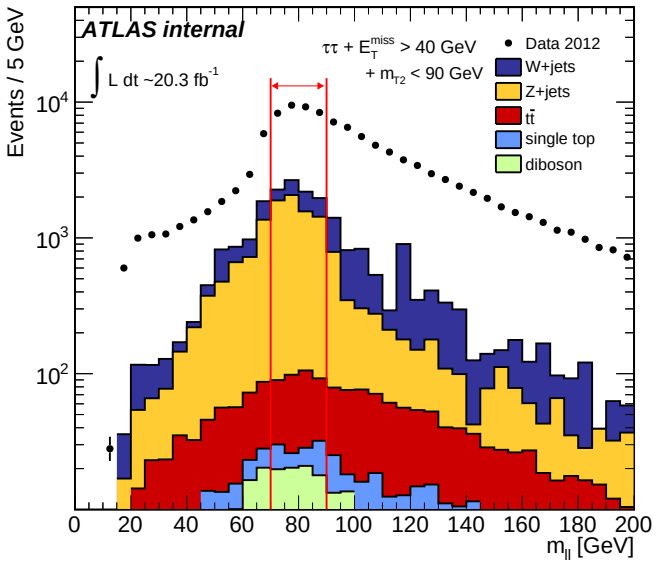

Figure 7.1: Distribution of the invariant mass of the tau pair $m_{\tau\tau}$. Prerequirements for this distribution are two taus in the event, $E_T^{miss} > 40\,\text{GeV}$, and $m_{T2} < 90\,\text{GeV}$. The difference between the data event yield and the stacked simulated background predictions is expected to be from the QCD multi-jet background.

a broader distribution and thus the ratio of Z + jets events can be improved with a cut. Thus $\Delta\phi > 2.5$ is chosen. Since ΔR and $\Delta\phi$ are highly correlated, an additional cut on ΔR would not further improve the exclusion of other backgrounds (see figure 7.4b). In the ΔR distribution the area below 2.5 is already rejected with the $\Delta\phi$ cut. To further improve the purity of Z + jets events in the validation region only events with high ΔR above 3.5 are a possibility. These values correspond to events with high $\Delta\eta$, which corresponds to particles in forward direction. But there are almost no events left at $\Delta R > 3.5$.
Another useful variable to investigate is the transverse mass m_T (see section 4.3.6) calculated with the hadronic decay products of a single tau. A distribution for m_T with a possible cut to enhance the Z + jets contribution defined as $70 < m_T < 120\,\text{GeV}$ is shown in figure 7.5 but no significant improvement on the ratio between data and Z background can be reached with this cut, because the Z + jets distribution has almost the same shape as the data distribution and a cut would reduce the event yields by the same ratio.
The requirements for the validation region are summarized in table 7.1. The event yield in the validation region for the simulated Z + jets events and the events from data as well as the ratio between the two numbers is shown in table 7.2. Also indicated in this table are the effects of further cuts to enhance the Z + jets contribution in the validation region. Going to higher E_T^{miss} cuts improves the ratio but also the statistics of simulated Z events drops significantly. The improvement of the ratio with the addition of the m_T

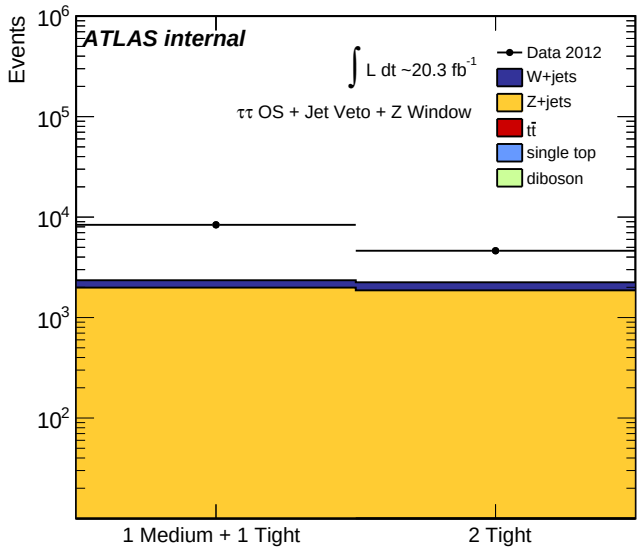

Figure 7.2: Distribution of different tau quality criteria. The difference between the data event yield and the stacked simulated background predictions is expected to be from the QCD multi-jet background.

cut is rather minimal. Therefore $E_T^{miss} > 40\,\text{GeV}$ was chosen for the validation region. The QCD multi-jet background is now estimated from the validation region with same sign requirement, where the same number of QCD multi-jet events is expected as in the opposite sign region. The number of other background processes in the same sign region is subtracted from the data events to obtain the QCD multi-jet estimation. The numbers in the opposite and same sign region are shown in table 7.3. The E_T^{miss} and m_{T2} distribution with QCD multi-jet estimation are shown in figure 7.6. The total background event yield with QCD multi-jet estimation is slightly lower than the number of data events but within the uncertainties. This proves the validity of the scale factors used. With the scaling factors applied to the Monte Carlo simulated events the Z + jets background resembles the observations in data events. Thus it is possible to estimate the Z + jets background for the SUSY search in this analysis from simulation.

Z Validation Region
2 "Tight" taus
OS pair
signal jet veto
$E_T^{miss} > 40\,\text{GeV}$
$m_{T2} < 90\,\text{GeV}$
$\lvert m_{\tau\tau} - 80\,\text{GeV}\rvert < 10\,\text{GeV}$
$\Delta\phi > 2.5$

Table 7.1: Summary of the Z validation region requirements.

Z Validation Region	Data	Z + Jets	Ratio(%)
with $E_T^{miss} > 40\,\text{GeV}$	4115±64.2	1742.3±130.5	42.3
with $E_T^{miss} > 50\,\text{GeV}$	1340±36.6	606.9±71.4	45.3
with $E_T^{miss} > 30\,\text{GeV}$	11189±105.8	4846.2±262.9	43.3
with $E_T^{miss} > 40\,\text{GeV}$ & $70 < m_T < 120\,\text{GeV}$	3168±56.3	1374.2±118.6	43.4

Table 7.2: Event yield for data and Z + jets background with ratio for different E_T^{miss} cuts and m_T cut.

Validation Region	OS	SS
Z + Jets	1742±131	15±10
W + Jets	126±96	0±0
Top	0.6±0.4	0±0
Diboson	3.7±1.1	0.50±0.29
MC Total	1873±162	16±10
MC + QCD	3894±168	
Data	4115±64	2037±45

Table 7.3: Number of events in the Z + jets validation regions. The second-to-last row shows the total Standard Model background with the QCD multi-jet contribution estimated from the same sign region.

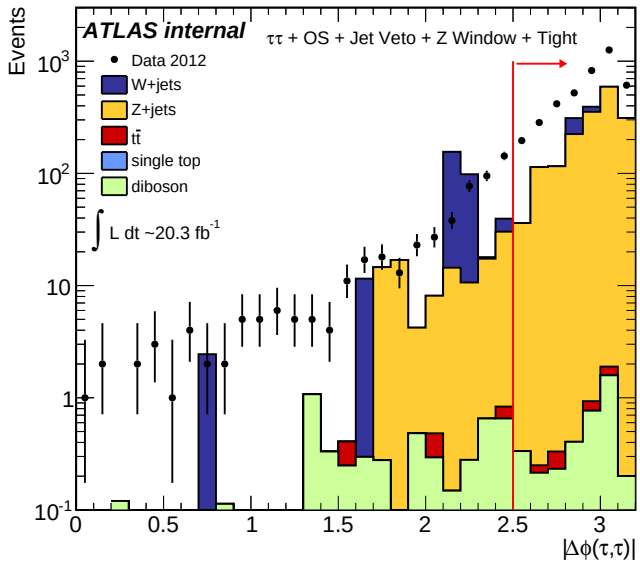

Figure 7.3: Distribution of $\Delta\phi$ between the two taus. The difference between the data event yield and the stacked simulated background predictions is expected to be from the QCD multi-jet background.

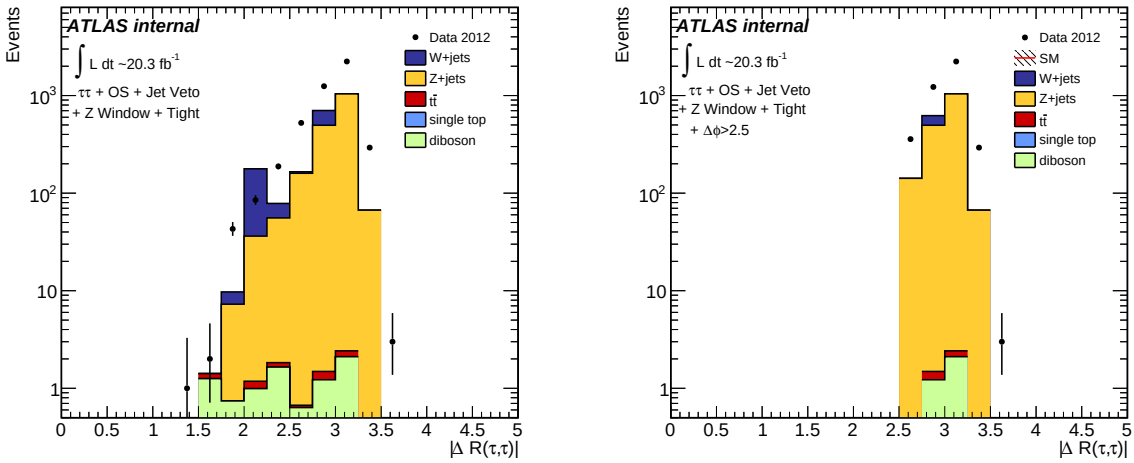

(a) Before $\Delta\phi$ cut

(b) After $\Delta\phi$ cut

Figure 7.4: Distribution of ΔR between the two taus. In 7.4a the requirements are two "tight" opposite sign taus, jet veto, $|m_{\tau\tau} - 80\,\text{GeV}| < 10\,\text{GeV}$, $E_T^{miss} > 40\,\text{GeV}$, and $m_{T2} < 90\,\text{GeV}$. In 7.4b in addition $\Delta\phi > 2.5$ is required. The difference between the data event yield and the stacked simulated background predictions is expected to be from the QCD multi-jet background.

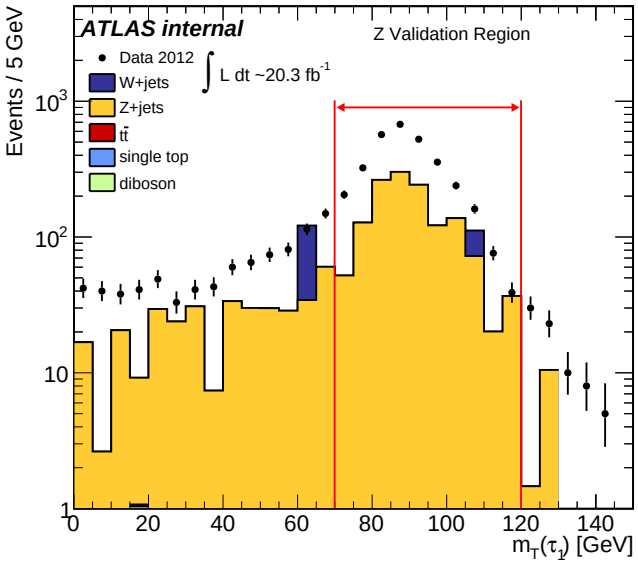

Figure 7.5: Distribution of m_T of the leading tau in the Z validation region. The difference between the data event yield and the stacked simulated background predictions is expected to be from the QCD multi-jet background.

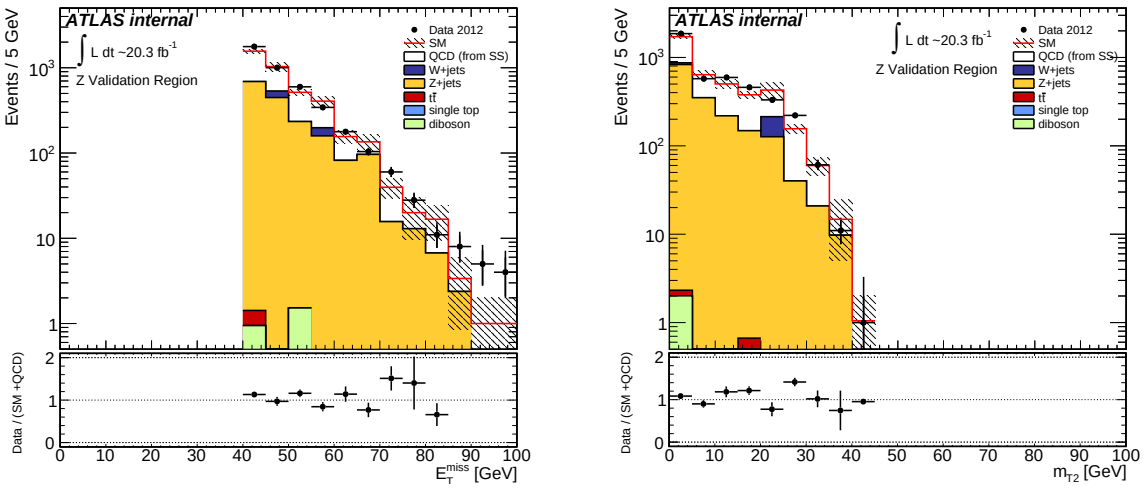

(a) E_T^{miss} distribution (b) m_{T2} distribution

Figure 7.6: Comparison of data and background event yields in the Z + jets validation region for the E_T^{miss} distribution (7.6a) and the m_{T2} distribution (7.6b). The QCD multi-jet background is estimated from the validation region with same sign requirement.

7.3 $t\bar{t}$ and Single Top

In the validation region for $t\bar{t}$ and single top two taus with opposite sign are required. The following cuts are used as a starting point: $E_T^{miss} > 40\,\text{GeV}$, $m_{T2} < 90\,\text{GeV}$ and the Z-veto. However the veto on signal jets is dropped to obtain a sufficient number of top events. Events with forward jets close to the beam axis are vetoed. The number of b-jets is a good way to further improve the ratio of top events. The distribution of the number of b-jets is shown in figure 7.7. If at least two b-jets are required the other backgrounds can be very effectively reduced, while the top decay processes are dominating in such an event topology. Therefore a cut on the number of b-jets to be at least 2 is chosen.

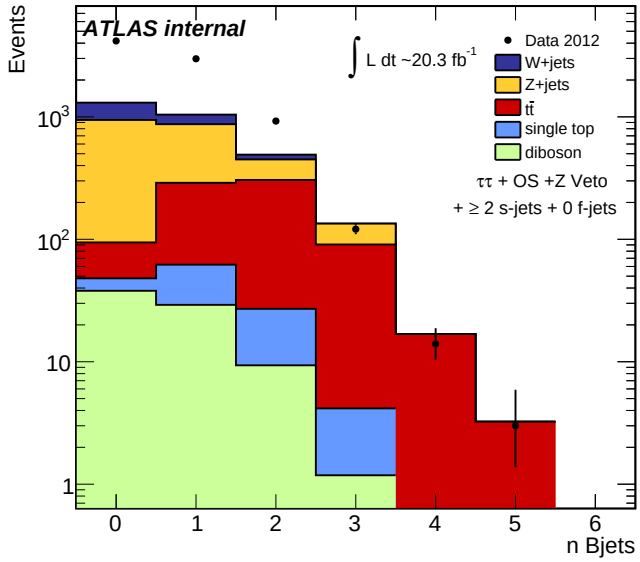

Figure 7.7: Distribution of the number of b-jets. The difference between the data event yield and the stacked simulated background predictions is expected to be from the QCD multi-jet background.

To suppress contributions from Z + jets events the sum of the transverse masses m_T of the two tau leptons can be used. This sum peaks at below 80 GeV for Z+jets, while for other backgrounds it peaks at higher values. This is shown in figure 7.8. An additional cut on $m_T(\tau_1) + m_T(\tau_2) > 80\,\text{GeV}$ is applied. A variable used to study $t\bar{t}$ decays is the contransverse mass m_{CT} [64]. This observable can be calculated from the four-vectors of the selected jets and leptons:

$$m_{CT}^2(v_1, v_2) = [E_T(v_1) + E_T(v_2)]^2 - [p_T(v_1) - p_T(v_2)]^2 \tag{7.3}$$

where v_i can be a lepton (l), a jet (j), or a lepton-jet combination (jl), transverse momentum vectors are defined by p_T and transverse energies E_T are defined as $E_T = \sqrt{p_T^2 + m^2}$. The quantities $m_{CT}(j, j)$, $m_{CT}(l, l)$ and $m_{CT}(jl, jl)$ have an upper bound from analytical functions of the top quark and W boson masses. A top-tagged event must have at least

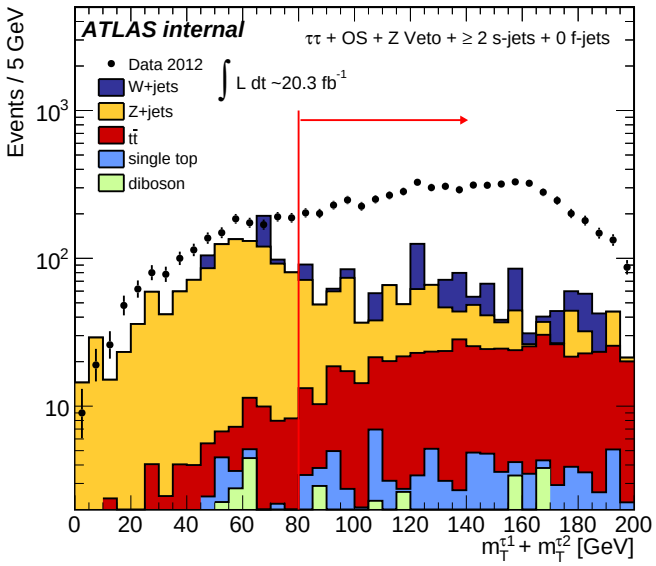

Figure 7.8: Distribution of the sum of the transverse masses m_T of the two tau leptons. The difference between the data event yield and the stacked simulated background predictions is expected to be from the QCD multi-jet background.

two jets with $p_T > 20$ GeV, and the scalar sum of the p_T of at least one combination of two jets and the two leptons in the event must exceed 100 GeV. Furthermore, top-tagged events are required to have m_{CT} values calculated from combinations of jets and leptons consistent with the expected bounds from $t\bar{t}$ events as described in Ref. [65].
A comparison of data events with Monte Carlo simulated background events for the m_{CT} top tagging algorithm is shown in figure 7.9. It can be seen that the m_{CT} is very useful to discriminate between top and other backgrounds, since the ratio of the $t\bar{t}$ and single top contribution in a validation region is significantly improved. Thus events in the validation region are required to be m_{CT} top tagged events.
The requirements for the validation region are summarized in table 7.4. The event yield in the validation region for the simulated $t\bar{t}$ and single top events and the events from data as well as the ratio between the two numbers is shown in table 7.5. Also indicated in this table are the effects of further cuts to enhance the Z + jets contribution in the validation region. Increasing the E_T^{miss} cut value significantly improves the ratio and above 50 GeV the QCD multi-jet contribution is not dominant as can be seen in figure 7.10a. However, the statistics drops. At E_T^{miss} values above 90 GeV the number of top events slightly exceeds the data event yield. But the estimated background is still within the uncertainty of the data. For the validation region $E_T^{miss} > 40\,\text{GeV}$ was chosen.
The QCD multi-jet background is estimated from the validation region with same sign requirement instead of opposite sign. The number of other background processes in the same sign region is subtracted from the data events to obtain the QCD multi-jet estimation. The numbers in the opposite and same sign region are shown in table 7.6. The E_T^{miss} and m_{T2} distributions with QCD multi-jet estimation are shown in figure 7.10.

Top Validation Region
2 taus
OS pair
$\geq$2 b-jets
$\geq$2 b-jets
m_{CT} top tag
$E_T^{miss} > 40\,\text{GeV}$
$m_{T2} < 90\,\text{GeV}$
$\lvert m_{\tau\tau} - 80\,\text{GeV}\rvert > 10\,\text{GeV}$
$m_T(\tau_1) + m_T(\tau_2) > 80\,\text{GeV}$

Table 7.4: Summary of the top validation region requirements.

Z Validation Region	Data	Top	Ratio (%)
with $E_T^{miss} > 40\,\text{GeV}$	685±26.2	216.4±8.9	31.5
with $E_T^{miss} > 50\,\text{GeV}$	333±18.2	165.5±7.5	49.7
with $E_T^{miss} > 30\,\text{GeV}$	1285±35.8	271.8±10.6	21.2

Table 7.5: Event yield for data and top background with ratio for varied E_T^{miss} cuts.

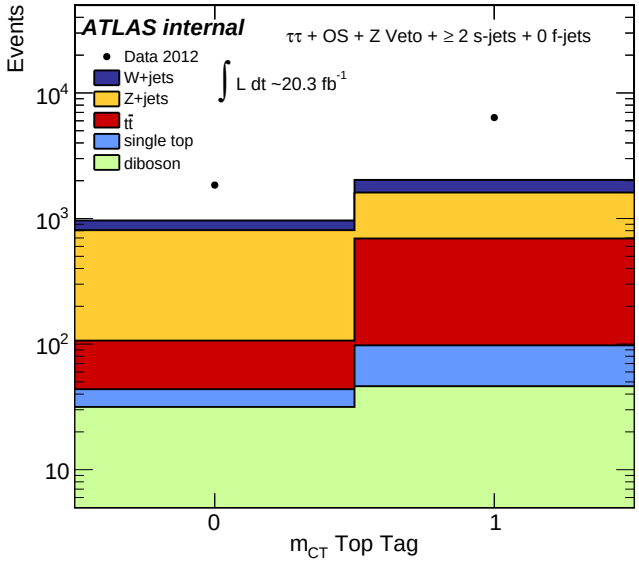

Figure 7.9: Distribution of events with and without the m_{CT} top tag. The difference between the data event yield and the stacked simulated background predictions is expected to be from the QCD multi-jet background.

In the same sign control region the top background contributes $\sim 15\%$ of the data event yield. This slightly influences the QCD multi-jet estimation. The background estimation is a little above the data event yield in the validation region, but the numbers fit within the uncertainties. Thus also the $t\bar{t}$ and single top background is valid to be estimated from Monte Carlo simulation with the scaling factors used for this analysis.

Validation Region	OS	SS
Top	348±10	80±7
W + Jets	36±26	0±0
Z + Jets	48±11	14±9
Diboson	5.4±1.1	1.0±0.6
MC Total	438±30	95±11
MC + QCD	827±39	
Data	777±28	484±22

Table 7.6: Number of events in the top validation region. The second to last row shows the total Standard Model background with the QCD multi-jet contribution estimated from the same sign region.

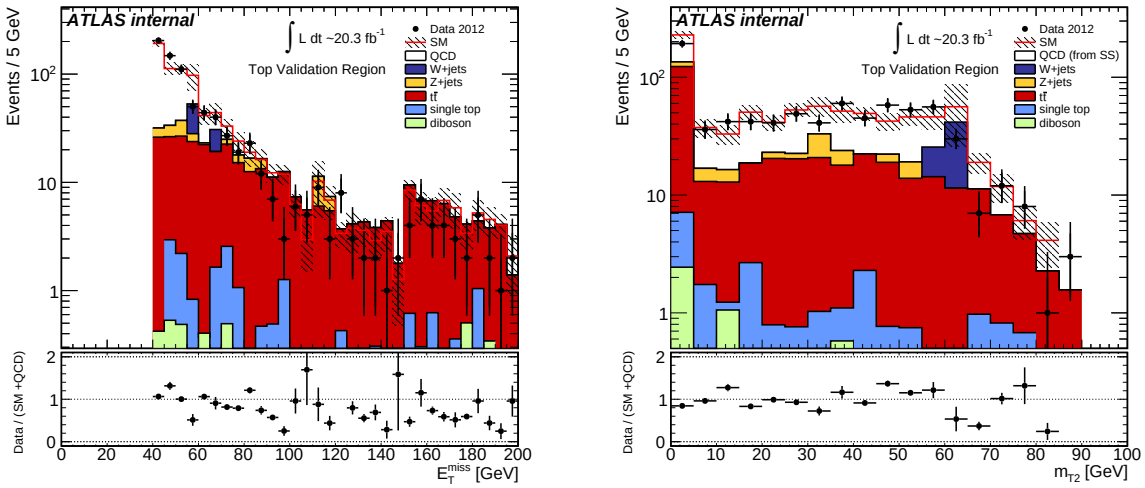

(a) E_T^{miss} distribution

(b) m_{T2} distribution

Figure 7.10: Comparison of data and background event yields in the top validation region for the E_T^{miss} distribution (7.10) and the m_{T2} distribution (7.10b). The QCD multi-jet background is estimated from the validation region with same sign requirement.

7.4 Tau Charge Misidentification Study

As an additional cross-check for the validity of the QCD multi-jet background estimation from the SS regions it is investigated in this section if the rate of hadronically decaying taus from Z decays with a misidentified electrical charge is similar in data and Monte Carlo simulation.
A precision measurement of $Z \to \tau\tau$ decay processes with two hadronically decaying taus in the final state is not possible due to the large contribution of QCD multi-jet processes. However, for studies such as the $Z \to \tau\tau$ cross-section measurement [66] this problem is avoided by studying events where only one tau decays hadronically and the other tau decays leptonically into a muon. The charge of high energetic muons can be identified with very high accuracy due to the track reconstruction in the inner detector and muon spectrometer. For the muon selection the basic muon definition described in section 4.3.3 is enhanced by several quality criteria. The isolation parameter "ptcone30", which corresponds to the p_T sum of the tracks in a cone of $\Delta R < 0.3$ around the muon, fulfills $\frac{ptcone30}{p_T} < 0.12$. The longitudinal impact parameter z_0 of the muon is required to have $|z_0 \cdot \sin\theta| < 0.4$. Finally the transverse impact parameter d_0 fulfills $|d_0/\sigma(d_0)| < 3$ [39].
To select events with one muon and one tau a trigger with online tau $p_T > 20\,\text{GeV}$ and with online muon $p_T > 15\,\text{GeV}$ is used. To use only events that have reached the trigger plateau also cuts on the p_T of the reconstructed objects have to be applied, which are slightly above the trigger thresholds. Thus $p_T > 25\,\text{GeV}$ is required for the reconstructed tau and $p_T > 18\,\text{GeV}$ for the reconstructed muon.

Validation Regions
1 "Tight" tau
1 isolated muon
muon + tau trigger
$p_T(\tau) > 25\,\text{GeV}$, $p_T(\mu) > 18\,\text{GeV}$
OS or SS pair
signal jet veto
$E_T^{miss} > 40\,\text{GeV}$
$m_{T2} < 90\,\text{GeV}$
$\lvert m_{\tau\mu} - 80\,\text{GeV}\rvert < 10\,\text{GeV}$
$\Delta\phi > 2.5$

Table 7.7: Summary of the charge misidentification validation region requirements.

To investigate the charge misidentification of taus in a $Z \to \tau_h\tau_\mu$ decay the same cuts as in the Z validation region are applied. Since jets are rarely misidentified as muons

Validation Region	OS	SS
W + Jets	1218.2±101.1	456.5±92.4
Z + Jets	5009.0±176.6	39.9±11.9
Top	2.7±0.8	0.2±0.2
Diboson	25.30±1.4	2.3±0.6
MC Total	6255.2±203.5	498.8±93.1
Data	5685±75.4	380±19.5

Table 7.8: Summary of the event yields in the $\mu\tau$ Z validation region with opposite sign or same sign requirement.

the QCD multi-jet background is very small and the Z decay process dominates. The definition of the validation region is summarized in table 7.7. The event yield in the validation region with opposite and same sign requirement is listed in table 7.8.
The Monte Carlo prediction is significantly overestimated compared to data. This is mostly due to the W+jets contribution, which is overestimated in the Monte Carlo simulation. In the $Z \to \tau\tau$ cross-section measurement [66] two additional cuts are applied to distinguish between Z and W events. For the first cut the kinematic observable $\sum \cos\Delta\phi$ is introduced. The angles in the transverse plane ϕ of the two leptons and the E_T^{miss} vector are used. The variable is defined as:

$$\sum \cos\Delta\phi = \cos\left(\phi(\mu) - \phi(E_T^{miss})\right) + \cos\left(\phi(\tau_h) - \phi(E_T^{miss})\right) \tag{7.4}$$

The distributions of $\sum \cos\Delta\phi$ can be seen in figure 7.11. The Z + jets distribution peaks at higher values than the W + jets distribution. Thus a cut with $\sum \cos\Delta\phi > -0.15$ is chosen to suppress the W contribution. To further suppress the W contribution also a cut on the transverse mass of the muon is applied $m_T(\mu)$. The distribution before the cut on $\sum \cos\Delta\phi$ is shown in figure 7.12. Since the cut on $\sum \cos\Delta\phi$ already rejects many of the W events, only a loose cut is applied on the transverse mass $m_T < 50\,\text{GeV}$.

Additional Cuts
$\sum \cos\Delta\phi > -0.15$
$m_T(\mu) < 50\,\text{GeV}$

Table 7.9: Summary of the additional charge misidentification validation region requirements.

The additional cuts for the validation region are summarized in table 7.9. It can be seen in the figures that the W + jets background is overestimated by the Monte Carlo simulation. To scale the sample the semi data driven method described in section 7.1 is applied. To

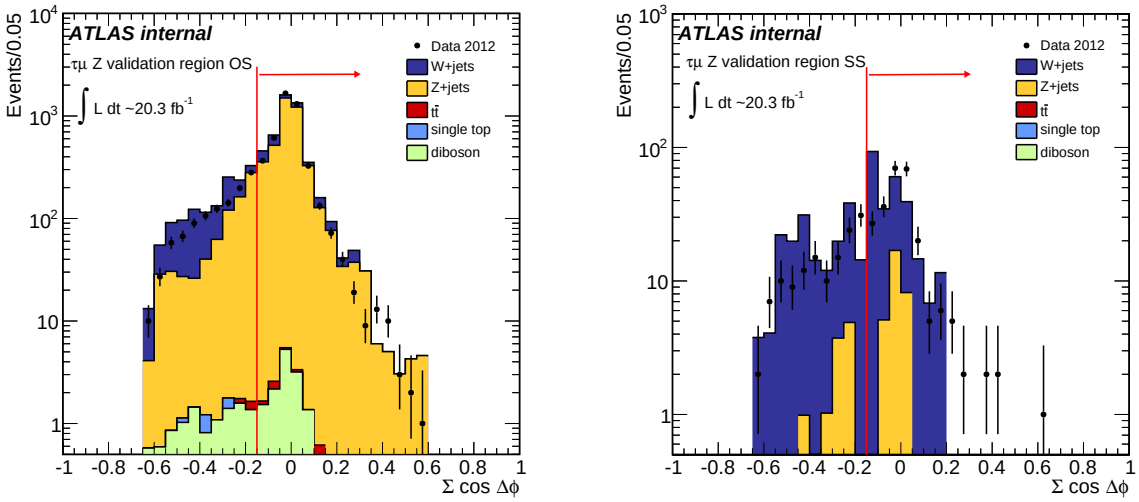

(a) Opposite Sign (b) Same Sign

Figure 7.11: Distribution of $\sum \cos\Delta\phi$ in the Z validation region with $\mu\tau$ requirement and leptons with opposite sign charges (7.11a) or same sign charges (7.11b). The QCD multi-jet background is not shown in these plots but it is expected to be small.

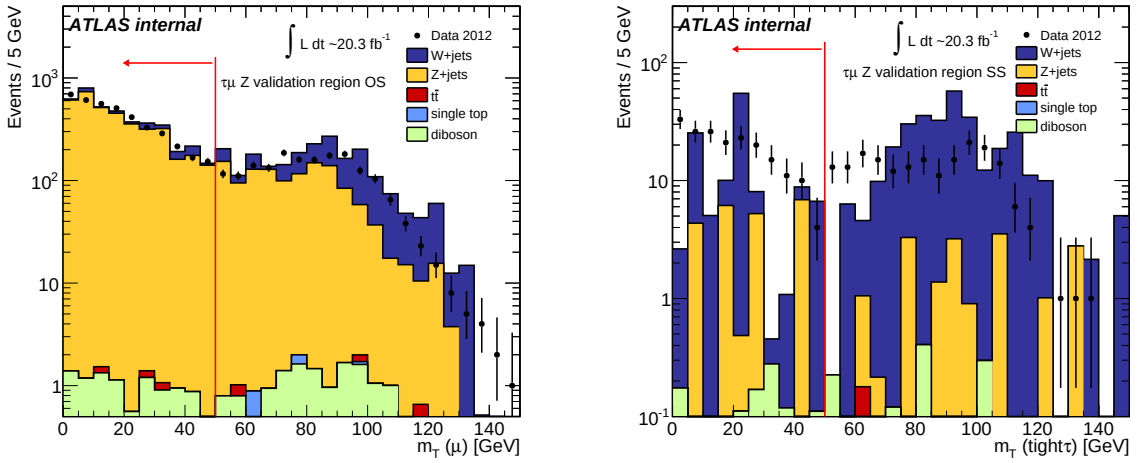

(a) Opposite Sign (b) Same Sign

Figure 7.12: Distribution of $m_T(\mu)$ in the Z validation region with $\mu\tau$ requirement and leptons with opposite sign charges (7.12a) or same sign charges (7.12b). The QCD multi-jet background is not shown in these plots but it is expected to be small.

W Control Regions
1 "Tight" tau
1 isolated muon
muon + tau trigger
$p_T(\tau) > 25\,\text{GeV}$, $p_T(\mu) > 18\,\text{GeV}$
OS or SS pair
signal jet veto
$E_T^{miss} > 40\,\text{GeV}$
$m_{T2} < 90\,\text{GeV}$
$\lvert m_{\tau\mu} - 80\,\text{GeV}\rvert < 10\,\text{GeV}$
$\Delta\phi > 2.5$
$\sum \cos\Delta\phi < -0.15$
$m_T(\mu) > 50\,\text{GeV}$

Table 7.10: Summary of the W + jets control region requirements.

W Control Region	OS	SS
W + Jets	544±64	161±32
Z + Jets	350±41	8±4
Top	1.3±0.6	0.18±0.18
Diboson	8.2±0.7	0.8±0.4
MC Total	905±77	170±33
Data	665±26	97±10

Table 7.11: Summary of the event yields in the W control region with opposite sign or same sign requirement.

obtain a W + jets dominated control region the W suppression cuts $\sum \cos\Delta\phi > -0.15$ and $m_T < 50\,\text{GeV}$ are inverted. The proportion of quark jets is higher in the opposite sign selection with respect to the gluon component that is dominant in the same sign selection. Therefore two separate scaling factors are calculated, one is determined in an opposite sign control region and the other in a region with same sign requirement. This is based on [66]. The definition of the W control regions is summarized in table 7.10. The event yield in the W control regions is listed in table 7.11.
The scaling factor $f_W = \frac{N_{CR}^{data} - N_{CR}^{otherSM}}{N_{CR}^{W}(MC)}$ for the different control regions is listed below:

- **Opposite Sign:** $f_W = 0.56 \pm 0.11$
- **Same Sign:** $f_W = 0.55 \pm 0.07$

A precise simulation of the W + jets background would yield a scaling factor close to 1. But the Monte Carlo simulated samples are very limited to describe a W decay process where one tau is generated by a misinterpreted jet in the event. In the $Z \to \tau\tau$ cross-section measurement the scaling factors in the opposite and same sign control regions are different. In this analysis the opposite sign W control region still has a major contribution from the Z + jets background, that influences the scaling factor. Due to the strong focus on the Z + jets background with the validation region cuts in this analysis the W control region defining cuts are not enough to suppress the contribution entirely. The similarity between the opposite sign and same sign region is a coincidence. The numbers in the control regions with the additional cuts and the scaled W + jets background is shown in table 7.12. The background prediction differs from the data, because the QCD multi-jet background is missing in this table. To estimate the ratio R of misidentified tau charges in a Z decay from data the estimation for other background processes is subtracted from the data event yield:

$$R = \frac{N_{SS}^{data} - N_{SS}^{otherSM}}{N_{OS}^{data} - N_{OS}^{otherSM}} \tag{7.5}$$

The ratio from data and from Monte Carlo simulation together with the ratio in the original Z validation region with two hadronically decaying taus is shown in table 7.13. As expected the ratio is higher for real data events, since the contribution from QCD multi-jet is missing. In [66] the QCD multi-jet background in the opposite sign region is estimated with an ABCD method but the same sign region is used as a control region. Thus this method cannot be used here. As a very rough estimate one could use the difference between Monte Carlo and data in the opposite sign region and assume this is the same in the same sign region. With this the ratio reduces from 2.9% to 1.6%. With the result an upper limit for the charge misidentification rate in data can be given with 2.9±1.0%.
In the case of two hadronically decaying taus the ratio is expected to be higher since there are two possibilities for a tau in the event to have a misidentified charge. However the difference between the estimation from data and Monte Carlo is small enough that the QCD multi-jet estimation from the same sign validation regions is not significantly influenced.

Validation Region	OS	SS
W + Jets	89±25	51±32
Z + Jets	3353±148	20.7±9.9
Top	0.55±0.32	0.0±0.0
Diboson	7.3±0.7	0.35±0.16
MC Total	3450±150	72±34
Data	3496±59	151±12

Table 7.12: Summary of the event yields in the $\mu\tau$ Z validation region with opposite sign or same sign requirement and the additional cut $\sum \cos\Delta\phi > -0.15$ and $m_T < 50\,\text{GeV}$.

Validation Region	Ratio
$\tau_h\tau_\mu$ (data)	2.9±1.0%
$\tau_h\tau_\mu$ (MC)	0.6±0.3%
$\tau_h\tau_h$ (MC)	0.9±0.6%

Table 7.13: Summary of the τ charge misidentification ratios in a $Z \to \tau\tau$ decay.

8 Results

In this chapter the sensitivity of the analysis is presented for completeness. Other members of the ATLAS SUSY working group developed the methods and derived the numbers that are presented in this chapter.

8.1 Data and Background Comparison

With the methods described in chapter 5 the background estimation is now compared with the data event yield in the signal regions. The QCD multi-jet & W + jets background is estimated from data with the ABCD method, the Z + jets and top background is estimated from Monte Carlo simulation with the ABCD-like method, and finally the diboson background is directly estimated from the simulated samples. The event yields and uncertainties are listed in table 8.1.

	OS-m_{T2}	OS-m_{T2}-nobjet
Z + Jets	0.28 ± 0.26 ± 0.23	0.4 ± 0.3 ± 0.3
Top	0.2 ± 0.5 ± 0.1	1.6 ± 0.8 ± 1.2
Diboson	2.2 ± 0.5 ± 0.5	2.5 ± 0.5 ± 0.9
QCD &W + Jets	8.4 ± 2.6 ± 1.4	12 ± 3 ± 3
SM Total	11.0 ± 2.7 ± 1.5	17 ± 4 ± 3
Data	6	14
SUSY Ref. P1:	6.8 ± 1.0	9.2 ± 1.2
SUSY Ref. P2:	7.5 ± 0.7	8.9 ± 0.7

Table 8.1: Summary of the event yields in the signal regions. The Standard Model background expectations are listed. The number of events in $\int \mathcal{L}\,\mathrm{dt} = 20.7\,\mathrm{fb}^{-1}$ of recorded ATLAS data in 2012 is shown. A comparison with the two reference SUSY samples is given. The first error is the statistical uncertainty and the second is the systematic uncertainty. [38]

Additionally the distributions of several kinematic variables are given in this section. The m_{T2} distribution in each signal region is shown in figure 8.1. The distribution of

p_T and η of the leading tau is shown in figure 8.2 and the distribution of the missing transverse energy E_T^{miss} and the invariant mass of the tau pair $m_{\tau\tau}$ is shown in figure 8.3.

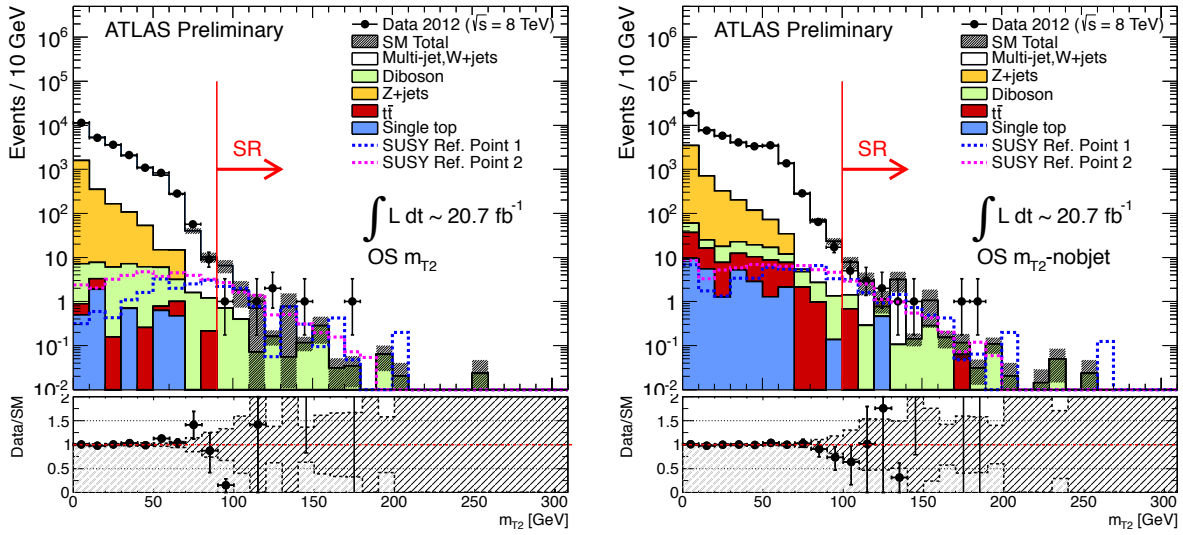

(a) OS-m_{T2} (b) OS-m_{T2}-nobjet

Figure 8.1: m_{T2} distribution for signal region OS-m_{T2} (8.1a) and for OS-m_{T2}-nobjet (8.1b). The stacked histograms show the expected backgrounds. The white histogram represents the multi-jet and W+jets contribution obtained from data using the ABCD method. The Standard Model backgrounds are normalized to 20.7 fb^{-1}. The lower plots show the distributions of data over SM background ratio. [38]

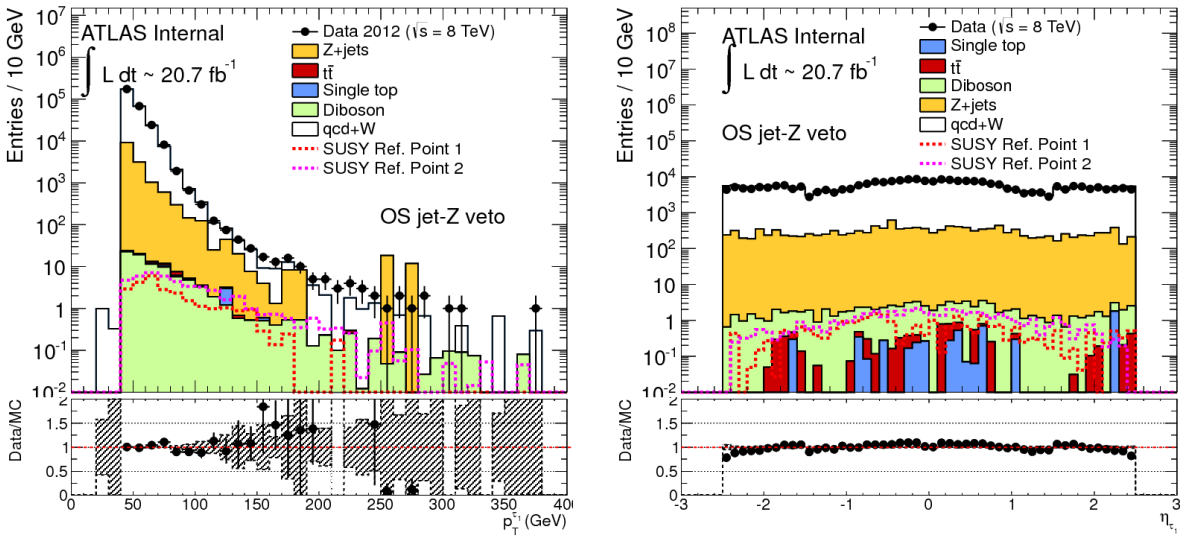

(a) $p_T(\tau_1)$ (b) $\eta(\tau_1)$

Figure 8.2: Kinematic distribution of the p_T of the leading tau (8.2a) and of the η of the leading tau (8.2b) for OS events with jet and Z veto. [38]

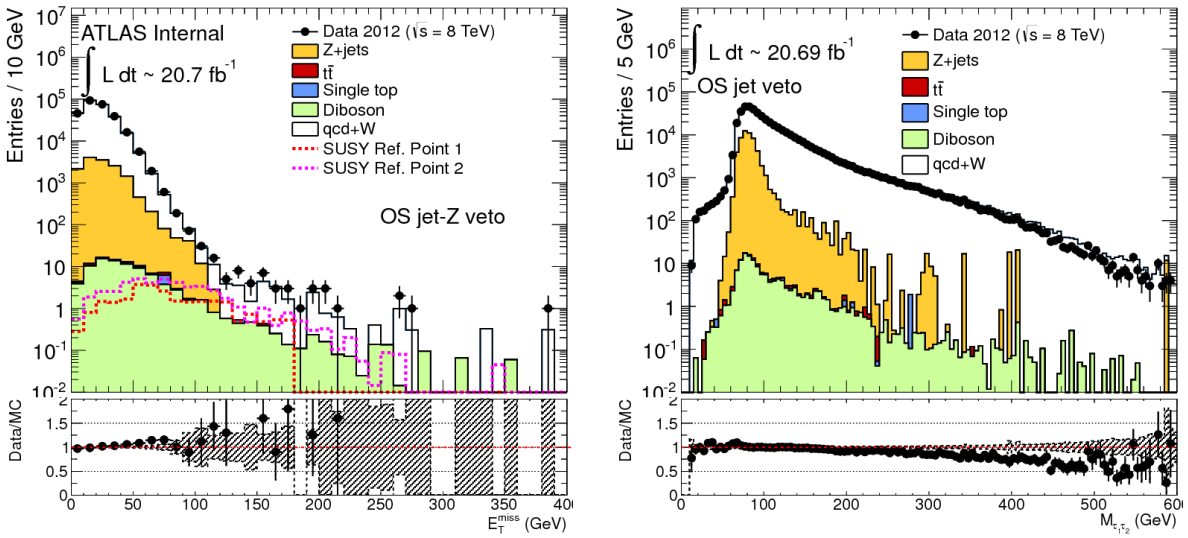

(a) E_T^{miss} (b) $m_{\tau\tau}$

Figure 8.3: Kinematic distribution of the missing transverse energy E_T^{miss} (8.3a) and of the invariant mass of the tau pair $m_{\tau\tau}$ (8.3b) for OS events with jet veto and a Z veto applied only in the E_T^{miss} distribution. [38]

8.2 Interpretation

Since no significant excess in data is observed compared to the estimated Standard Model background, exclusion limits on the analyzed SUSY models can be given.
In the exclusion plots given in this section the yellow error band around the expected limit corresponds to the $\pm 1\sigma$ results, which includes all systematic uncertainties except the theoretical uncertainties on the SUSY cross section. For the error band $\pm 1\sigma \pm 1^{SUSY}_{theory}$ around the observed limits the SUSY cross section has been varied by $\pm 1\sigma$. The limits summarized below correspond to the $-1\sigma^{SUSY}_{theory}$ line.

- **Simplified Model C_1N_2 production:** The exclusion limits for the simplified model grid with chargino-neutralino production are shown in figure 8.4a. With the results from both signal regions a part of the parameter phase space can be excluded. The parameter space for masses of $\tilde{\chi}^0_1$ up to 100 GeV in a range up to 350 GeV for the $\tilde{\chi}^\pm_1$ mass can be excluded.

- **Simplified Model C_1C_1 production:** The exclusion limits for the simplified model grid with chargino-chargino production are shown in figure 8.4b. The results for the best fit of both signal regions leads to the exclusion of the parameter space for $\tilde{\chi}^0_1$ masses up to $30 - 50$ GeV in a range of $170 - 330$ GeV for the $\tilde{\chi}^\pm_1$ mass.

- **pMSSM:** The exclusion limits in the $\mu - M_2$ mass plane for the pMSSM signal grid with $M_1 = 50$ GeV and $\tan\beta = 50$ are shown in figure 8.5. Except for very low values around $100 - 150$ GeV and very high values greater than 400 GeV for both M_2 and μ the entire parameter space is excluded. In the low mass region the lightest chargino and the next-to-lightest neutralino are lighter than the stau. In this case the gauginos would decay into light leptons and jets rather than into taus. In the high mass region of M_2 and μ the direct stau production is dominating, which also leads to other decay processes, which are not the focus of this analysis.

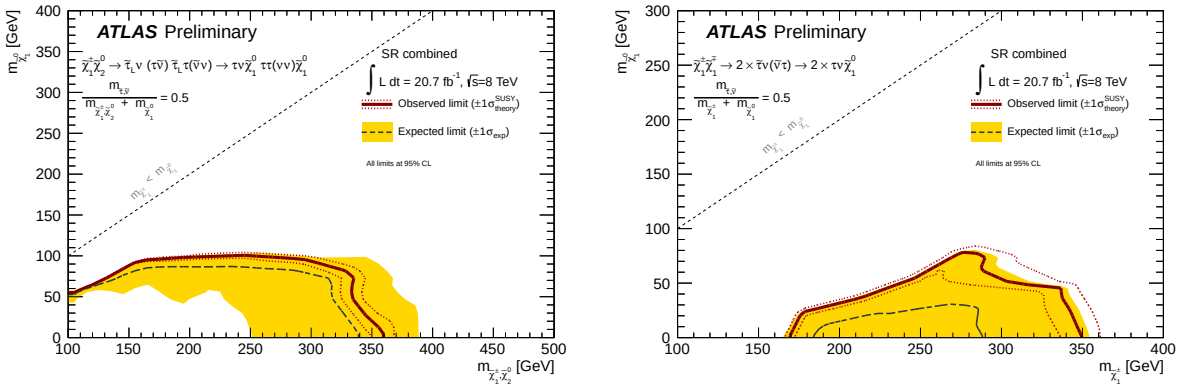

(a) C_1N_2 production (b) C_1C_1 production

Figure 8.4: 95% CL exclusion limits for simplified model grids with chargino-neutralino production (8.4a) or chargino-chargino production (8.4b) for the signal region with the best expected limit at each grid point. The black dashed line shows the 95% CLs expected limit. The solid band around the expected limit shows the $\pm 1\sigma$ result where all uncertainties, except those on the signal cross-sections, are considered. The $\pm 1\sigma$ lines around the observed limit represent the results obtained when moving the nominal signal cross section up and down by the $\pm 1\sigma$ theoretical uncertainty. [38]

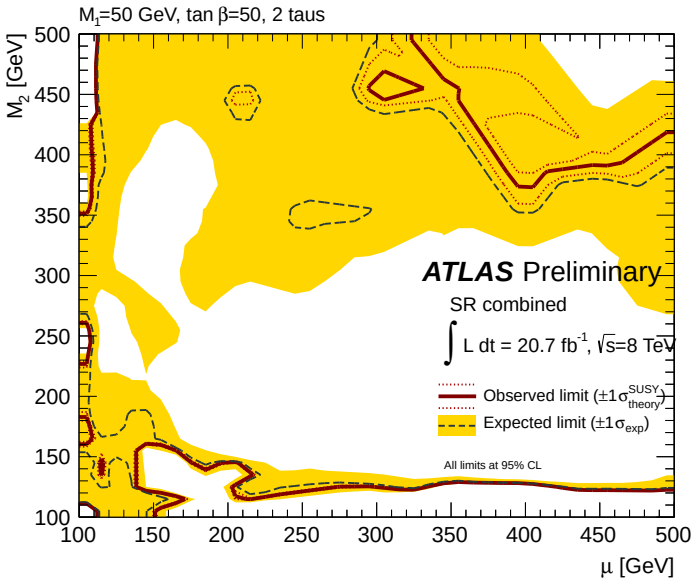

Figure 8.5: 95% CL exclusion limits in the $\mu - M_2$ mass plane of the pMSSM grid with $M_1 = 50\,\text{GeV}$, $\tan\beta = 50$ for the signal region with the best expected limit at each grid point. The black dashed line shows the 95% CLs expected limit. The solid band around the expected limit shows the $\pm 1\sigma$ result where all uncertainties, except those on the signal cross-sections, are considered. The $\pm 1\sigma$ lines around the observed limit represent the results obtained when moving the nominal signal cross section up and down by the $\pm 1\sigma$ theoretical uncertainty. [38]

9 Summary and Conclusions

In this thesis a search for the electroweak pair production of supersymmetric particles in events with at least two hadronically decaying tau leptons and missing transverse energy in the final state was presented. A sample of proton-proton collisions at a center of mass energy of $\sqrt{s} = 8\,\text{TeV}$ with an integrated luminosity of $\int \mathcal{L}\ \text{dt} = 20.3\,\text{fb}^{-1}$ was used.
In SUSY models where the tau slepton is lighter than the electron and muon sleptons, charginos and neutralinos decay prevalently through tau leptons. In this thesis the direct production of $\tilde{\chi}_2^0\tilde{\chi}_1^\pm$ and $\tilde{\chi}_1^\pm\tilde{\chi}_1^\mp$ is studied. The first case yields 3 tau leptons in the final state, and the latter yields two. The chargino decays into a left-handed pair of stau and tau neutrino or stau neutrino and tau. The next-to-lightest neutralino decays into a stau and a tau. The staus or stau neutrinos then further decay into the lightest neutralino and a tau or tau neutrino. In the final state two or more taus, two neutralinos, and possibly tau neutrinos are present. The neutralinos and neutrinos escape the detection, which leads to a high missing transverse energy. The studied signature is therefore events with two or more hadronically decaying taus and large missing transverse energy in the final state. The dominant Standard Model background to this search are the QCD multijet and W + jets processes, where the taus are mis-identified quark or gluon jets. Minor contributions come from Z + jets, $t\bar{t}$, single top and diboson processes. The QCD multi-jet and W + jets processes are estimated from data with an ABCD method. The other backgrounds are estimated from Monte Carlo simulated samples. However the estimation of the Z and top contributions is improved with a Monte Carlo driven "ABCD"-like method.
The improvement of the Z and top background estimation with a different approach to the "ABCD"-like method that has been used for the ATLAS note [38] is presented. The goal was to increase the statistics in the control regions to give a more reliable prediction for the signal regions. The relative statistical uncertainty for the Z background prediction is reduced in signal region OS-m_{T2} from 93% to 72% and in signal region OS-m_{T2}-nobjet from 75% to 54%. The statistics in control regions B and C has been improved by a factor of 5 and 10, respectively, for signal region OS-m_{T2} and by a factor of 3 and 8, respectively, for signal region OS-m_{T2}-nobjet. The relative statistical error for the top background prediction is reduced in signal region OS-m_{T2} from 250% to 31% and in signal region OS-m_{T2}-nobjet from 50% to 22%. The statistics in control regions B and C has been improved by a factor of 158 and 4, respectively, for signal region OS-m_{T2} and by a factor of 7 and 3, respectively, for signal region OS-m_{T2}-nobjet.
Another study is presented to prove the validity of the use of the Monte Carlo samples for estimating the Z+jets and top background. In this study validation regions enriched with either Z or top events have been developed. The background prediction is comparable to the data within uncertainties. An additional cross-check has been performed to prove

that the rate of charge misidentification of taus in data is not too different from the Monte Carlo simulation. An upper limit of 2.9±1.0% for the charge misidentification rate of hadronically decaying taus from Z decays in data events has been derived.
No excess of events has been observed with respect to Standard Model predictions. This result has been interpreted in a phenomenological Minimal Supersymmetric Standard Model (pMSSM), a simplified model with chargino-neutralino pair production, and a simplified model with chargino pair production. For the simplified model with chargino-neutralino pair production the parameter space for masses of the lightest neutralino up to 100 GeV and up to 350 GeV for the lightest chargino can be excluded. For a simplified model with chargino pair production the parameter space for the lightest neutralino mass up to $30 - 50$ GeV in a range for the lightest chargino mass of $170 - 330$ GeV can be excluded at 95% confidence level. For the pMSSM model except for very low values around $100 - 150$ GeV and very high values greater than 400 GeV for both M_2 and μ the entire parameter space is excluded.

Bibliography

[1] D. H. Perkins, *Introduction to High Enrergy Physics*, Addison Wesley, 1987

[2] C. Berger, *Elementarteilchenphysik*, Springer, 2002

[3] D. Griffith, *Einführung in die Elementarteilchenphysik*, Akademie Verlag, 1996

[4] B. Povh, K. Rith, C. Scholz, F. Zetsche, *Particles and Nuclei*, Springer, 1995

[5] M. E. Peskin, D. V. Schroeder, *An Introduction to Quantum Field Theory*, Addison-Wesley, 1987

[6] J. Beringer et al. (Particle Data Group), *Particle Physics Booklet*, Phys. Rev. D **86**, 010001 (2012)

[7] J. W. F. Valle *Neutrino masses twenty-five years later*, AIP Conf.Proc.687:16-32 (2003), arXiv:hep-ph/0307192

[8] Planck Collaboration, *Planck 2013 results. XVI. Cosmological parameters*, arXiv:1303.5076 [astro-ph.CO] (2013)

[9] M. Drees, R. M. Godbole, P. Roy, *Theory and Phenomenology of Sparticles*, World Scientific, 2005

[10] S. P. Martin, *A Supersymmetry primer*, hep-ph/9709356 (2008)

[11] R. N. Mohapatra, *Unification and Supersymmetry*, Springer, 1996

[12] J. Wess, B. Zumino, *A Lagrangian Model Invariant under Supergauge Transformations*, Phys. Lett. B **49**, 52 (1974)

[13] J. Wess, B. Zumino, *Supergauge Transformations in Four Dimensions*, Nucl. Phys. B **70**, 39 (1974)

[14] D. Alves et al., *Simplified Models for LHC New Physics Searches*, J. Phys. G: Nucl. Part. Phys. **39** (2012), arXiv:1105.2838

[15] J. Alwall, P. Schuster, N. Toro, *Simplified Models for a First Characterization of New Physics at the LHC*, Phys. Rev. D **79**, 075020 (2009), arXiv:0810.3921

[16] ATLAS Collaboration, *Observation of a new particle in the search for Standard Model Higgs boson with the ATLAS detector at the LHC*, Phys. Lett. B **716**, 1-29 (2012)

[17] CMS Collaboration, *Observation of a new boson at a mass of 126 GeV with the CMS experiment at the LHC*, Phys. Lett. B **716**, 30-61 (2012)

[18] A. Djouadi, J.L. Kneur, and G. Moultaka, *SuSpect: a Fortran Code for the Supersymmetric and Higgs Particle Spectrum in the MSSM*, hep-ph/0211331v2 (2005)

[19] DØ Collaboration, *Search for associated production of charginos and neutralinos in the trilepton final state using 2.3 fb^{-1} of data*, Phys. Lett. B **680**, 34-43 (2009)

[20] LEP2 SUSY Working Group, http://lepsusy.web.cern.ch/lepsusy/www/inos_moriond01/charginos_pub.html

[21] ATLAS Experiment, https://twiki.cern.ch/twiki/bin/view/AtlasPublic/SupersymmetryPublicResults

[22] Prospino, http://www.thphys.uni-heidelberg.de/∼plehn/index.php?show=prospino&visible=tools

[23] CERN-Homepage: *http: // www. cern. ch*

[24] O. Brüning et al., *LHC Design Report*, CERN-2004-003

[25] ATLAS Homepage: http://www.atlas.ch/

[26] ATLAS Collaboration, *The ATLAS Experiment at the CERN Large Hadron Collider*, JINST **3** (2008) S08003, *http://www.iop.org/EJ/abstract/1748-0221/3/08/S08003*

[27] ATLAS Collaboration, *ATLAS Detector and Physics Performance Technical Design Report, Volume 1*, ATLAS-TDR-14, CERN-LHCC-99-14, 1999 *http://atlas.web.cern.ch/Atlas/GROUPS/PHYSICS/TDR/access.html*

[28] M. Lamprecht, *Studien zu Effizienz und Akzeptanz des ATLAS-Myontriggers mit simulierten Messdaten*, Diploma thesis, Ludwig-Maximilians-Universität München (2007)

[29] The ATLAS Collaboration, *ATLAS Insertable B-Layer Technical Design Report*, ATLAS TDR 19, CERN/LHCC 2010-013

[30] ATLAS Experiment, https://twiki.cern.ch/twiki/bin/view/AtlasPublic/TriggerOperationPublicResults

[31] ATLAS Experiment, https://twiki.cern.ch/twiki/bin/view/AtlasPublic/LuminosityPublicResults

[32] Worldwide LHC Computing Grid, http://lcg.web.cern.ch/lcg/

[33] ATHENA, https://twiki.cern.ch/twiki/bin/view/Atlas/AthenaFramework

[34] The Gaudi Project, http://proj-gaudi.web.cern.ch

[35] R. Brun, F. Rademakers: *ROOT - An Object-Oriented Data Analysis Framework*, http://root.cern.ch/

[36] K. Assamagan et al., *The ATLAS Monte Carlo Project*, ATL-SOFT-INT-2010-002

[37] S. Agostinelli et al., *Geant4 - A Simulation Toolkit*. Nucl. Instrum. Meth. A, **506**(3): 250–303 (2003), http://geant4.web.cern.ch/geant4/

[38] The ATLAS Collaboration, *Search for electroweak production of supersymmetric particles in final states with at least two hadronically decaying taus and missing transverse momentum with the ATLAS detector in proton-proton collisions at* $\sqrt{s} = 8$ *TeV*, ATLAS-CONF-2013-028 (2013)

[39] The ATLAS Collaboration, *Search for direct-slepton and direct-chargino production in final states with two opposite-sign leptons, missing transverse momentum and no jets in 20* fb^{-1} *of pp collisions at* $\sqrt{s} = 8$ *TeV with the ATLAS detector*, ATLAS-CONF-2013-049 (2013)

[40] The ATLAS Collaboration, *Search for direct production of charginos and neutralinos in events with three leptons and missing transverse momentum in 21* fb^{-1} *of pp collisions at* $\sqrt{s} = 8$ *TeV with the ATLAS detector*, ATLAS-CONF-2013-035 (2013)

[41] H. Baer, F. E. Paige, S. D. Protopescu, X. Tata, *ISAJET 7.69: A Monte Carlo Event Generator for pp,* $\bar{p}p$*, and* e^+e^- *Reactions*, arXiv:hep-ph/0312045 (2003)

[42] T. Gleisberg et. al., *Event generation with SHERPA 1.1*, JHEP 0902:007 (2009), arXiv:0811.4622

[43] S. Frixione, B.R.Webber, *The MC@NLO 3.2 event generator*, hep-ph/0601192 (2006)

[44] B. Kersevan, E. Richter-Was, *The Monte Carlo Event Generator AcerMC 2.0 with Interfaces to PYTHIA 6.2 and HERWIG 6.5*, arXiv:hep-ph/0405247 (2004)

[45] J. Alwall et al., *MadGraph 5 : Going Beyond*, arXiv:1106.0522 (2011)

[46] M. Cacciari, G. Salam, and G. Soyez, *The anti-*k_t *jet clustering algorithm*, arXiv:0802.1189v2 [hep-ph] (2008)

[47] The ATLAS Collaboration, *Local Hadronic Calibration*, ATL-LARG-PUB-2009-001

[48] D. W. Miller, A. Schwartzman, D. Su, *Jet-Vertex Association Algorithm*, ATL-COM-PHYS-2008-008 (2008)

[49] The ATLAS collaboration, *Commissioning of the ATLAS high-performance b-tagging algorithms in the 7 TeV collision data*, ATLAS-CONF-2011-102

[50] The ATLAS Collaboration, *Performance of the Reconstruction and Identification of Hadronic τ Decays in ATLAS with 2011 Data*, ATLAS-CONF-2012-142

[51] ATLAS Collaboration, *Muon reconstruction efficiency in reprocessed 2010 LHC proton-proton collision data recorded with the ATLAS detector*, ATLAS-CONF-2011-063, http://cdsweb.cern.ch/record/1345743

[52] ATLAS Collaboration, *A measurement of the ATLAS muon reconstruction and trigger efficiency using J/Ψ decays*, ATLAS-CONF-2011-021, http://cdsweb.cern.ch/record/1336750

[53] ATLAS Collaboration, *Electron performance measurements with the ATLAS detector using the 2010 LHC proton-proton collision data*, Eur. Phys. J. C **72** (2012) 1909, arXiv:1110.3174 [hep-ex]

[54] C.Lester, D.Summers, *Measuring masses of semi-invisibly decaying particles pair produced at hadron colliders*, Phys. Lett. B **463**, 99-103 (1999), arXiv:hep-ph/9906349v1

[55] A. Barr, C. Lester, P. Stephens, *m_{T2} : the truth behind the glamour*, J. Phys. G **29**, 2343-2363 (2003), arXiv:hep-ph/0304226v1

[56] ATLAS Collaboration, *Jet energy measurement with the ATLAS detector in proton-proton collisions at $\sqrt{s} = 7\,\text{GeV}$*, Eur. Phys. J. C, **73** 3 (2013) 2304, arXiv:1112.6426 [hep-ex]

[57] The ATLAS Collaboration, *Determination of the tau energy scale and the associated systematic uncertainty in proton-proton collisions at $\sqrt{s} = 7\,\text{GeV}$ with the ATLAS detector at the LHC in 2011*, ATLAS-CONF-2012-054

[58] ATLAS Collaboration, *Performance of missing transverse momentum reconstruction in proton-proton collisions at 7 TeV with ATLAS*, Eur.Phys.J.C **72** (2012) 1844, arXiv:1108.5602 [hep-ex]

[59] ATLAS Collaboration, *Improved luminosity determination in pp collisions at $\sqrt{s} = 7\,\text{GeV}$ using the ATLAS detector at the LHC*, CERN-PH-EP-2013-026, arXiv:1302.4393 [hep-ex]

[60] J. Alwall et al., *Comparative study of various algorithms for the merging of parton showers and matrix elements in hadronic collisions*, Eur. Phys. J. C **53** (2008) 473

[61] J. M. Campbell et al., *Vector boson pair production at the LHC*, JHEP 1107:018 (2011), arXiv:1105.0020 [hep-ph]

[62] M. Mangano et al., *ALPGEN, a generator for hard multiparton processes in hadronic collisions*, JHEP, 0307:001 (2003)

[63] G. Corcella et al., *HERWIG 6.5: an event generator for Hadron Emission Reactions With Interfering Gluons (including supersymmetric processes).*, JHEP, 0101:010, (2001)

[64] D. R. Tovey, *On measuring the masses of pair-produced semi-invisibly decaying particles at hadron colliders*, JHEP 0804:034 (2008), arXiv:0802.2879

[65] G. Polesello, D. R. Tovey, *Supersymmetric particle mass measurement with the boost-corrected contransverse mass*, JHEP 1003:030 (2010), arXiv:0910.0174

[66] The ATLAS Collaboration, $Z \to \tau\tau$ *cross section measurement in proton-proton collisions at* 7 TeV *with the ATLAS experiment*, ATLAS-CONF-2012-006

List of Tables

List of Figures

Danksagungen:

Am Ende dieser Arbeit möchte ich mich bei allen Personen bedanken, die mit zu deren Gelingen beigetragen haben, insbesondere bei:

- Prof. Dr. Dorothee Schaile für die Möglichkeit an ihrem Lehrstuhl zu promovieren und die sehr herzliche Aufnahme am Lehrstuhl. Sie ist mit verantwortlich für die sehr angenehme Arbeitsatmosphäre, die ich an diesem Lehrstuhl vorgefunden habe. Dann danke ich ihr auch für die sehr hilfreichen und lehrreichen Korrekturvorschläge kurz vor der Abgabe der Arbeit. Zu guter Letzt möchte ich mich natürlich auch für das Erstellen des Erstgutachtens meiner Arbeit bei ihr bedanken.

- Prof. Dr. Wolfgang Dünnweber für die Erstellung des Zweitgutachtens zu meiner Arbeit.

- Dr. Federica Legger für die gute, intensive und lehrreiche Betreuung während der Promotion. Auch bei der Korrektur der eigentlichen Arbeit hat sie mir wichtige Hinweise und Verbesserungsvorschläge gegeben.

- Dr. Julien de Graat und Dipl.-Phys. Christopher Schmitt für das Korrekturlesen meiner Arbeit.

- Allen aktiven und ehemaligen Mitgliedern des Lehrstuhls Schaile, mit denen ich während meiner Zeit am Lehrstuhl zusammen arbeiten durfte. Insbesondere möchte ich mich bedanken bei Dr. Julien de Graat, Dr. Christian Kummer, Dr. Cedric Serfon, Dipl.-Phys. Christopher Schmitt, M.Sc. Alberto Vesentini und M.Sc. Josephine Wittkowski für die sehr angenehme Arbeitsumgebung in unserem gemeinsamen Büro. Sie haben mir auch sehr oft bei Problemen mit der Programmierung oder Analyse aushelfen können. Außerdem möchte ich mich bei ihrer Gesellschaft bedanken, die immer sehr aufmunternd und angenehm war.

- Den Teilnehmern der Arbeitstreffen zu Themen rund um die QCD, insbesondere bei Dr. Julien de Graat, Dr. Christian Kummer, Dr. Markus Lichtnecker und Dr. Thomas Müller.

- Meiner Familie und dabei vor allem meinen Eltern Dorothee und Johannes Becker. Sie haben mir durch ihre Erziehung, ihre finanzielle Unterstützung und den Rückhalt in unserem Zuhause den Abschluss eines Hochschulstudiums mit Promotion überhaupt erst ermöglicht. Aber auch bei der gesamten Großfamilie möchte ich mich bedanken, da es nicht selbstverständlich ist, dass man sich so gut miteinander versteht.